Bachelor End Project Electrical Engineering
Bioelectronics

Multi-Site Magnetic Neuronal Stimulation System for Earthworms: Design and Response Tracking

Group J

Arman van Dijk, Skip Doorn, Max Engels, Maarten Groen, Joris Hoogeweegen, Jiaqi Pan
5024021, 5356202, 5553725, 5169704, 5619963, 5043794

Supervisor:	Leon Abelmann
Daily supervisors:	Wouter Serdijn, Johan Meyer, Suman Kundu, Bas van Hoogstraten
Neutral Assessor:	Chris Verhoeven
Date final version:	2nd July 2024

Abstract

The device that is designed and described in this thesis aims to non-invasively stimulate neural activity in an earthworm at multiple, specific locations. This is done by inducing an electric field from two inductors with a specific electric field strength in mind. The response of the earthworm is recorded and amplified to enable analysis of this signal. Initially, requirements are set that need to be met by this device. From these requirements a design process was started and simulations were made. After this, a device was created on which the requirements could be evaluated. Due to the physical trials not being completed the requirements could not be fully verified.

Preface

This thesis is written in the context of the Bachelor Graduation Project for the Bachelor of Electrical Engineering at the Technical University Delft, conducted during the final ten weeks of the bachelor program. During this time, our group has been extensively researching and designing a device that can stimulate neural activity in a worm. This was a bumpy process in which we both learned a lot on the aspect of electronics design, but also how to work together as a team and reaching a collective goal. It must be said that for all of us this has been the most fun part of our academic journey yet. With this thesis we want to show the progress we made in acquiring and applying knowledge about magnetic stimulation, and our journey in designing a device that can achieve this. Special thanks go out to Leon Abelmann, Wouter Serdijn, Johan Meyer, Suman Kundu and Bas van Hoogstraten, for guiding us during this process and brainstorming together with us during the weekly meetings. We would also like to thank Nils Kauffmann for welcoming us with open arms to the Klushok and helping out with his extensive knowledge on electronics.

- The authors
June 2024

Task Division

Subgroup:	Group Members:
Stimulation	Joris Hoogeweegen, Jiaqi Pan
Control	Arman van Dijk, Skip Doorn
Recording	Max Engels, Maarten Groen

In the table above the subgroup division in shown. The group names correspond to the chapters below. All the other chapters are written by the entire group.

Contents

Glossary

ABBREVIATION	***DESCRIPTION***
TMS	Transcranial Magnetic Stimulation
SNR	Signal-to-Noise Ratio

Chapter 1

Introduction

Transcranial magnetic stimulation (TMS) is a non-invasive neuromodulation technique extensively used in clinical applications and basic research. During TMS, a coil is placed over the scalp. A brief high-intensity current pulse passes through the coil producing a time-varying magnetic field (B-field). The B-field further induces an electric field (E-field) inside the brain, which modulates brain activities [1, 2].

Since the introduction of TMS in 1985 by Barker and colleagues [3], relatively little is known about how TMS engages specific cortical regions, cell types, and neuronal compartments, as well as how it induces action potentials and propagates excitation within the brain [4]. Animal models are essential for investigating these underlying mechanisms since they allow more comprehensive electrophysiological recordings and invasive experiments that are difficult or impractical on humans [5]. However, most commercial TMS coils are designed for humans. The large geometric size of human TMS coils causes non-focal high-intensity stimulation, which is not applicable to small animal studies [5]. The low focality is also a problem for humans, when multi-site stimulation is desired. This can be addressed by using coil arrays to spatially adjust the electric field [6, 7, 8]. However, current multi-channel arrays do not overcome the fundamental limitations of electric field targeting. Achieving high resolution with small coil windings increases electric losses, mechanical stress, and driving current [9]. Therefore, there is a strong need for miniaturised TMS coils in the neuroscience, neural engineering, and clinical research communities [5].

This thesis aims to address these challenges by utilising earthworms, which provide a simpler and more accessible system for studying neuronal stimulation. It seeks to answer the question: **"How should a product be designed to effectively and safely utilise inductors for noninvasive neuronal stimulation at various sites on an earthworm, while ensuring accurate monitoring of the response of the neuron?"** The concept of this product is illustrated in Figure 1.1.

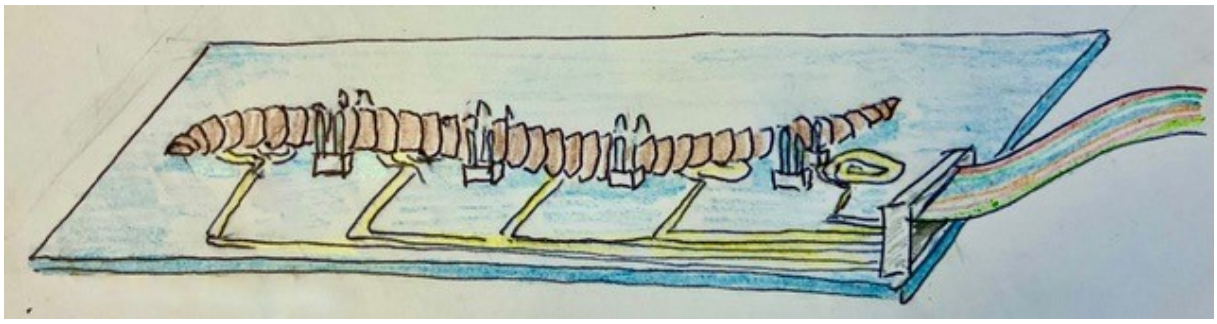

Figure 1.1: Concept of the initial product idea. In this figure a worm is attached to a plate with coils that are intended to stimulate neural activity (Abelmann, 2024).

The thesis is organised into nine chapters. Following this introduction, Chapter 2 presents a Programme of Requirements and Chapter 3 provides a comprehensive design overview. Chapter 4 delves into the necessary inductor and pulse characteristics for stimulation purposes. In Chapter 5, a circuit for systematic and controlled stimulation is discussed. Chapter 6 outlines a setup for recording and visualising the neuronal activity of the worm. Chapter 7 describes the integration of the designs from into a total system. Chapter 8 presents the project results, followed by a discussion. Finally, Chapter 9 concludes the project and offers recommendations for further research.

Chapter 2

Programme of Requirements

The mandatory requirements are those that must be met for the system to function properly. The trade-off requirements are requirements that improve the system on a specific front but are not necessary for the overall functionality of the system. The requirements and their rationale are described below.

Mandatory Requirements (General)

G-MR1 | The product must utilise an inductor to induce an electric field with a minimum strength of 100 V/m in air at the location of a neuron of a Lumbricus terrestris (earthworm).

G-MR2 | When measured 10 mm away from the stimulation site along the worm's length, the induced electric field strength from one inductor must be less than half of the strength at the stimulation site.

G-MR3 | The stimulation method must not require invasive procedures or penetration of the organism's body.

G-MR4 | The inductor must not reach temperatures above 318 K during stimulation.

G-MR5 | The electric field's orientation with respect to the worm must be adjustable, without moving the worm.

G-MR6 | The electric field strength must be adjustable in steps of 10 V/m.

G-MR7 | The stimulation setup must contain at least two inductors.

G-MR8 | The product must provide the user separate timing controls for each inductor.

G-MR9 | High-power components must be securely insulated and designed with safety features to ensure user protection.

G-MR10 | The response on neurons due to stimulation must be monitored at two distinct locations.

G-MR11 | The current induced by the inductors in the probes must not affect the measurement.

G-MR12 | The response of the neurons must be displayed within one second.

G-MR13 | The time between sedating the worm and the actual stimulation must be at most one minute.

G-MR14 | The maximum limit over the total cost must be less than €1000,-.

Trade-off Requirements (General)

G-TR1 | The induced electric field should provoke an action potential in a Lumbricus terrestris (earthworm).

G-TR2 | The inductors can be moved to different places.

G-TR3 | Multichannel measurements should be possible.

G-TR4 | The setup in its entirety should be mobile enough for a single person to move.

Requirements G-MR1, G-MR3 and G-MR7 were the initial requirements established by the project supervisors and form the primary rationale for this design. The assumption is that the specified electric field strength will be sufficient to stimulate neural activity in a worm. These requirements outline the primary objective: to create a product capable of non-invasively stimulating neurons using multiple inductors. Requirement G-MR2 specifies the focality of the electric field induced by a single inductor. This requirement arises from the necessity to position the inductors as close as 2 cm to each other while avoiding the induction of action potentials in the region between them due to the superposition of their electric fields. Requirement G-MR5 enables research on the relationship between the orientation of electric fields and the induction of action potentials. Requirements G-MR6 and G-MR8 specify how the inductors must be controlled. The step size is set to allow for testing different field strengths and determining the threshold needed to stimulate neural activity. The separate timing controls make research on the inhibiting of neurons, as well as subtreshold stimulation, possible. Requirement G-MR9 is focused on safety, emphasising the importance of securely storing the significant amount of power required by the design. Requirement G-MR10 mandates the response tracking of neurons at two locations. Requirements G-MR11 and G-MR12 further specify the capabilities and compliance of the measuring device to enhance the design's usability.

Requirement G-MR4 sets a temperature limit to ensure the safety of the worm's tissue. Requirement G-MR13 ensures rapid and humane testing procedures on the worm, ensuring sufficient research time while the worm remains sedated to minimise stress on the live animal. This design project and its associated research are conducted in accordance with animal research regulations.

Finally, Requirement G-MR14 addresses the budgetary constraint set by the project organisers, stipulating that the maximum budget available for the design is €1000.

Requirement G-TR1 is an expansion of G-MR1. It is desired that the 100V/m field provokes an action potential, as this is the ultimate goal of our design. However, due to uncertainty about the feasibility of this, it is noted as a trade-off requirement, making it secondary to the primary specifications. Requirement G-TR2 pertains to the mobility of the inductors. While modularity can enhance the usability of our design for research purposes, it is not essential and should not be the main focus during the design process. Requirement G-TR3 involves multichannel measurements. Although it is beneficial to have one device measure both signals, as outlined in requirement G-MR10, this functionality is not critical for the device's operation and is considered an added bonus. Requirement G-TR4 addresses the mobility of the entire system. As research equipment, making the system mobile would facilitate easier use and removal after experiments. However, this feature is not necessary for the system to function effectively.

Chapter 3

Design Overview

To develop a product capable of fulfilling all the requirements, a block diagram was created. This diagram provides a clear overview of the necessary components for the product's construction. The block diagram is shown in Figure 3.1.

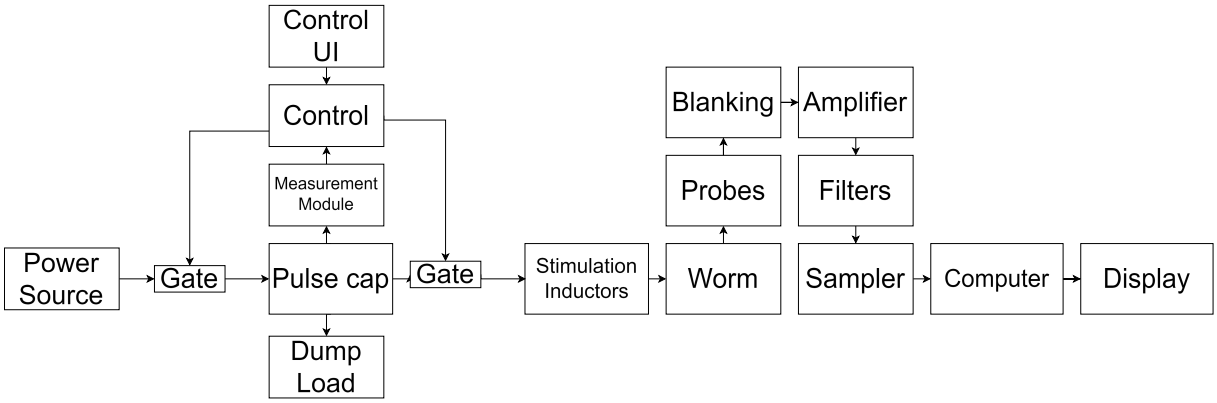

Figure 3.1: The full design block diagram

First, a power source is required for the system, which could be a direct connection to a socket or an independent battery. This power source is connected to a pulse capacitor via a gate. This gate, controlled by a control unit with a user interface, can be opened and closed to manage operations. The pulse capacitor is used to apply a short, high-current pulse to the stimulation inductors. It can also be discharged by opening a gate to a dump load. The stimulation inductors then transmit the pulse from the pulse capacitor to the worm using electromagnetic fields.

The next component is the worm. As mentioned in the Programme of Requirements, a L. terrestris (earthworm) will be used to evaluate the product. Probes are used to obtain a neural signal from the worm, which is then amplified and filtered. The signal is subsequently converted from analog to digital form. Finally, the signal is plotted for readout.

Detailed explanations of these blocks will be provided in their respective chapters. Additionally, the red blocks represent a testing setup to verify whether the blocks meet the requirements, as seen in fig 3.2. These testing setups will also be discussed in the upcoming chapters.

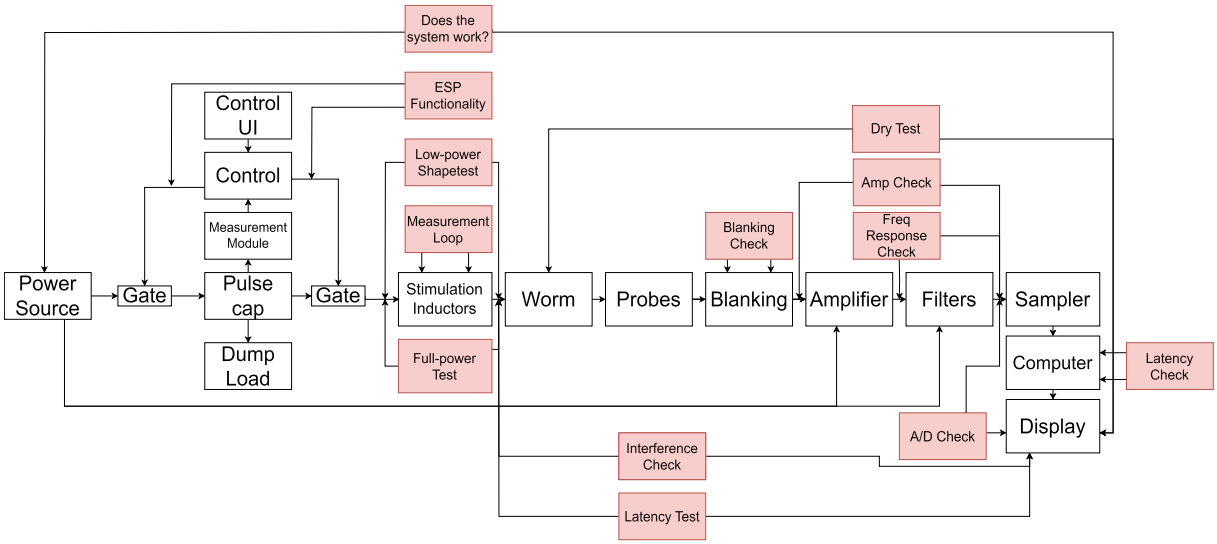

Figure 3.2: The full design block diagram with tests

Chapter 4

Stimulation

4.1 Introduction

The foundation of this project lies in utilising inductors to induce electric fields (E-Fields) in specific neuronal locations within an earthworm. Achieving this requires the design of both these inductors as well as the corresponding current pulses trough these inductors. Upon finalising this design, the Control subgroup (Chapter 5) will generate the requisite pulses, while the Recording subgroup (Chapter 6) will monitor the neuronal responses. Figure 4.1 illustrates the segment of the complete design overview, detailed in Chapter 3, that is dedicated to the stimulation subgroup.

The design of both inductor and pulse characteristics, henceforth referred to as 'the design', is necessary due to the insufficiency of current solutions to meet the requirements. As stated in Chapter 1, there is a strong need for miniaturised coils. Several miniaturised TMS coils have been developed for rodent studies, with better focality than human TMS coils [5] . The circular variants of these coils, however, do not reach the desired electric field strength by two orders of magnitude [10, 11, 12, 13, 14]. In contrast, the figure-eight variants achieve better focality and field strength but could be impractical in a multi-inductor setup due to their large dimensions [15, 16, 17]. The main challenge of designing high focality, miniaturised coils is thus caused by the trade-off between coil diameter and E-field strength [18].

In light of this problem, this chapter addresses the question: **"What inductor and pulse characteristics are necessary to induce the desired electric field for neuronal stimulation purposes?"** The chapter begins with a Program of Requirements (PoR) dedicated to the Stimulation subgroup. It then presents possible solutions for the design, followed by an analysis and selection of these solutions. The implementation of the optimal solution is described thereafter. Finally, the results are presented and discussed, leading to a conclusion that summarises the findings and suggests directions for future research.

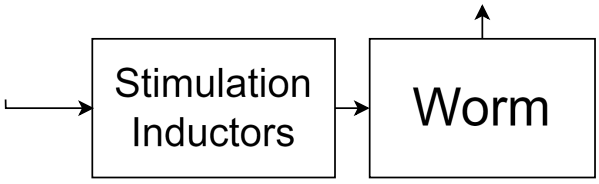

Figure 4.1: Segment of the design overview that is dedicated to the stimulation subgroup.

4.2 Program of requirements

Creating a stimulation inductor involves numerous aspects that must be examined before the design process can commence. To delineate the design objectives, a set of requirements was established and compiled into a PoR. This PoR is based on the general requirements. This section outlines these requirements and their rationale.

Mandatory Requirements

S-MR1 | The design must induce an electric field with a minimum strength of 100 V/m in air at 3 mm distance.

S-MR2 | The design must, when measured 10 mm away from the stimulation site, induce an electric field strength less than half of the strength at the stimulation site.

S-MR3 | The design must not reach temperatures above 318 K during stimulation.

S-MR4 | The design must function in a setup with at least two inductors.

S-MR5 | The total cost of the design must be less than €50,-.

Trade-off Requirements

G-TR1 | The induced electric field should provoke an action potential in a Lumbricus terrestris (earthworm).

G-TR2 | The inductors can be moved to different places.

Requirement S-MR1 is based on Requirements G-MR1 and G-MR3 and is established by looking at the anatomy of the earthworm, see Appendix A.1. Neurons are dispersed throughout the worm's body, making it impractical to designate a single distance or location for a neuron. Consequently, focus is directed towards the ventral nerve cord, which contains the largest axons. To reach the ventral nerve cord without penetrating the body, approximately 2.5 mm must be traversed between the skin and the nerve cord. This distance, supplemented by an additional 0.5 mm margin to avoid direct contact with the worm, results in the 3 mm specified in the requirement.

Requirement S-MR2 follows from G-MR2 and G-MR5, requiring one inductor to have a specified focality and adjustable orientation. Requirement S-MR2 is formulated in a way that, once this requirement is met, the control circuit and the worm can be added for the general requirements to be met.

Requirement S-MR3 and S-MR4 follow directly from G-MR4 and G-MR7, respectively. In both cases, it holds that once the design meets the requirements of the subgroup, the control circuit has to provide the necessary parameters for the general requirements to be met.

Requirement S-MR5 is formed by a preliminary estimate of inductor production costs, representing a small part of the total cost defined by G-MR14.

The Trade-off Requirements G-TR1 and G-TR2 are directly relevant for the Stimulation subgroup and are therefore duplicated from the General Requirements in Chapter 2.

4.3 Possible Solutions for Design

4.3.1 The Inductor Characteristics

Regarding the inductor, there are several considerations to take into account. The shape and size significantly impact the focusing of the E-field. This, in turn, influences thE-field's strength and focality, which are essential parameters for meeting Requirements S-MR1 and S-MR2. Inductor shapes can range from simple round coils to more complex configurations such as figure-of-eight, cloverleaf, and H-coils. Additionally, there are advanced modifications, including eccentric windings and 3-D differential coils, as well as the incorporation of magnetic cores to enhance performance [9]. The dimensions of these inductors can vary widely, from micrometer scales used in microelectromechanical systems (MEMS) [19] to centimeter-scale TMS coils [9]. The choice of wire material also plays a role in inductor design. Copper is the most commonly used material because of its high electrical conductivity. Additionally, some designs use Litz wire to reduce skin effect and proximity effect losses at higher frequencies [20].

4.3.2 The Pulse Characteristics

The characteristics of the current pulse mainly influence Requirements S-MR1 and S-MR2. The variety lies in the shape, slope and duration. From Appendix A.2, different pulse shapes (such as sinusoidal, rectangular, or biphasic) affect the temporal profile of the induced E-field and its interaction with neurons. The slope of the pulse waveform influences the E-field strength.

4.4 Design Analysis

4.4.1 Inducing an E-field

For all possible solutions, to address both Requirement S-MR1 and Requirement S-MR2, the initial step involves deriving the formulas necessary to calculate the E-field induced by the inductor. By solving Maxwell's equations, it can be determined that the magnetic vector potential $\boldsymbol{A}(\boldsymbol{r}, t)$ needs to be evaluated. This evaluation can be performed over a closed contour C in one dimension (1D) by Equation 4.1 or over a volume V in three dimensions (3D) by Equation 4.2.

$$\boldsymbol{A}(\boldsymbol{r}, t)_{1\mathrm{D}} = \frac{\mu_0}{4\pi} \oint_C \frac{I(t)}{|\boldsymbol{r} - \boldsymbol{r}'|} d\boldsymbol{l}' \tag{4.1}$$

$$\boldsymbol{A}(\boldsymbol{r}, t)_{3\mathrm{D}} = \frac{\mu_0}{4\pi} \int_V \frac{\boldsymbol{J}(\boldsymbol{r}', t)}{|\boldsymbol{r} - \boldsymbol{r}'|} dV' \tag{4.2}$$

From this magnetic vector potential, the induced E-field $\boldsymbol{E}(\boldsymbol{r}, t)$ can then be determined using Equation 4.3:

$$\boldsymbol{E}(\boldsymbol{r}, t) = -\frac{d\boldsymbol{A}(\boldsymbol{r}, t)}{dt} \tag{4.3}$$

From these equations, it follows that the E-field is influenced by both the characteristics of the inductor and the pulse. Firstly, the E-field strength increases proportionally with the rate of change of current over time, denoted as $\frac{dI}{dt}$. This implies that, concerning current characteristics, only the slope of the pulse significantly impacts the E-field strength. Secondly, the orientation of the E-field is consistently parallel to the direction of the current but oriented in the exact opposite direction. Thirdly, the E-field strength diminishes with increasing distance from the inductor $|\boldsymbol{r} - \boldsymbol{r}'|$. In order to make a choice on the inductor characteristics, the relation between the voltage and current of an inductor described by Equation 4.4 is needed.

$$\frac{dI}{dt} = \frac{V}{L} \tag{4.4}$$

From this equation, it is clear that increasing $\frac{dI}{dt}$ can be achieved by decreasing the inductance L. Reducing inductance can be accomplished by altering the inductor's dimensions. This relationship is depended on the inductor's shape, but for the most commonly used inductors, such as coils and wire loops, the relevant equations are provided in 4.5 and 4.6, respectively [21]. Increasing the diameter of these inductors will increase the inductance, and increasing the number of loops will result in a quadratic increase in inductance. Given that all the complex shapes discussed in potential solutions will depend on this or similar principles, the objective is to utilise a wire loop inductor with the simplest possible configuration.

$$L = \mu N^2 \frac{A}{l} \tag{4.5}$$

$$L \approx \mu \frac{D}{2} \left[\ln\left(\frac{8D}{d}\right) - 2 \right] \tag{4.6}$$

Back of the envelop calculation

Before determining the exact characteristics of the inductor and pulse, a preliminary estimation is conducted using a back-of-the-envelope calculation. This ballpark figure allows the control subgroup to make initial design decisions, upon which the stimulation subgroup then can build. Let us assume that the inductor is a circular wire loop with a radius $r_{\text{loop}} = 5\,\text{mm}$ at a distance $d = 3\,\text{mm}$ from the stimulation site. Then, by making a rough simplification that during integration both the direction of current and the distance to the stimulation site, remain constant, Equation 4.1 becomes Equation 4.7. This simplification underestimates the required $\frac{dI}{dt}$.

$$\boldsymbol{A}(d,t)_{1\text{D}} = \frac{\mu_0 I(t)}{4\pi} \int_0^{2\pi} \frac{r_{\text{loop}}}{d} d\theta' = I(t) \frac{\mu_0}{4\pi} \frac{2\pi r_{\text{loop}}}{d} \tag{4.7}$$

By rewriting and substituting this into Equation 4.3, Equation 4.8 is obtained, which is a formula for the current slope. This can be filled in with $100\,\text{V/m}$ from Requirement S-MR1, resulting in approximately $100\,\text{MA/s}$.

$$-\frac{dI}{dt} = \boldsymbol{E}(d,t) \frac{4\pi}{\mu_0} \frac{d}{2\pi r_{\text{loop}}} = 10^2 \cdot 10^7 \cdot \frac{3 \cdot 10^{-3}}{2\pi \cdot 5 \cdot 10^{-3}} \approx 0.1\,\text{GA/s} \tag{4.8}$$

Requirement S-MR3 specifies that the inductor may not heat up over 318 K. The temperature change ΔT in a inductor with mass m is depended on the amount of heat energy Q dissipated in the inductor and is depended on its material via the specific heat capacity C of the substance (in $\text{Jkg}^{-1}\text{K}^{-1}$), see Equation 4.9.

$$Q = mC\Delta T \tag{4.9}$$

For a wire loop with a loop diameter of 1 cm and a wire diameter of 1 mm, it can be found that 10 J (the maximum given by the Control subgroup in Chapter 5) of energy will heat the copper mass up by 117.5 °C. This is far beyond the required limit, but it is not realistic for the loop to heat up by this amount, since it is also connected to a larger copper mass in the form of the conductive paths that connect the capacitor and the switch. As the implementation of the conductive paths is part of the control circuit, it can be said that it is not of major importance to optimise the wire loop as an individual component, since the temperature increase is mostly dependent on the copper mass that the Control subgroup adds to the conductive paths.

Circular Loop Inductor in 1D

In 1D, the wire can be approximated as infinitely small. Starting from equation 4.1, a more detailed equation can be derived to calculate the magnetic vector potential. Using equation 4.10, the magnetic vector field potential can be calculated using r_{loop} and an input current $I(t)$ over time in spherical coordinates. Here the $\mathbf{r} = (\text{r},\phi,\theta)$ is the position vector from the origin to the observing point P. Vector $\mathbf{r}' = (\text{r}',\phi',\theta')$ points from to a location of the circular loop, in which r' is equal to r_{loop}. This can be seen in Figure 4.2 below. The E-field then follows from 4.3.

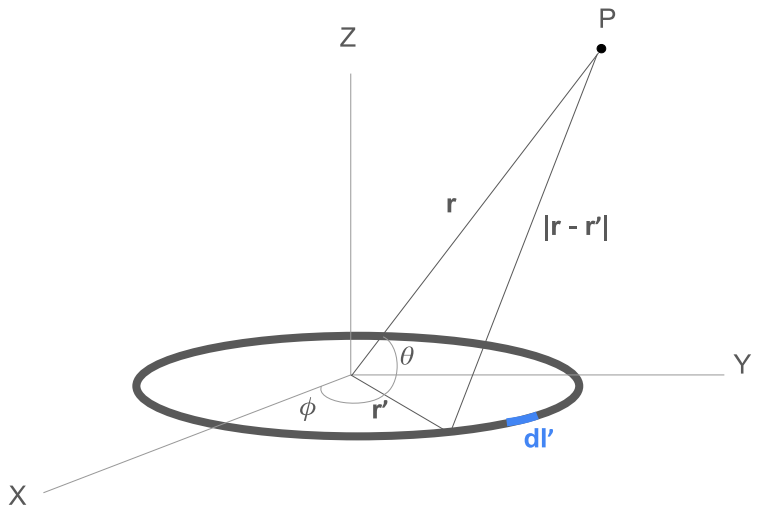

Figure 4.2: 1D Circle loop problem with spherical coordinates

$$\mathbf{A}(\mathbf{r},t)_{\text{1D}} = \frac{\mu_0 I(t)}{4\pi} \int_0^{2\pi} \frac{-r'\sin\phi'\hat{\mathbf{e}_\mathbf{x}} + r'\cos\phi'\hat{\mathbf{e}_\mathbf{y}}}{\sqrt{r'^2 + r^2 - 2r'r\sin\theta\cos\phi'}} d\phi' \tag{4.10}$$

Circular Loop Inductor in 3D

Instead of modelling the circular loop as a wire with an infinitesimal radius, it can also be modelled relatively simply as a 3D wire with a square-shaped cross-section. Just like with the 1D-model, this 3D-model starting with equation 4.2 can be derived more. For short distances (relatively to the wire radius), this model should be more accurate. Using cylindrical coordinates, the magnetic vector potential at a certain point in space $\mathbf{r} = (r, \phi, z)$ and in time t could then be calculated using 4.11, see Figure 4.3 below. The E-field then follows from 4.3. The inductor loop radius r_{loop} and wire radius r_{wire} can be given as input to this model, together with an in current through the loop $I(t)$ as function over time. This formula uses the approximation that the current density throughout the loop is constant.

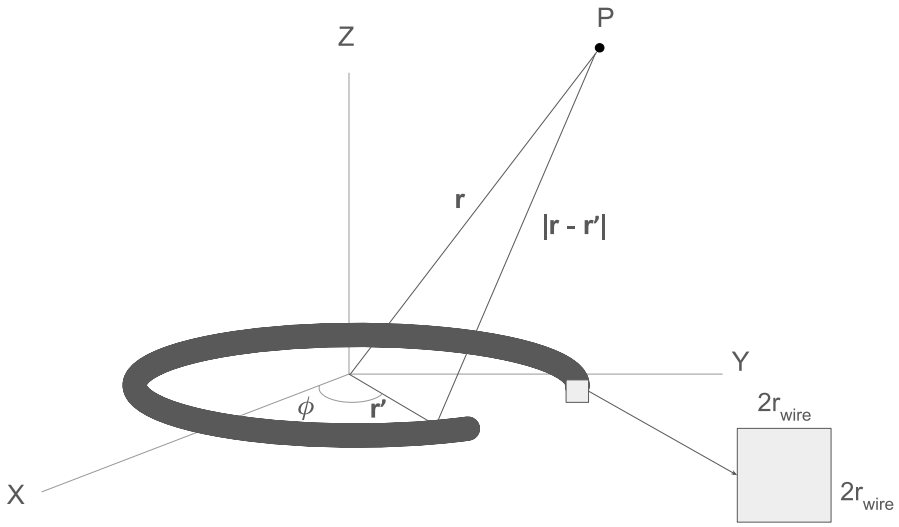

Figure 4.3: 3D Circle loop problem with cylindrical coordinates

$$\mathbf{A}(\mathbf{r},t)_{\text{3D}} = \frac{\mu_0}{4\pi}\frac{I(t)}{A_{\text{wire}}}\int_0^{2\pi}\int_{r_{\text{loop}}-r_{wire}}^{r_{\text{loop}}+r_{wire}}\int_{-r_{wire}}^{r_{wire}}\frac{\cos(\phi'-\phi)r'dzdrd\phi'}{\sqrt{r^2+r'^2-2rr'\cos(\phi'-\phi)+(z'-z)^2}} \quad (4.11)$$

Here, A_{wire} is equal to $(2r_{\text{wire}})^2$.

Comparing the 1D and 3D model

The result of the E-field of the 1D and 3D model can be seen in Figure 4.4 below. This simulation was modelled with the following parameters:

1. $\frac{dI}{dt} = 9.3GA/s$
2. $w_{\text{loop}} = 1cm$
3. $l_{\text{loop}} = 6cDm$
4. $d_{\text{between loops}} = 3mm$

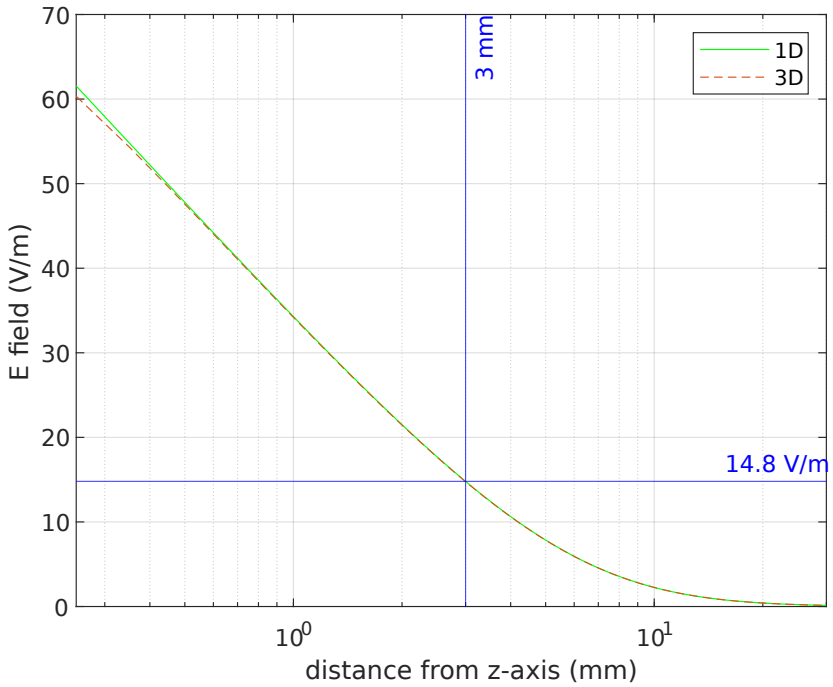

Figure 4.4: 1D vs. 3D modelled E-field over distance. With $\frac{dI}{dt} = 100MA/s, r_{\text{loop}} = 5mm$ and $r_{\text{wire}} = 0.2mm$. These two models are nearly identical, therefore the thickness of the wire does not have a significant effect on the E-field.

It can be seen that the simulated E-field curve of both of the models are nearly identical, from which can be concluded that the thickness of the wire does not have a significant influence on the E-field. Therefore, calculating the E-field can be done using either one of these models.

Stimulation Inductor Shape

For the inductor shape, it was looked at the differences between a circular loop and a square loop. The black arrows in left of Figure 4.5 show the magnetic vector potential along a circular loop carrying a certain current. This is then split in the x and y-components represented by the green and blue arrows. The influence of these components on the magnetic vector potential at the observing point *P1* are summed up. The following can be noted:

1. The influences of the components in the x-direction *l1* and *l3* are cancelled by the influences of *l2* and l4.

2. The influence of the red arrow in the y-direction has less influence on the observing point *P1* than the green arrow in the y-direction.

From the first point, it can be concluded that the components in the x-direction have no influence on the magnetic vector potential at the observing point *P1*, since there it always an "opposite pair" at a same distance to *P1* that will cancel it.
From the second point, it can be concluded that the further away the "cancelling" component in the y-direction from *P1*, the less of an influence it has on *P1*.
Knowing this, it was then looked at the influence of a square loop through which a current flows, has on magnetic vector potential the observing point *P2*. Since the components *l5* and *l6* in the x-direction cancel each other, only the two sides in the y-direction will have influence on the observing point*P2*.

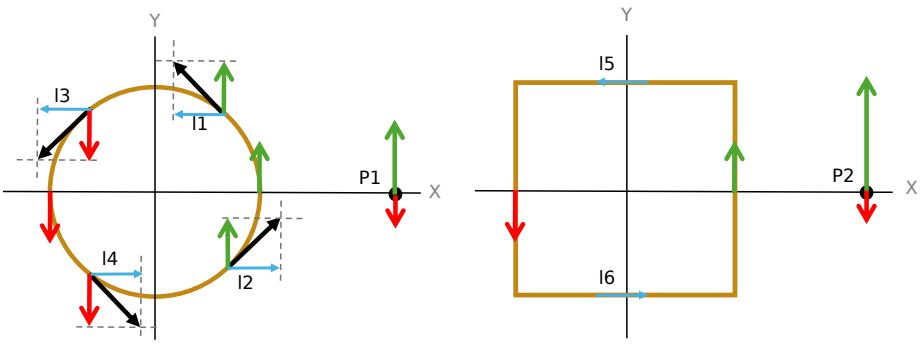

Figure 4.5: Influence of E-field on a point of circular loop vs. Square loop. The influence on the E-field at point P2 due to a square loop is more significant than the circular loop on P1

Square Loop Inductor

As mentioned in section 4.4.1 above, the geometry of an inductor impacts magnetic vector potential at the observation point greatly. A circular loop will produce a less strong influence on the magnetic vector potential at an observing point unequally distanced to all segments of the circular loop than that of an square inductor loop, see in Figure 4.5 the difference of P1 and P2. Therefore, it will also impact the E-field at the observing point. In Figure 4.6, the E-field is analysed at a distance 3 mm with $\frac{dI}{dt} = 9.3\,\mathrm{GA/s}$. This new current slope is feasable according to a new calculation by the Control subgroup (Chapter 5). It can be seen that the E-field is 221 V/m at a distance of 3 mm.

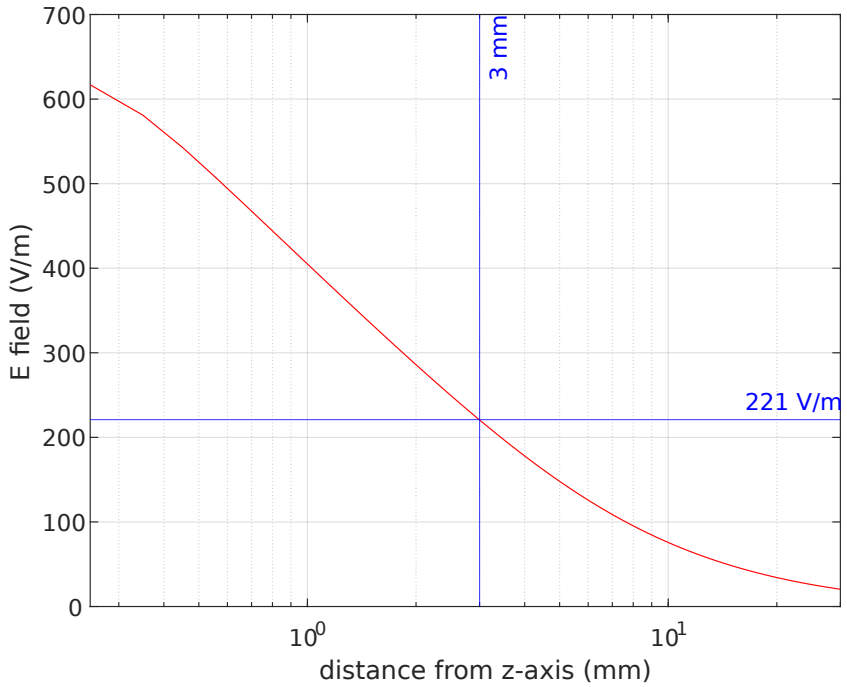

Figure 4.6: E-field of square loop inductor over distance. Simulated with $\frac{dI}{dt} = 9.3GA/s$. The square loop is modelled as two wire segments of 1 cm, separated by 6 cm, in which the current flows in opposite directions. At 3 mm from the inductor loop, the E-field is 221 V/m.

4.4.2 Measurement loop

To verify requirement S-MR1 a measurement loop is designed to measure the E-field. This measurement loop is placed on the opposite side of the stimulation inductor loop which can be seen in the Figure 4.7

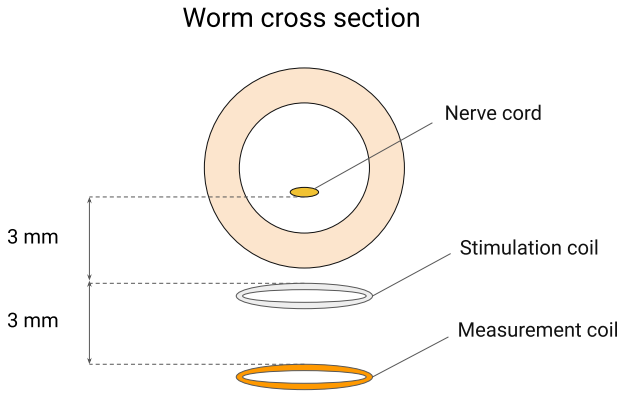

Figure 4.7: Measurement loop set-up. The measurement loop is placed at 3 mm from the stimulation inductor loop to simulated the resulting E-field at the nerve cord.

This measurement coil will pick up the induced voltage (emf) ε generated from the flux lines

from the stimulation coil. The relation of emf to flux lines is given by the following formula:

$$\varepsilon = -N\frac{d}{dt}\oint \mathbf{A}\cdot d\mathbf{s} \tag{4.12}$$

But since flux is also related to the E-field, the emf can also be expressed as:

$$\varepsilon = \int \mathbf{E}\cdot d\mathbf{s} \tag{4.13}$$

Therefore, the E-field at a distance of $3mm$ from the stimulation coil can be calculated from the emf measured at the oscilloscope.

4.4.3 Multiple Inductors Setup

Two Stimulation Inductors

Since the general mandatory requirement C-MR3 obligates the stimulation setup to contain at least two inductors. It was looked at how these two inductors would interfere with each other. From equation 4.1, the magnetic vector potential $\mathbf{A}(\mathbf{r},t)$ is calculated from the line integral of a certain structure. From Maxwell, it is known that:

$$\mathbf{B} = \nabla \times \mathbf{A} \tag{4.14}$$

The magnetic flux linkage between two structures l and k which can be seen in Figure 4.8 can be defined as:

$$\lambda(l,k) = \int_k \mathbf{B_l}\cdot \mathbf{da_k} \tag{4.15}$$

In which $\mathbf{B_l}$ represents the magnetic flux density created by structure l on the surface element $\mathbf{da_k}$ of structure k.
Using Stokes' theorem we can write the magnetic flux as:

$$\lambda(l,k) = \oint_k \mathbf{A_l}\cdot \mathbf{dk} \tag{4.16}$$

Then, combining 4.1 and 4.16, the magnetic flux linkage can be expressed as [22]:

$$\lambda(l,k) = \frac{\mu_0 I}{4\pi}\oint_k\oint_l \frac{\mathbf{dl}\cdot\mathbf{dk}}{|\mathbf{r}-\mathbf{r}'|} \tag{4.17}$$

In Figure 4.8 below, the layout of the two inductors can be seen. These two rectangular inductors have a width of 1 cm and 6 cm in height are placed 1 cm apart.

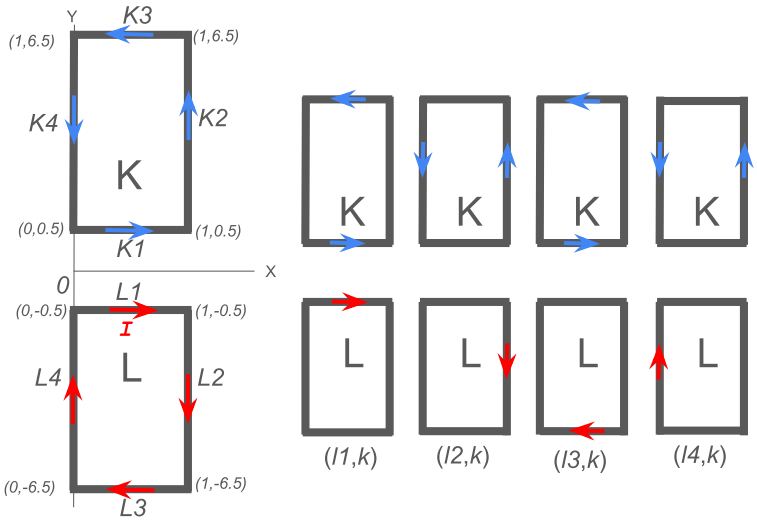

Figure 4.8: Partial flux linkage implementation

Here, the current I in structure l flows in the clock-wise direction, as can be seen by the red arrows. The blue arrows in structure k represent the direction in which the induced emf in structure k is measured. The directions of the arrows are important for determining the boundaries of the integrals for the magnetic flux linkage.

The magnetic flux linkage between structure l and k can be seen as the sum of the partial magnetic flux linkages between each of the segments $l_1 - l_4$ with structure k, this can be seen on the right of Figure 4.8. For example, the magnetic flux linkage between structure segment l_1 and structure k, is the sum between the influences between the segments l_1 with k_1 and k_3. It is important to note that since the magnetic flux linkage is the double integral of the dot product between the small integration elements **dl** and **dk**, only the segments that are not right angles to each other are considered.

The magnetic flux linkage between structure l and k can be expressed as following:

$$\lambda(l,k) = \sum_{\substack{i=1 \\ i=odd}}^{4} \sum_{\substack{j=1 \\ j=odd}}^{2} \lambda(l_i, k_{2j-1}) + \sum_{\substack{i=1 \\ i=even}}^{4} \sum_{\substack{j=1 \\ j=even}}^{2} \lambda(l_i, k_{2j}) \tag{4.18}$$

With the individual partial flux linkages being:

$$\lambda(l_i, k_j) = \frac{\mu_0 I}{4\pi} \oint_{l_i} \oint_{k_j} \frac{\mathbf{dl_i} \cdot \mathbf{dk_j}}{\sqrt{(x_{k_j} - x_{l_i})^2 + (y_{k_j} - y_{l_i})^2}} \tag{4.19}$$

From the magnetic flux linkage $\lambda(l,k)$, the mutual inductance and the induced emf ε can be calculated:

$$M(l,k) = \frac{\lambda(l,k)}{I} \tag{4.20}$$

$$\varepsilon = -M(l,k)\frac{dI}{dt} \tag{4.21}$$

As requirement G-TR2 obliges the two inductors to placed in different places, the effect on the lateral misalignment of the two inductors on mutual inductance and induced emf is studied. This is done is the following manner: initially, the structures l and k are perfectly aligned distanced from each other by 1 cm in the x-y plane. Then, a parallel translation of the structure k is done from -20 cm to +20 cm while the other structure does not move. This can be seen in Figure 4.9.

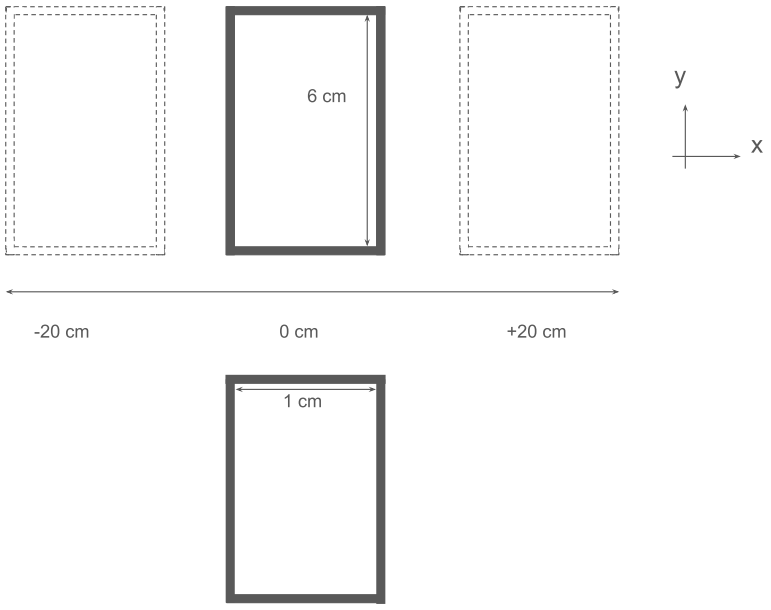

Figure 4.9: Lateral misalignment setup

Next, the requirement G-MR5 obliges the E-field's orientation to be adjustable with respect to the worm. studied. The adjustment of the E-field's orientation happens through the rotation of the structure k around its x-axis closest to the structure l. This is done by keeping structure l still and rotating structure k so that angular misalignment between the two structures ranges between 0 and 180°. This can be seen in Figure 4.10. The effect on the mutual inductance and the induced emf can be calculated again just like from the lateral misalignment from the magnetic flux linkages between each of the segments l_1 - l_4 with structure k.

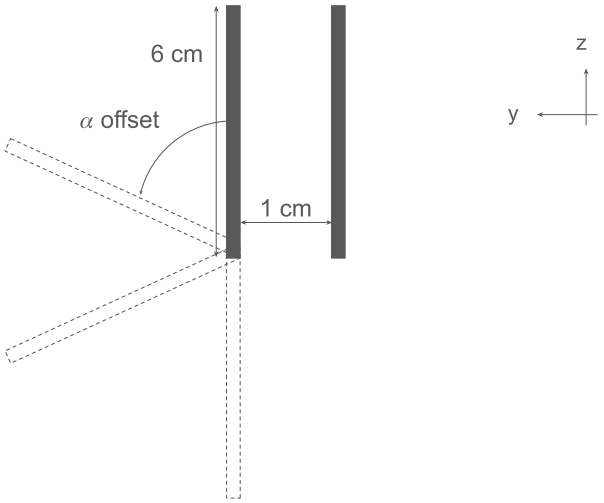

Figure 4.10: Angular misalignment setup

The influence on the mutual inductance and induced emf based on a $\frac{dI}{dt} = 9.3GA/s$ of both lateral and angular misalignment is shown below in Figure 4.11 and Figure 4.12 respectively. These two square inductor loops are placed 1 cm apart from each other, this done in order to simulate the two stimulation square loop inductor experiment in which the loops will be placed on both side of the worms body. This distance will be approximately 1 cm.

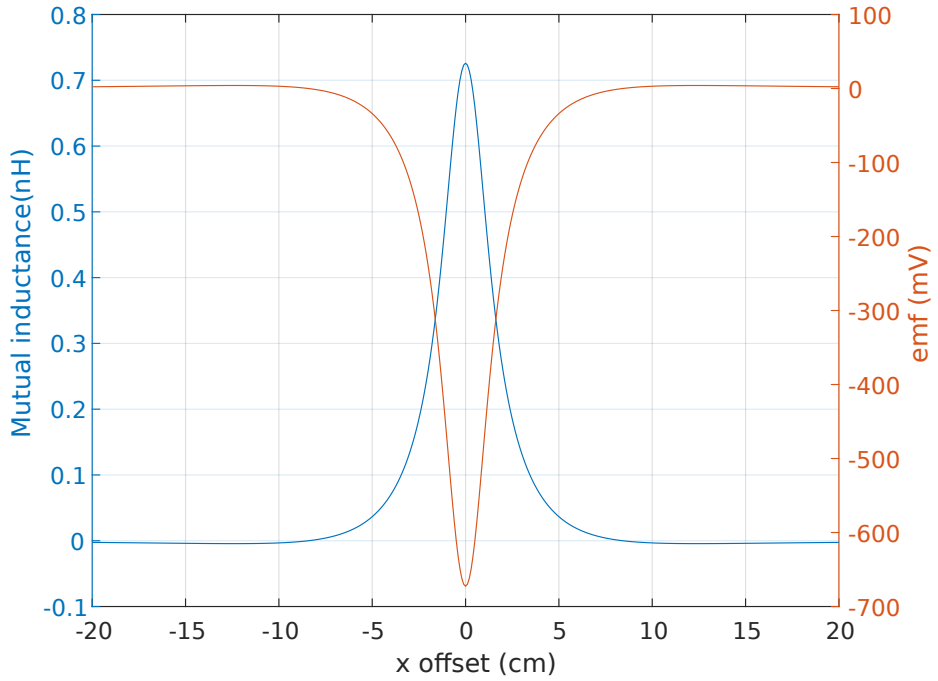

Figure 4.11: Lateral misalignment results between two square loop inductors of 1cm by 6cm, simulated using $\frac{dI}{dt} = 9.3GA/s$. These two square inductor loops are placed 1 cm apart from each other. The mutual inductance and the induced emf is determined while offsetting the square inductor loop from -20cm to +20cm in the x-axis direction. At offset 0cm the mutual inductance and the induced emf is the largest being 0.73 nH and -673 mV respectively.

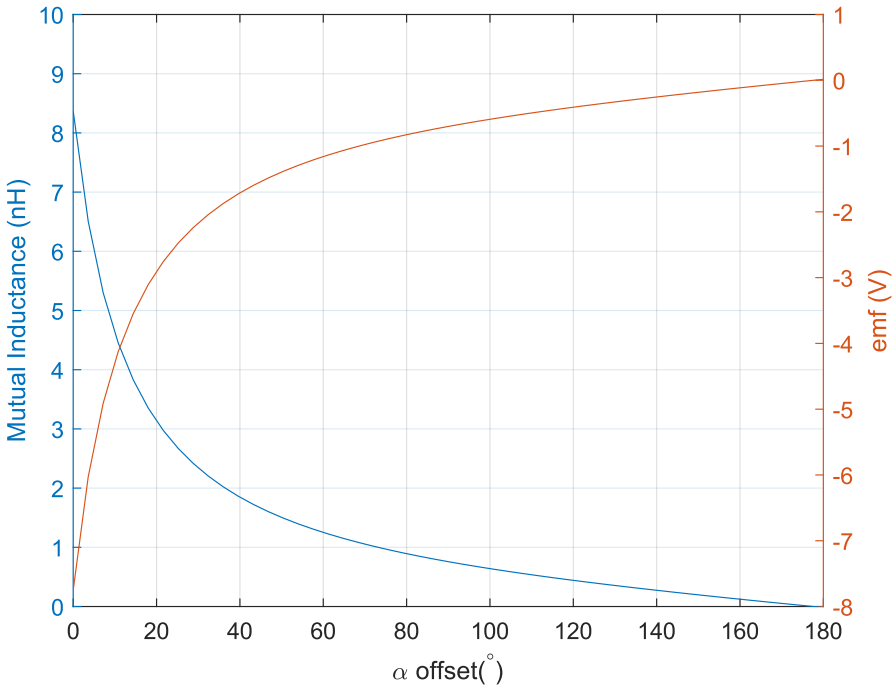

Figure 4.12: Angular misalignment results between two square loop inductors of 1cm by 6cm, simulated using $\frac{dI}{dt} = 9.3GA/s$. The mutual inductance and the induced emf is determined while offsettimg rotating one of the two square inductor loops from 0 to 180°. At an offset of 0°, the mutual inductance and induced emf is the largest being 8.4nH and -7.8V respectively.

The angular misalignment at an offset of 180° should be the same as the lateral misalignment of 6 cm. From the results of Figure 4.11 and 4.12 is derived that these values only differ by 1%. Therefore, it can be concluded that these models are almost the same and therefore give an good representation of the influence of the lateral and angular misalignment on the induced emf.

From Figure 4.11, it can be concluded that the induced emf is largest at 0 cm offset -673 mV. In section 5.6.1, the Control group established that the source voltage V_0 through which the stimulation loop is powered is 300V. The lateral misalignment at an offset of 0cm is only 0.2% of V_0 and therefore deemed insignificant.
More, from Figure 4.12, it can be seen that the induced emf is largest at 0° offset, being -7.8V. But since the source voltage V_0 is 300V, this is only 2.6%. Therefore, it can concluded that this deemed insignificant.

4.4.4 Determining the Focality

Requirement S-MR2 obliges the E-field to be half of the strenght at the stimulation site when measured 1 cm away. This is shown in the Figure 4.13 below. This analysis is done in the same way as in 4.11.

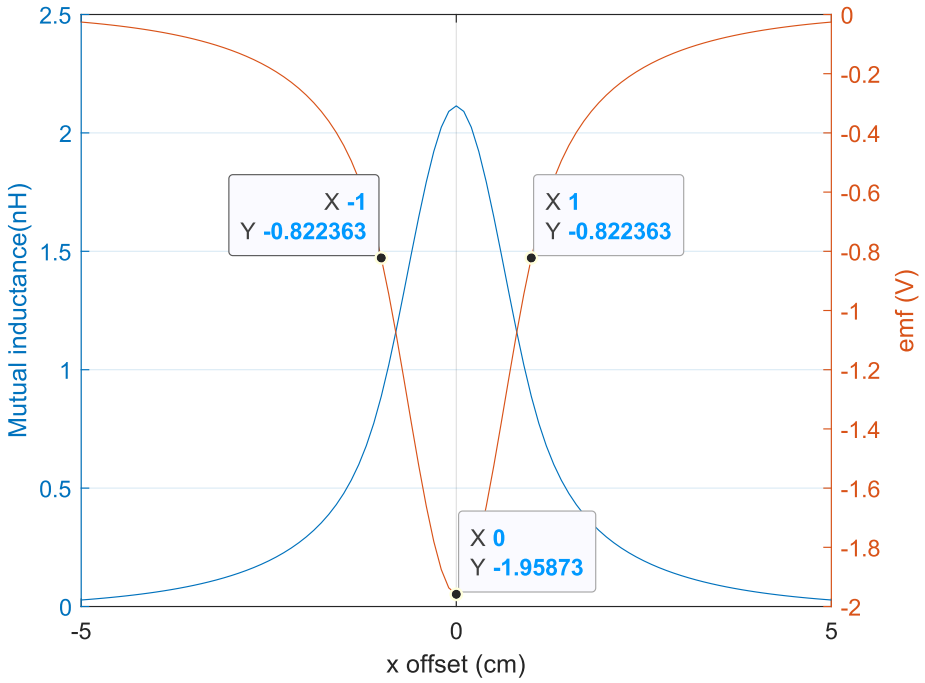

Figure 4.13: E-field strength of two square inductors distanced 3 mm away from each other. At 1cm offset left and right to that point the E-field decreases by 58%.

In Figure 4.13, it can be seen that at 1cm offset left and right to that point the E-field decreases by 58%.

4.4.5 From E-field to action potential

To address trade-off requirement G-TR1, it is essential to first have a understanding of the current knowledge regarding the mechanisms involved in inducing an action potential with an external electric field. The relevant mechanisms for optimising the design characteristics can be categorised into two primary aspects: the strength and duration of the electric field, and the excitation site and orientation of the electric field, see Appendix A.2. By drawing a parallel between research on pyramidal cells, which are extensively studied in the context of TMS, and the neurons of an earthworm, valuable insights can be gained. Research on pyramidal cells indicates that smaller pulse widths necessitate larger E-fields to elicit an action potential. Additionally, the current TMS pulses have a minimum duration of 30 µs. These findings introduce a new consideration for the current and inductor characteristics. Beyond the essential requirements for E-field strength and focality, there is now a trade-off requirement stipulating that the duration of the E-field should be maximised.

4.5 Design Choice

The analysis indicates that a maximum $\frac{dI}{dt}$ is required in an inductor positioned as close as possible to the worm, in order to get a maximum E-field. The inductor should for the same reason have the smallest possible inductance. As a trade-off, the $\frac{dI}{dt}$ must be sustained for the longest possible duration. The inductor characteristics include a copper, rectangular wire loop, with a short length of 1 cm. A $\frac{dI}{dt} = 9.3GA/s$ will be sufficient to get the desired E-field strength. The longer the control subgroup can maintain this slope, the greater the chances of provoking an action potential.

4.6 Implementation

In order to verify the analysis done on the stimulation inductor(s), the block diagram in Figure 4.1 can be updated in the following Figure 4.14 below, with the addition of the measurement loop mentioned in section 4.4.2 and the temperature test.

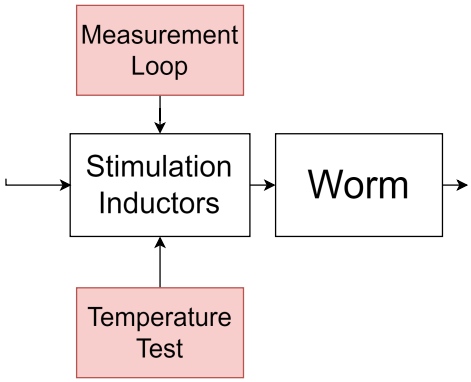

Figure 4.14: Segment of the design overview with tests that is dedicated to the stimulation subgroup.

The first test that will be performed is the Temperature Test. This test is done by measuring the temperature of the coil to evaluate whether Requirement G-MR4 is met. This can be done by an infrared thermometer.

The second test that is performed is the Measurement Loop. This will measure the EMF from which can be derived if Requirement G-MR1 is met. The Measurement Loop itself also needs to be tested to ensure it functions correctly and behaves according to theoretical expectations.

4.6.1 Test Setup

In order to measure the E-field distanced at d mm from the inductor loop, the following test set-up in Figure 4.15 is made.

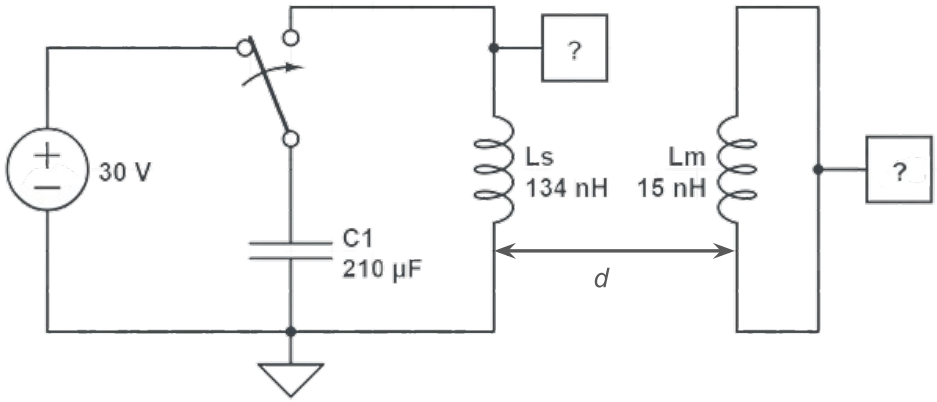

Figure 4.15: Test setup of the stimulation inductor loop and the measurement loop to measure the E-field at a distance d.

Here, the capacitor C1 is being charged to 30V by the power supply. Then, a switch is flipped to discharge it into the stimulation inductor loop Ls. This change in voltage is measured by an oscilloscope in Channel 1. A second channel is connected to the measurement loop, which is placed at d = 1cm away from the stimulation inductor loop. This will ensure there is an EMF induced in the inductor loop Lm, which can be used to derive the E-field.
The stimulation and the measurement loops were made from a copper tinned wire with a wire radius of 0.25mm. One roll of this costs 11.99 euros.

4.6.2 Realisation

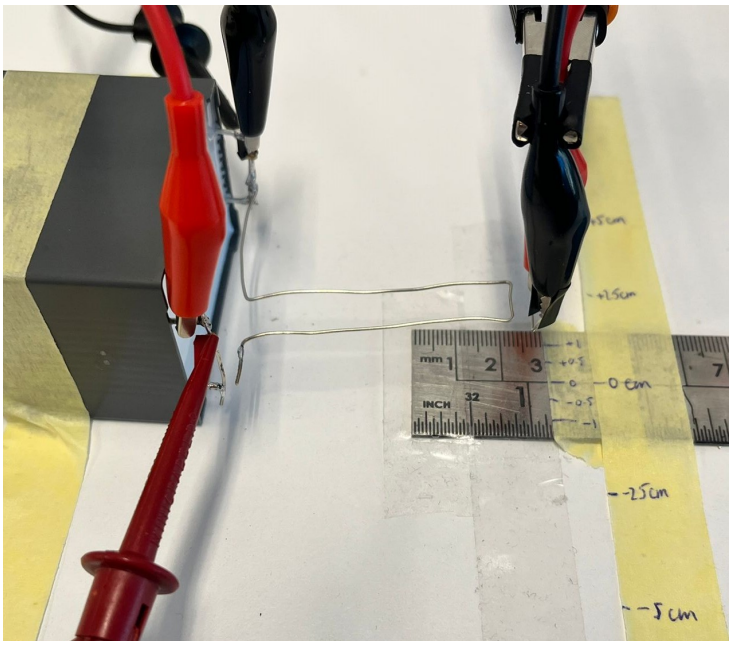

Figure 4.16: Realisation of the stimulation coil. This coil is rectangular and has a width of 1 cm and a length of 6 cm to mimic traces on the pcb.

Figure 4.17 shows a set-up with an extended stimulation inductor to mimic the traces on a PCB. A small measurement loop can be seen in the picture on the right. The measurement loop is oriented perpendicular to the stimulation inductor, in this way only the induced electric field in the plane of the stimulation inductor is measured.

4.7 Results

In this section the results of the tests are shown and a brief explanation is given about the results. Since only one of the tests was able to be performed, this will be presented in the section below.

4.7.1 Measurement Loop

To ensure the measurement loop works as intended, it is first tested by shorting the capacitor through a test stimulation coil and capturing the EMF with the measurement loop. The results are presented in Figure 4.17. Several things can be observed. CH1 is the voltage over the capacitor and thus also over the inductor. CH2 is the measured induced emf in the measurement loop. An oscillation occurs due to the resonance of the capacitor and the inductor. The peak induced emf is 200 mV. The $\frac{dI}{dt}$ can be estimated in two ways. The first method involves

estimating the second time derivative of the voltage across the capacitor and inductor, see Equations 4.22 and 4.23.

$$I = C\frac{\Delta V}{\Delta t} = 210 \cdot 10^{-6} \cdot \frac{15}{5 \cdot 10^{-6}} = 610\,\text{A} \tag{4.22}$$

$$\frac{\Delta I}{\Delta t} = \frac{610}{3.5 \cdot 10^{-6}} = 174\,\text{MA/s} \tag{4.23}$$

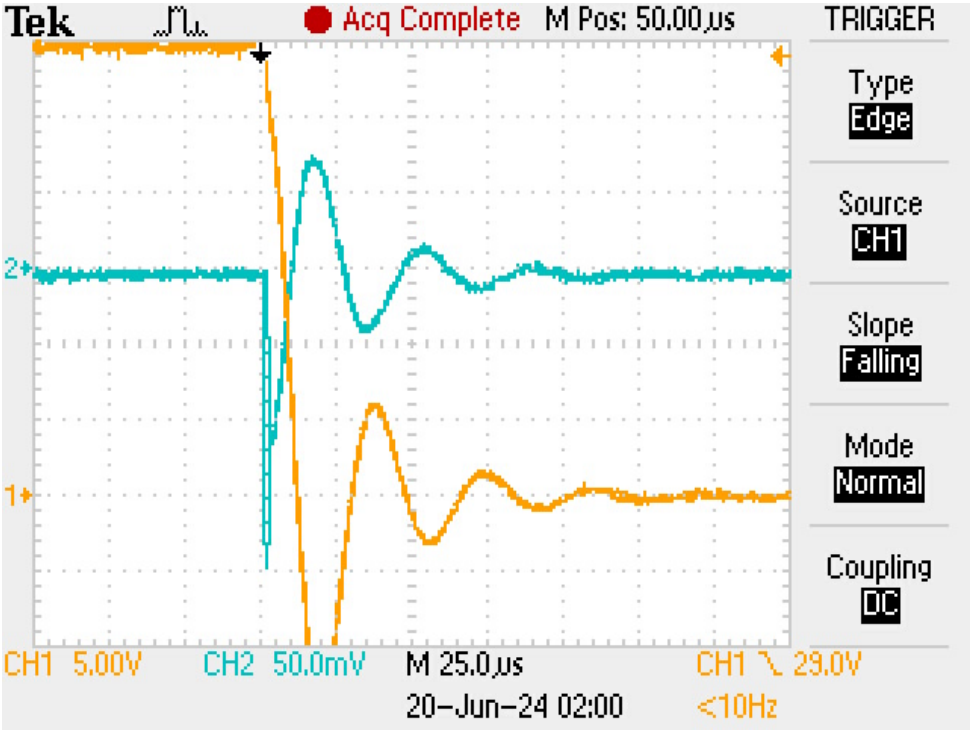

Figure 4.17: Data from simple implementation setup. With CH1 (yellow) being $V_C = V_{\text{L-stimulation}}$ and CH2 (blue) being $V_{\text{L-measurement}}$. As expected, the measured field is the derivative of the stimulation pulse. From the data an E-field of 28.6 V/m can be derived with an $\frac{dI}{dt}$ of approximately 180 MA/s.

Through visual inspection, a value of approximately 37 µs can be extracted for the resonant frequency of the waveform in Figure 4.17. Using the available information about the rest of the circuit, an approximation of the maximum dI/dt can be made.

$$\frac{dI(0)}{dt} = \frac{V_0}{L} = \frac{V_0}{\left(\left(\frac{2\pi}{T_0}\right)^2 C\right)^{-1}} \tag{4.24}$$

$$\frac{30}{\left(\left(\frac{2\pi}{37 \cdot 10^{-6}}\right)^2 210 \cdot 10^{-6}\right)^{-1}} = 181\,\text{MA/s} \tag{4.25}$$

Evaluating Equation 4.24 with an initial voltage of 30 V and a capacitance of 210 µF yields a dI/dt of 181 MA/s.

Both calculations estimate around 180 MA/s. By giving this as input to the model and comparing the result with the EMF, the model can be validated. The model estimates an electric field of 28 V/m at 5 mm distance and 18 V/m at 10 mm distance. Since the measurement loop had only one piece of 7 mm wire (l), the E-field strength can be estimated by Equation 4.26.

The result of this calculation is, especially with measurements errors due to the 6 setup, close to what the model predicts.

$$E = \frac{\text{emf}}{l} = \frac{200 \cdot 10^{-3}}{7 \cdot 10^{-3}} = 28.6V/m \tag{4.26}$$

4.8 Discussion

Due to difficulties with implementing the total design and the testing being completely dependent on the Control subsystem, none of the tests could be performed on the realised design. It was however confirmed that the measurement loop works as intended, indicating future research on this topic is recommended.

4.9 Conclusion

This chapter addressed the question: **"What inductor and pulse characteristics are necessary to induce the desired electric field for neuronal stimulation purposes?"** After a thorough analysis of possible design solutions, a solution was chosen that best fitted the program of requirements. This solution consist of the following inductor and pulse characteristics:

1. $\frac{dI}{dt} = 9.3GA/s$
2. Inductor geometry = square loop with a side length of 1 cm

It is also established from modelling the E-field based on an 1D and 3D model, that the thickness of the wire does not impact the E-field significantly.
Due to difficulties implementing the test-setup, the requirements mentioned in 4.2 were only verified using simulations. From this can be concluded that all requirements are met, an overview is given in Table 4.1.

Requirement:	Achieved:	Value:
S-MR1	Yes	221 V/m
S-MR2	Yes	The E-field at 1cm is decreased by 58%
S-MR3	Not tested	-
S-MR4	Yes	The maximum influence of lateral and angular misalignment is only 2.6%
S-MR5	Yes	11.99 euro
G-TR1	Not tested	-
G-TR2	Yes	

Table 4.1: Overview of the requirements from the PoR achieved with values

Chapter 5

Control

5.1 Introduction

When attempting to evoke a measurable response in the neuronal activity of a worm by means of stimulation with an induced electric field, a specific kind of circuitry is required to obtain the desired electrical characteristics that are necessary for generating an action potential. From this the main objective of the control subgroup can be derived, which is to design, build and test the control circuitry that will be used to power the stimulation inductor. The related Programme of Requirements that follows from this objective contains requirements that can be divided into two main categories that are concerned with the following derived objectives:

1. The electronic components within the circuitry must be chosen such that their resulting voltage, current and time characteristics are in accordance with the desired pulse characteristics.

2. The circuitry must be designed in such a way that the safety of the end-user can be guaranteed.

Additionally, ease-of-use is a highly valued metric for the final product, and as such a secondary objective, that has been defined through a trade-off requirement, has been established, which comes in the form of enabling the circuitry to be controlled remotely by means of integrating a microcontroller.
Since the main objective includes the use of a dual inductor setup, another degree of complexity is added due to the increased demands for the accuracy and consistency of the product. The addition of a second inductor with fully independent control allows for an increased amount of testing options and variability. This added variability necessitates careful consideration for the design of the control circuitry to ensure accuracy and consistency, which is of major importance with regard to the quality of the measurements.

5.2 Programme of Requirements

Designing pulse generating circuitry requires careful consideration of several aspects, that, as was stated in the Introduction, can be divided into two categories. The system requirements that follow from these aspects are based on general requirements G-MR1, G-MR4, G-MR5, G-MR6, G-MR7, G-MR8, G-MR9, G-MR13, G-MR14. The rest of this section contains the system requirements and the reasoning behind their inclusion.

Mandatory Requirements

GC-MR1 | The product must provide the user with separate timing controls for each inductor.

C-MR1 | The shortest interpulse duration of a multi-coil setup must be shorter than the pulse period.

C-MR2 | No capacitors must be able to store more than 10 J.

C-MR3 | Every capacitor that is able to store more than 1 J at a voltage above 10 V must have the ability to be discharged at any time through a dump resistor.

C-MR4 | Any conductor, shielded or not, that is able to have a voltage of more than 60 VDC over it when in use, must be contained within an insulated enclosure.

C-MR5 | Any insulated enclosure, containing hazardous circuitry, must not have any opening or holes with a diameter of 10 mm or more.

C-MR6 | When setting a desired voltage over a pulse capacitor, the error margin must be 5% of the maximum voltage.

C-MR7 | Pulse capacitors must be able to be charged to their desired voltage in less than 10 s.

C-MR8 | Pulse capacitors must be able to be discharged below 10 V within 10 s.

C-MR9 | The control circuitry must be able to send a current pulse with a dI/dt of at least 100 MA/s through a stimulation inductor.

C-MR10 | The conductors of the circuit connected to the stimulation inductor must not exceed 318 K.

C-MR11 | The total cost of the design must be less than €750,-.

Trade-off Requirements

TR1 | The control circuit should be remotely controllable as an HTTP server.

Control Requirements GC-MR1 and C-MR1 follow from general Requirements G-MR7 and G-MR8, which state that the setup must contain at least two stimulation inductors, with separate control over the timings. The addition of extra coils enables the user to test the effect of spatial and temporal variation of pulses. Mainly the use-case where it is desirable to test whether or not two sub-threshold pulses can lead to the additive equivalent effect of a single supra-threshold pulse by being able to create an action potential is of importance to this system requirement. Summing multiple pulses requires that the interpulse duration of a multi-coil setup is shorter than the pulse period.

Requirement C-MR2 is concerned with the safety of the user, and is derived from Requirement G-MR9. The control circuitry will require voltages above the practical safe limit of 60 V, which means that there is a possibility for the pulse capacitors to contain amounts of potential energy that are able to cause serious harm to the user if the circuitry were to malfunction, which could result in a failure mode of the capacitors, potentially an explosion. A limit of 10 J has been selected to mitigate the effects of the worst case result of an explosion.

Requirement C-MR3 results from a similar path of reasoning as requirement C-MR2. Below the limit of 10 J, capacitors can still be a serious shock hazard when they are charged above the practical safe limit of 60 V. When the circuitry is not in use, the user should be able to safely utilise the physical product, and as such the capacitors must be able to be discharged at any time, to prevent the user from being shocked outside of operational procedures.

Requirements C-MR4 and C-MR5 have similar objectives, stemming from Requirement G-MR9, and are also concerned with preventing harm to the user. As opposed to Requirement

C-MR3, which is concerned with user safety outside of operational procedures, these requirements are concerned with the safety during operational procedures. Due to the potential energy of the capacitor, and the general shock hazard of the entire circuitry due to voltages above 60 V being used, it is wise to prevent the user from being able to touch any of the circuitry during normal operation. This is realised through the use of proper shielding and insulation, and the addition of an insulated enclosure that is not accessible unless it is properly and intentionally opened. This should prevent any limbs from unintentionally entering the insulated enclosure during normal operation. The specified diameter of 10 mm is roughly based on IP 2x, which states an object is protected from finger-based intrusion as long as any holes present in the object have a diameter of less than 12.5 mm.

Requirements C-MR6 and C-MR7 pertain to the charging process of the pulse capacitors, and, respectively, they are based on Requirements G-MR6 and G-MR13. These general requirements state that stimulation must occur within 1 minute, starting from the moment of sedation, and the electric field strength must be adjustable in steps of 10 mV/mm. By being able to accurately regulate the the pulse capacitor voltage within an error margin of 5%, the electric field strength can be adjusted with a maximum step size of 10 mV/mm. This value can be verified by making a measurement over the capacitor during the tests. Secondly, a maximum charge time of 10 s should offer the user enough breathing room to stimulate the worm within 1 minute of the sedation being applied, as charging the pulse capacitors is by far the most time-consuming part of the process of creating a pulse. Additionally, the 10 s has been chosen, such that there is an opportunity to conduct multiple tests within the 1 minute time window, and the required charge rate is realistically attainable with widely available power supplies.

Requirement C-MR8 also follows from the safety Requirements G-MR9, and is related to Requirements C-MR2, C-MR2. In case of failure, the capacitors should be unconditionally discharged to a level that could not cause harm. The value of 10 s should be plenty of time to let the capacitor discharge to a safe voltage before the user is able to touch the circuitry after the power has been disconnected.

Requirement C-MR9 directly results from general requirement G-MR1. Research from the stimulation subgroup has shown that this value should be sufficient to achieve an induced electric field strength of 100 V/m when a wire loop with a loop diameter of 1 cm and a wire diameter of 0.4 mm.

Requirement C-MR10 is related to Requirement G-MR4. The temperature of 318 Kelvin was chosen when considering the temperature of tissue damage. While the general requirement is based on the temperature of the coil, it was deemed that the conductors connected to the inductor should also stay below this value, to ensure that they would not dissipate heat into the inductor up to unsafe temperatures.

Requirement C-MR11 follows from Requirement G-MR14. Since the total budget for the project is $1000, -$, it was decided that the budget could be split between control and recording. The largest portion goes to control, as high power components are more expensive.

Finally, Requirement TR1 has been added as a quality-of-life functionality that enables the user to remotely control the control circuitry. This removes the need for manual control that would consist of physically following a predetermined set of operations to obtain the desired testing parameters. The addition of a microcontroller that can be remotely controlled through an HTTP server allows the user to execute the entire testing procedure through any device with a functional WIFI connection. When the microcontroller is used for making measurements, separating the datastream from the system log information stream not only makes the product more robust, but it also becomes more manageable to use, and to debug. Additionally, making

changes to the program is more easily done on a preconceived HTTP architecture, then on a serial communication protocol, so that less programming skills are required to adapt the system.

5.3 Possible Solutions for Design

Determining the setup requires that some comparisons are made between a variety of implementable approaches. The final system should be able to accurately charge and discharge two separate capacitors, where accuracy is mainly required for the timing and the amount of charge. User safety is also of major importance when considering the different design solutions. To delineate the different aspects of the design, a block diagram was made, found in Figure 5.1. Each block has its own design considerations, and the rest of this section will elaborate further on how each and every design choice is affected by the system requirements. The red blocks indicate the tests that signify if the system functions.

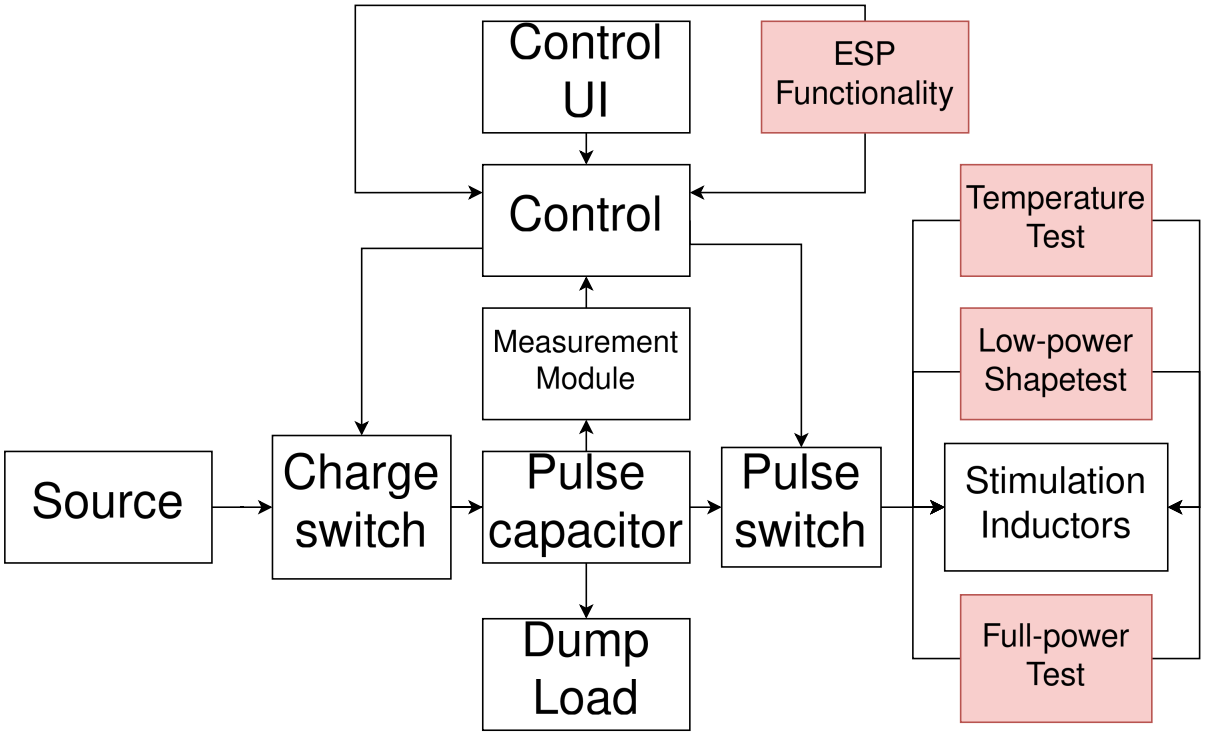

Figure 5.1: Segment of the design overview dedicated to the control subgroup. The red blocks indicate the tests.

5.3.1 Testing

To ensure that the system functions as intended, the following tests are drawn up.

1. ESP Functionality: Test if the timers of the microcontroller are accurate.
2. Low-power Shapetest: Test if the pulse characteristics are as expected before driving the voltage up.
3. Full-power Test: Drive up the voltage to the limits of the circuit components, and determine the maximal power for stimulation.
4. Temperature Test: Test if the stimulation inductor stays below a damaging temperature, also when the pulses are fired in quick succession.

5.3.2 Pulse generation

The industry standard for generating a short high current pulse through an inductor is to charge a capacitor to a relatively high voltage, and then discharge it in the shortest amount of time that is realistically possible[23]. This process is limited by the peak current rating of the pulse capacitor. This means that TMS pulse generation circuits can be analysed as simple RLC oscillators.

Requirements C-MR2 and C-MR9 are the most relevant requirements for the selection of the RLC values. Respectively, they state that the pulse capacitors must not be able to store more than 10 J, and that the system must be able to create a current pulse with a dI/dt of 100 MA/s through a wire loop that has a loop diameter of 1 cm and a wire diameter of 0.4 mm. Since the Stimulation subgroup will be producing multiple coils, it is wise to not aim exactly for the limit, but to see it as a minimum threshold value. Tracing it back even further, this system requirement was based on general requirement G-MR1, which states that the system must be able to induce an electric field strength of 100 $\mathrm{V\,m^{-1}}$ at a certain distance. This value was chosen, as this electric field strength should be capable of triggering an action potential in a neuron of a worm. There are no drawbacks to inducing a greater electric field strength if the triggering of an action potential is the main goal. There is, however, a limit to how high the current through the inductor can be, as there is a limit of 10 J for the potential energy of the pulse capacitors. To find out what component values are required to create the desired current pulse, it is useful to analyse the behaviour of a simple series RLC network.

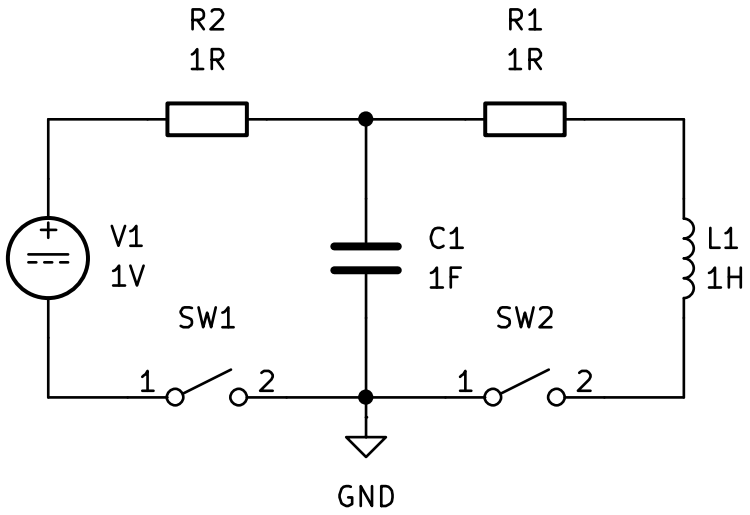

Figure 5.2: Simple RLC network with charging loop

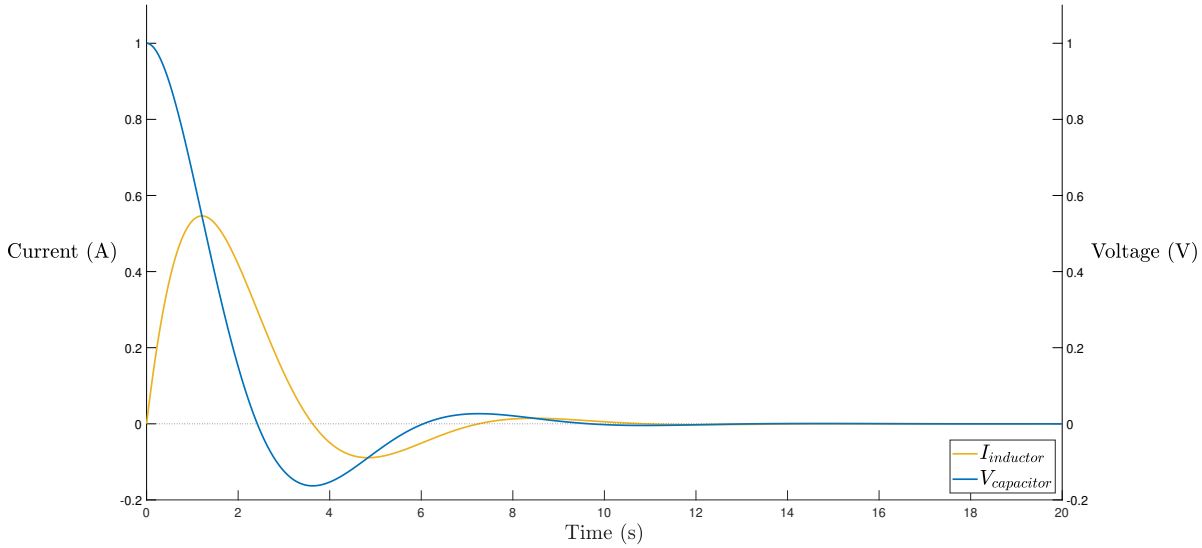

Figure 5.3: Voltage over capacitor $C1$ of Figure 5.2 (blue) and current through inductor $L1$ (yellow) as a function of time, using $C1 = 1\,\mathrm{F}$, $R1 = 1\,\Omega$ and $L1 = 1\,\mathrm{H}$. At these values the circuit is underdamped, resulting in a biphasic pulse.

The circuit schematic that is presented in Figure 5.2 shows a network with two connected loops. If it assumed that the switches are normally open, then closing switch SW1 for some time should lead to charge accumulating on the plates of capacitor C1. Next, if it assumed that after a near infinite amount of time switch SW1 is opened again, capacitor C1 should have reached a voltage equal to that of the DC source, which in this case is 1 V, and the capacitor should stay at that voltage until switch SW2 is closed. Closing this switch will cause the capacitor to discharge through the right loop, which will result in a pulsed current flowing through the inductor in the form of a damped cosine. These current and voltage characteristics have been plotted as a function of time in Figure 5.3.

To reveal the effect of the RLC values on the current characteristics, a transient analysis can be performed. By taking the right loop of Figure 5.2, finding the impedance of each of the components in the series configuration, and substituting s for $j\omega$, the following equation can be found:

$$V(s) = I(s)\left(R + Ls + \frac{1}{Cs}\right) \tag{5.1}$$

Solving for $I(s)$ with $V(s)$ chosen as an unknown constant gives the following solutions after an inverse LaPlace transform:

$$I(t) = \frac{V}{L\sqrt{|\alpha^2 - \omega_0^2|}} \cdot e^{-\alpha t} \sin\left(\sqrt{|\alpha^2 - \omega_0^2|} \cdot t\right) \quad \{\xi < 1\} \tag{5.2}$$

$$I(t) = \frac{V}{L\sqrt{|\alpha^2 - \omega_0^2|}} \cdot e^{-\alpha t} \sinh\left(\sqrt{|\alpha^2 - \omega_0^2|} \cdot t\right) \quad \{\xi > 1\} \tag{5.3}$$

Where:

$$\alpha = \frac{R}{2L} \tag{5.4}$$

$$\omega_0 = \frac{1}{\sqrt{LC}} \tag{5.5}$$

$$\xi = \frac{\alpha}{\omega_0} \tag{5.6}$$

Respectively, α represents the damping coefficient and ξ represents the damping factor. The latter, which is affected by the ratio of α and ω_0, determines whether Equation 5.2 or Equation 5.3 should be used. Figure 5.3 shows the current characteristics of a series RLC network that is underdamped, as it contains a biphasic sinusoidal current pulse, which means that ξ should be less than one. By substituting the component values of Figure 5.2 in Equations 5.5, 5.4 and 5.6, the following can be stated:

$$\xi = \frac{\alpha}{\omega_0} = \frac{\left(\frac{R}{2L}\right)}{\left(\frac{1}{\sqrt{LC}}\right)} = \frac{\left(\frac{1}{2 \cdot 1}\right)}{\left(\frac{1}{\sqrt{1 \cdot 1}}\right)} = \frac{1}{2}\sqrt{2} \approx 0.71 < 1 \tag{5.7}$$

Indeed, Equation 5.7 shows that ξ is less than one for the circuit shown in Figure 5.2, which gives the analytic proof for the biphasic current waveform. By making even the slightest change to this network, the damping can be drastically altered. For example, if the value of R is changed from $1\,\Omega$ to $4\,\Omega$, the damping factor becomes greater than one, and the current pulse becomes monophasic, as can be seen in Figure 5.4.

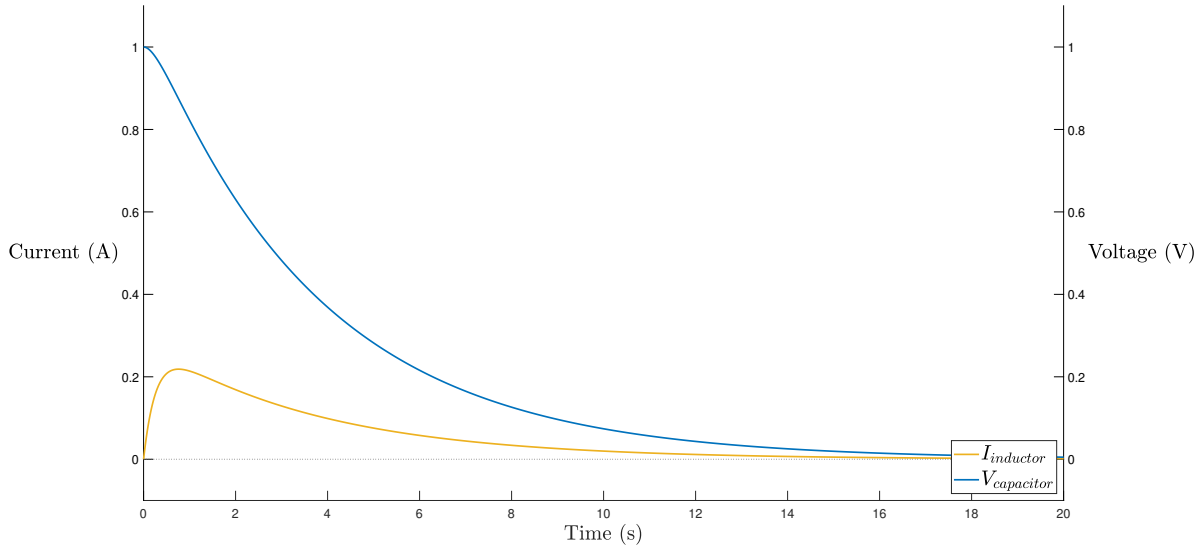

Figure 5.4: Voltage and current characteristics of the simple RLC network with monophasic behaviour

The expression that was obtained halfway through Equation 5.7 can be simplified to find out in what way the circuit component values affect the damping factor.

$$\xi = \frac{\left(\frac{R}{2L}\right)}{\left(\frac{1}{\sqrt{LC}}\right)} = \frac{R\sqrt{C}}{2\sqrt{L}} \tag{5.8}$$

From Equation 5.8 it can be seen that both the series resistance and series capacitance are proportional to the damping factor, while the series self-inductance is inversely proportional to the damping factor.

It might seem like the waveform characteristics are a rather arbitrary property when optimising for the maximum induced electric field, but here it is important to consider the application of the realised pulse generation circuit. Literature shows that in standard TMS applications, biphasic current pulses have a lower threshold than monophasic pulses when attempting to elicit a response in motor neurons[24]. Additionally, biphasic current pulses could be preferred over monophasic pulses due to their increased efficiency, as after a single period, biphasic setups will still retain some of the input energy in the capacitor as the oscillation causes the discharged capacitor to partially recharge again[25]. The opposite occurs in monophasic setups, where a single pulse will be generated and the system will not resonate due to the Ohmic losses of the total series resistance. In this case, however, it is preferred to use a monophasic current pulses, as the stimulation subject is a nerve cord of a worm. These consist of neurons that are connected lengthwise in a single direction along the worm, as is explained in Appendix A.1. As opposed to general TMS applications, where it is of lesser importance what neurons are stimulated in a cluster as long as some neurons are stimulated, when stimulating a worm it is desirable to have strong unidirectional characteristics for the induced electric field. It is thought that monophasic setups are superior for this application[24].

When compared to the damping ratio, it is much less clear how the RLC values affect the shape of the current pulse, which also follows from Equations 5.2 and 5.3, where it can be seen that the RLC values are present in denominators, exponents and trigonometric functions. It is clear that the voltage is directly proportional to the current, and up to a certain point the inductance should be inversely proportional to the current. Since further conclusions are difficult to make just by inspecting these equations, it can be useful to calculate the positive extreme values for the current through a wide range of different RLC series networks. By taking the derivative of Equations 5.2 and 5.3, and solving for t when the derivative is set to be equal to zero, the following equations can be found:

$$t = \frac{\arctan\left(\frac{\sqrt{|\alpha^2-\omega^2|}}{\alpha}\right) + \pi n}{\sqrt{|\alpha^2-\omega^2|}} \quad \{\xi < 1\} \tag{5.9}$$

$$t = \frac{\operatorname{arctanh}\left(\frac{\sqrt{|\alpha^2-\omega^2|}}{\alpha}\right) + \pi n}{\sqrt{|\alpha^2-\omega^2|}} \quad \{\xi > 1\} \tag{5.10}$$

Taking $n = 0$ and substituting the resulting value in Equations 5.2 and 5.3 gives the positive extreme value for the current. By varying a single RLC value at a time, and keeping the rest at a static value while the other parameter is being varied, a rough indication can be obtained of the relation of the RLC values in a series network to the positive extreme value of the current.

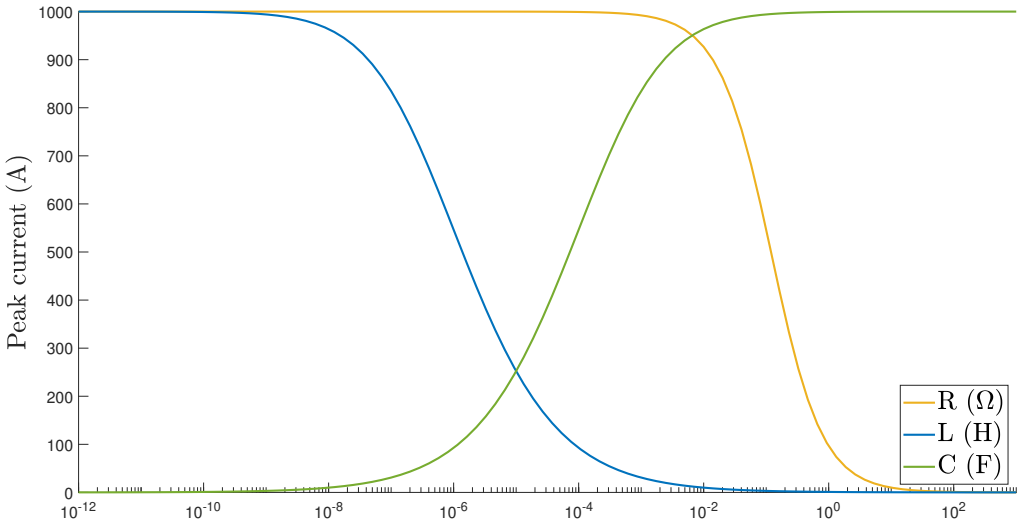

Figure 5.5: Relations of RLC values to the positive extreme current value with RLC series network values 100 V, 100 mΩ, 1 µH and 100 µF. One of the RLC values is varied at a time, with the x-axis representing either the resistance (Ω), the inductance (H) or the capacitance (F), while the rest is kept at the aforementioned values. The graph shows that increasing the capacitance will also increase the peak current, while increasing the resistance or the inductance has the opposite effect.

Figure 5.5 shows that minimising the series resistance and self-inductance while maximising the series capacitance is the key to maximising the current through the inductor. Keeping general requirement G-TR1 in mind, there is a slight preference for monophasic behaviour, which also requires the series inductance to be minimised and the series capacitance to be maximised, but here it is desirable to increase the series resistance instead of decreasing it. Increasing the resistance has the drawback of lowering the peak current, and since there is a mandatory requirement pertaining to the minimum achieved current through a specific inductor, it might still be beneficial to aim for biphasic behaviour.

rete

5.3.3 Charge/discharge loops

The charging and discharging process of the capacitor is a part of the system that is much simpler as its requirements are less strict. The charging process is only really limited by the charging time, which, as is stated by Requirement G-MR7, is a maximum of 10 s. Pushing the charging time towards the order of magnitude of several milliseconds or less is convenient when it is desirable to be able to use pulse trains, which is used for rTMS (repetitive TMS). There is, however, no requirement for this, and such a charge timing makes the process of accurately charging the capacitor to different voltages more complex, as there are limitations to reducing the delay of timed microcontroller outputs and the fall time of switches. Additionally, a shorter charging time also means that the current flowing through the capacitor moments after closing the switch will be significantly larger. Physical switches, unlike their ideal counterparts, have parasitic self-inductances, and these will cause voltage spikes if the switch is opened while current is still flowing through the switch, as they will try to oppose the sudden change in current. Care should be taken to prevent these voltage spikes from becoming larger than the rated voltage of the switch, as not doing so could permanently damage the switches and render them unusable.

$$V = L\frac{dI}{dt} \tag{5.11}$$

It is well known, that the voltage and current characteristics of an inductor can be described by the relation that is stated in Equation 5.11. From this equation, it can be concluded that greater voltage spikes will be generated if there is a larger change in current over time. In practice, these voltage spikes can be almost completely avoided by letting the capacitors charge past five time constants, after which the change in current will be either zero or close to zero. Requirement G-MR6, however, requires that the electric field strength is adjustable in steps of $10V/m$. This could be achieved by changing the output voltage of the voltage source that charges the capacitor, but this is unpractical when multiple tests are to be run in quick succession. This means that the more practical option would be to not let the capacitor charge for five time constants, which means that voltage spikes are unavoidable. The safest approach to this problem is to ensure that it is impossible to create a voltage spike large enough to damage the switches.

$$I(t) = \frac{V_s}{R}e^{-\frac{t}{RC}} \tag{5.12}$$

$$\frac{dI(t)}{dt} = -\frac{V_s}{R^2C}e^{-\frac{t}{RC}} \tag{5.13}$$

$$-\frac{L_p V_s}{R^2 C} < V \tag{5.14}$$

Equation 5.12 describes the current through a capacitor in a series RC network, where the capacitor is being charged by a DC voltage source. By taking the time derivative of this equation, evaluating the function at $t = 0\,\mathrm{s}$ and substituting the resulting parameters in Equation 5.11, Equation 5.14 can be formed. Choosing component values in compliance with this inequality ensures that no voltage spike will ever be greater than the rated voltage of the switch. This follows from the fact that the time derivative of the current through the capacitor has its greatest absolute value at $t = 0\,\mathrm{s}$, since it scales with a factor e^{-x}.

Discharging the capacitor, assuming that this is not done through the stimulation inductor, is an important safety measure. Requirement C-MR8 states that the capacitor must be able to be discharged within 10 s, but similar to the case of the charging process it is not practical to optimise the time to unnecessarily small values. Doing so could damage components through thermal abuse as a result of high currents. Capacitor discharge can be achieved by connecting a parallel resistor, and an LED in combination with a reverse conducting zener diode could even be added to indicate when the capacitor is safe to touch. Two practical solutions exist for the implementation of this system; with or without a switch. A normally closed switch could be connected in series with the dump resistor. This ensures that the default state is to discharge the capacitor, which prevents the inability to safely discharge when the system that controls the switch fails. Alternatively, the dump resistor could be used without a switch, provided that the resistor has a relatively high value, as this setup makes it such that the capacitor is always discharging. This means that a part of the current that is provided by the source during the charging process will also flow through the dump resistor in this circuit topology. If the dump resistor has a relatively low value, it removes some flexibility, as the capacitor will have to be discharged in relatively quick succession as the voltage will start dropping immediately if the charging process is stopped. Not using a switch does give the benefit of reduced complexity, and it is a safer system ultimately, as there is also one less component that can fail.

5.3.4 Pulse switch

In literature and most TMS applications, there are realistically only two options that are used for pulse switching, namely IGBTs and thyristors[23]. The choice is relatively limited due to the strict requirements for the switches, as they must be able to withstand high voltages and high peak currents. As these requirements are pushed to higher and higher values, the differences between these two options become clearer, as opposed to the charge switch where it is of less importance what type of switch is used. A comparison table can be formulated to describe and compare the deciding factors:

	Weight	IGBT	Thyristor
Cost	1	€15,- up to €30,-	€10,-
Rise time	3		
1	+/-	+	
Ease of control	2	+	+/-
Reverse conduction	1	Undefined behaviour	Opens the switch

Table 5.1: Comparison between IGBT and thyristor as pulse switches

Among these factors, the rise time is the most important factor, since it is not desirable to have a rise time in the same order of magnitude as the pulse period itself. Additionally, a slow turn-on time could significantly lower the peak-current, which is also undesirable. The cost is not that important as a consideration, as only a single pulse switch is required per control circuit, and with a budget limitation of €750,-, as is stated by mandatory requirement C-MR11, the price difference is not that significant. With thyristors being mainly used for high current and high voltage applications, their range of different products to choose from is much wider when compared to IGBTs. There is still, however, plenty of choice among high power IGBTs, so this is not a significant limitation. Thyristors and IGBTs also differ in their mode of control, with thyristors being current controlled devices, and IGBTs being voltage controlled. The standard method for triggering a thyristor is to create a short current pulse. IGBTs can be put into forward conduction more easily as they only require a positive voltage to be applied over the gate and emitter. Finally, IGBTs do have undefined behaviour in reverse conduction, and as such they are not suited for this purpose. Thyristors will turn off by themselves once the current through the forward conducting path falls below a certain threshold, which also means that thyristors will block current from flowing in the opposite direction. Both devices can be integrated in a biphasic setup by adding an anti-parallel diode.

5.3.5 Switch control

There are several options when deciding on the method of controlling the switches in the control circuit. From the requirements it follows that the system must contain at least two coils, so it is desired to have precise control over the parameters of stimulation of the different coils (e.g. the voltages over the two charge capacitors and the duration between the firing of the pulses). The different methods considered in this project are: Manually charging and unloading the capacitor, and using a microcontroller to automate parts of the process. The considerations were further narrowed down to the following set:

1. Price, relating back to Requirement C-MR10.
2. Temporal resolution, relating back to Requirements C-MR1 and C-MR5, as these depend on the temporal resolution of the controller.
3. Implementation, relating back to Requirement TR1, to ensure that using the product is easy, informative, and robust, and that implementing changes to the design requires little programming knowledge.

4. Scalability, relating back to Requirement C-MR1, but only becomes a factor when more than two coils are used in the system.

5. Safety, relating back to Requirements C-MR4 and C-MR2.

The boards used for this comparison are the Arduino UNO r3, ESP32, STM32H747 (hereafter STM32).

	Weight	Manual	Arduino	ESP32	STM32
Price	1	-	24,-	11.99	23,64
Resolution (clk)	3	-	16MHz	160MHz	480MHz
Implementation	2	-	Serial data	WIFI-module	Serial data
Scalability	1	-	14 pins	34	+
Safety	2	Manual	Remote	Remote	Remote

Table 5.2: Comparison of the different control methods.

From the requirements and Table 5.2 the conclusion can be made that using a microcontroller is better when controlling a multi-coil setup. Manual control is slower and more sensitive to error, while the microcontrollers can have pre-loaded programs that will have higher precision in switch timings. Properly using the switching times of the controllers could have benefits when using multiple coils, such as high temporal definition between the firing and the necessity for only one power supply for multiple voltage levels. This last factor reduces the amount of required equipment, which in turn reduces the dependencies on many devices, and lowers the setup time.

The debate between the Arduino, ESP32 and STM32 was settled with the following decisions: while the industry standard for medical devices is currently the STM32 for its high accuracy, the ESP32 has many benefits when considering prototyping a design, and being able to be adapted more easily by researchers. The ESP32 has good specs: integrated WIFI module, high clock frequency, low cost, programmable in C using VS Code extension. The integrated WIFI module was decisive in choosing the ESP32, as this removes the need for serial communication. Serial communication requires different implementations based on the operating system of the user, is more sensitive to noise, the communication is slow, and making changes to the design is more difficult. Making sure that recorded data transfer travels differently from the system information messages means easier and separated debugging when changes are made to the design.

Additionally, the event based architecture of the ESP gives the opportunity for a responsive, scalable and configurable set of programs that can be run, and the changes made by the user are implemented much more easily. Since the programs would be implemented with HTTP handlers, there would be no need for adapting the data registers on the receiving computer to the new data, and only one program has to undergo changes. Furthermore, making these changes to the ESP program can be done with a VS Code plugin, and its documentation for simple implementation is better. Developing for STM32 on the other hand requires experience with embedded programming software, and is therefore less suited for prototyping and researching.

To conclude, it was found that the switches on the circuit should be controlled with a microcontroller to ensure accurate and consistent results. While the STM32 has better specs for final implementation, the ESP32 advocates itself for prototyping and researching, and will therefore be chosen for this project.

5.4 Design Analysis

This section will cover an analysis of the previously proposed designs. The metrics that will be considered are mainly based on the Programme of Requirements.

5.4.1 Interpulse duration

RLC circuit

For a series RLC circuit, the factors that decide whether or not the interpulse duration is shorter than the current pulse duration are the maximum error margin of the switch control system, and the pulse period itself. Defining the pulse period is an important choice to make here, since different approaches can be taken here. The most accurate solution would be to find the time at which the current has become equal to zero after a full oscillation. This, however, only works for biphasic pulses, as monophasic pulses have a horizontal asymptote at $I = 0\,\mathrm{A}$ in their current waveform, so there is no analytic solution. This also becomes apparent when Equations 5.2 and 5.3 are analysed. The current in a biphasic circuit can only become equal to zero when the sine factor is equal to zero, so the period of a biphasic waveform can be found by setting the terms inside of the sine function equal to zero and evaluating at $n = 2\pi$:

$$T = \frac{2\pi}{\sqrt{|\alpha^2 - \omega_0^2|}} \tag{5.15}$$

The same cannot be done for the monophasic equation, as the hyperbolic sine is only equal to zero at $t = 0\,\mathrm{s}$. Here, a numerical approximation is required, one similar to the way in which five time constants are used as a sub one percent threshold for capacitor charging, to accurately indicate the period of the waveform. Alternatively, the resonant period could be used as a worst-case scenario. For waveforms that are just barely monophasic, and almost critically damped, the resonant period is almost equal to the time at which the current passes its sub one percent threshold. This statement will not be proven here, but it can be verified relatively easily by evaluating the current characteristics equation for RLC networks at the time at which the current is at its maximum, and the resonant period. As a waveform becomes increasingly more monophasic, the resonant period will become a worse and worse indicator for the pulse period, but it can still be used as a worst case.
When choosing RLC values for the circuit, this means that the error margin of the switch control must be less than either the resonant period or the value that results from 5.15, if the circuit is to be in compliance with mandatory requirement C-MR1.

Microcontroller accuracy

The second part of having the ability to fire pulses within a time frame that is shorter than the pulse period is to design an adequate timer system. The ESP32 has a clock frequency of 160MHz with a pre-scaler of 16 bit, to be used in the software timer. The ESP32 also has hardware timers that are able to deliver a temporal accuracy of a millisecond. It also has two timer protocols, general purpose and high resolution. Both can be set to the same temporal resolution, but the general purpose timer can only have one alarm set, at which multiple handlers will be activated. So in order to make a set of temporally spaced actions, the high precision timer must be used. There are also two ways a callback can be called: when the timer value is configured as a task, the callback will be considered as a task and there could be a delay between the timer interrupt and the carrying out of the callback (Information sourced from the Espressif [26]). To compensate, one can configure a timer in the Interrupt Service Routine (ISR), so the callback becomes of higher priority. In an ISR callback however, no blocking APIs can be called, such as reading out data from an ADC. So a combination between task and ISR dispatched methods should be used.

The decision was made open the charging gates with tasks, as the voltage could be measured in the same callback. The charge switch closing and the pulse switch opening will be done through ISR for improved accuracy. To test the accuracy of the timers, eight timers with ISR dispatching were setup and the timings of the callbacks recorded using the *esp_timer_get_time* function. Each measurement was made with 8 timers 200 µs apart, each with a different starting time. These measurements are presented Table 5.3.

	Measurement 1	Measurement 2	Measurement 3
Timer 1	55011	56011	60008
Timer 2	55212	56212	60216
Timer 3	55407	56407	60404
Timer 4	55608	56608	60608
Timer 5	55811	56812	60812
Timer 6	56004	57004	61004
Timer 7	56208	57208	61208
Timer 8	56408	57408	61407

Table 5.3: Timings test for the ESP32 microcontroller.

The variance in the results stem from the fact that it does not take the same time for all timers to be created. After the timer is created, the zero time moment is after the line of code is executed, and since there is some variance in how long it takes to create the timer, not all timers can be aligned perfectly. When looking at the different timers, there is also a recognisable pattern in the creation of the timers, which could be compensated for, but this would not yield a stable solution. Additionally, it was found that the ESP shows non-linear behaviour when setting values between 0 and 25 microseconds: The spacing between the two callbacks would be 5 or 20 microseconds depending on the given interpulse duration, after 25 µs the behaviour was again as expected. In Figure 5.6 the measurement can be seen that was made with an entered voltage of 7 µs, but the time between the callback resorted to a standard value within this range, here 5 µs.

This concludes that for accurate control with the ESP32 the pulse period must be more than 25 microseconds, with a maximum difference between two consecutive timers of 12 µs, and an average of 4.0 µs, following from Table 5.3. Below this value, the behaviour is non-linear, so less flexible, but also more robust. The ESP32 adheres to Requirements **??** and C-MR1, and seeing the added benefits of using the ESP32, it was decided to use this microcontroller for integration.

5.4.2 Capacitor energy

To be in compliance with mandatory requirement C-MR2 the evaluation of a single equation is required.

$$E = \frac{1}{2}CV^2 \tag{5.16}$$

By substituting a value of 10 J for E, all possible combinations can be found for the maximum values of the capacitance and the voltage to which the capacitor is charged.

5.4.3 Capacitor charging

As is expressed through mandatory requirements C-MR6 and C-MR7 it is desirable to be able to charge the capacitors to a certain voltage with a maximum error margin of 5% of the maximum voltage within 10 s. This means that there is a upper bound for the rate at which the voltage changes over time, which is limited by the temporal resolution of the switch control system, and

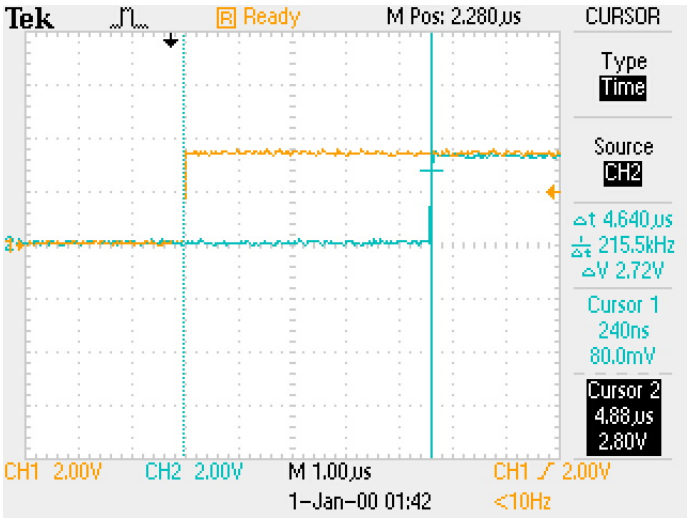

Figure 5.6: Measurement of the interpulse duration of the ESP32 microcontroller. The two channels are different GPIO outputs set to high in different ISR timer callbacks. The ESP shows non-linear behaviour in the 0-25 microsecond range, and values in this range resorts to a limited number of possible interpulse durations. The requested interpulse duration for this test was 7 µs.

there is a limit to the charge time of the capacitor, which is limited by mandatory requirement C-MR7. In the previous section, it was discussed that the discharging system could use a resistor that is connected parallel to the capacitor, which could either be directly connected, or connected via a normally closed switch. In the latter case, the time constant can be expressed as follows:

$$\tau = RC \tag{5.17}$$

This assumes that charging is done with the discharge switch in its open state, which should prevent any unnecessary energy loss. To be in compliance with the 10 s charge time requirement, Equation 5.17 simply has to evaluated with five time constants being equated to 10 seconds. The evaluation changes slightly for an RC circuit that has both a series and a parallel resistor, as is the case for the topology where the dump resistor is connected without an additional switch.

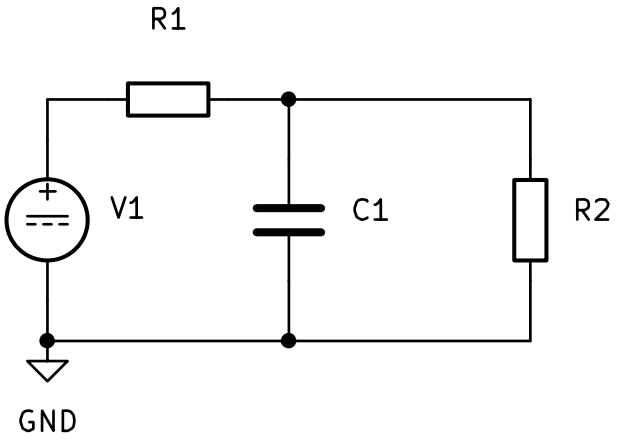

Figure 5.7: Series parallel RC network representation of combined charge and discharge system without switches

Figure 5.7 shows the alternative topology. Applying circuit analysis to the network results in the following expression:

$$\tau = \frac{R_1 R_2}{R_1 + R_2} C \tag{5.18}$$

The same can be done as before by evaluating the newly acquired expression with five time constants being equal to 10 seconds.

Finding out whether or not the system is in compliance with the 5% error margin requires two pieces of information, namely the error margin of the switch control system and the maximum voltage change over time. The latter can be found by taking the derivative of the voltage of a charging capacitor and evaluating that expression at $t = 0\,\text{s}$, as the change over time is the greatest at that moment. The voltage of the series and series parallel RC networks as the capacitors charge, can be expressed with Equations 5.19 and 5.20.

$$V(t) = V_s \left(1 - e^{-\frac{t}{RC}}\right) \tag{5.19}$$

$$V(t) = \frac{V_s}{\frac{R_1}{R_2} + 1} \left(1 - e^{-\frac{\left(\frac{R_1}{R_2}+1\right)t}{R_1 C}}\right) \tag{5.20}$$

Then, by taking the derivative, and evaluating at $t = 0\,\text{s}$, the following expressions can be found:

$$\frac{dV(0)}{dt} = -\frac{V_s}{RC} \tag{5.21}$$

$$\frac{dV(0)}{dt} = -\frac{V_s}{R_1 C} \tag{5.22}$$

Equations 5.21 and 5.22 show that both circuit topologies actually have the same maximum change over time at $t = 0\,\text{s}$. The acquired expression can then be used to formulate Equation 5.23, which in its place can be used to verify whether or not the system is in compliance with the voltage error margin requirement.

$$\frac{V_s}{R_1 C} \cdot t_{\text{error}} < 0.05 \cdot V_{\max} \tag{5.23}$$

Additionally, the error of the microcontroller needs to be taken into account. To control the charging switch, two different type of interrupts are used on the ESP, the task interrupt is used to measure the voltage over the capacitor, to inform the user about the actual voltage that was actually over the capacitor during the test. ISR callbacks are used for the charge and pulse switches, to ensure the accuracy of the system. In Section 5.4.1 this maximum error was established to 12 µs. These value combined with the charging time determines the error margin.

5.4.4 Capacitor discharging

Discharging the capacitor, just like charging the capacitor, must be able to be done in under 10 seconds, as is stated by mandatory requirement C-MR7. Here, verifying the system's compliance with this requirement is as straightforward as evaluating Equation 5.17 with five time constants being equated to 10 seconds.

5.4.5 Peak current

Mandatory requirement C-MR9 states that the control circuitry must be able to send a current pulse with a dI/dt of at least 100 MA/s through a wire loop with a loop diameter of 1 cm and a wire diameter of 0.4 mm.

$$L = \mu_0 \mu_r r_{\text{loop}} \left[\ln \left(\frac{8 r_{\text{loop}}}{r_{\text{wire}}} \right) - 2 \right] \tag{5.24}$$

$$R = \frac{\rho l}{A} \tag{5.25}$$

Equations 5.24[27] and 5.24 show that such a wire loop will have an inductance of 15 nH and a resistance of 4 mΩ.

- $R = 100\,\text{m}\Omega$
- $L = 150\,\text{nH}$
- $C = 100\,\mu\text{F}$
- $V_s = 150\,\text{V}$

To verify the feasibility of the system's compliance with the relevant mandatory requirement, some values have been selected that should be be relatively reasonable for a real-world implementation. For the resistance and self-inductance, the values have been chosen with parasitic resistances and parasitic self-inductances in mind from the RLC components, the switches and the conducting paths between the components. The capacitor value has been verified to be in a range where there is a wide range of options to choose from with voltage ratings above 100 V and peak current ratings above 1 kA taken into account. Taking these component values, and finding the derivatives of Equations 5.2 or 5.3 at $t = 0$, the following reduction can be found:

$$\frac{dI(0)}{dt} = \frac{V_s}{L_{\text{total}}} \tag{5.26}$$

By taking the previously proposed placeholder component values, it can be found that such a circuit should produce a maximum dI/dt of 1 GA/s, which is 10 times higher than the requirement. This shows that there is quite a lot of room to change the component values while being in compliance with the requirement.

5.4.6 Heat

To prevent the conducting paths from exceeding a temperature of 318 K, as is stated by mandatory requirement C-MR10, it is of major importance that the ratio between the total series resistance in the pulse loop and the total copper mass of the conducting paths is thoughtfully considered. Since there is a mandatory requirement that limits the input energy at 10 J, the specific heat equation can be used to find the minimum copper mass that is required to safely dissipate the energy.

- $\text{C}_{\text{Cu}} = 0.385\,\text{J/g°C}$
- $\text{Q} = 10\,\text{J}$
- $\Delta\text{T} = 25\,\text{°C}$

$$C = \frac{Q}{m\Delta T} \tag{5.27}$$

By solving Equation 5.27 for the mass m, it can be found that the minimum copper mass required to prevent an input energy of 10 J from heating the conductive path more than 25 °C, which is the difference between room temperature and the previously mentioned temperature limit, lies just above a single gram at approximately 1.04 g. This means that for a square wire with a width and height of 1 mm, a minimum length of 12 cm is required to safely dissipate the capacitor energy of a single pulse.

5.5 Design Choice

Following the design analysis, a few conclusions can be made about the RLC circuit that lead to the topology choice of the final implementation. Since the goal is to achieve at least 100 MA/s, and ideally this value is maximised to the extent that is allowed by the limited energy with which the capacitor is charged. This means that it is favourable to optimise the RLC circuit in the following ways:

- Minimise the total series resistance of the pulse loop to prevent the circuit from excessively heating up, and to maximise the dI/dt.
- Choose the voltage and the capacitance in such a way that the energy is as close as possible to the limit of 10 J.
- Maximise the voltage to increase the current and to allow the capacitor to be minimised, as this decreases the period of the pulse, which is also beneficial for the dI/dt. Do not choose the voltage at such a high value that it becomes unnecessarily difficult to find properly rated components.
- Use IGBTs for the pulse and charge switches. At least for the pulse switch it is ideal to have a switch with a short rise time to prevent the switch from reducing the peak current value. For the sake of consistency and simplicity, it is preferable to also make the charge switch an IGBT. This IGBT does not have to have the same high current ratings, as long as it has proper voltage ratings.

Additionally, the choice will be made to directly connect the dump resistor to the capacitor, as there is no real incentive, aside from a additional level of control, to be able to discharge the capacitor at will. Not implementing the switch also means that the circuit becomes less complex, and by extension also safer.

Regarding the controlling of the switches, it was chosen to use an ESP32 microcontroller for this project. The results from the analysis show that the ESP32 is able to fulfil requirements **??** and C-MR1. The integrated WIFI module has great benefits for research and development, which will be the primary goal of the product. In future renditions, STM32 microcontroller should be considered to increase the accuracy of the design.

5.6 Implementation

The control circuit contains a lot of elements that should be assembled in an optimal manner. The entire schematic of the system can be found is figure **??**. This schematic is further separated into three sections: The control circuit, the microcontroller board, and the power circuit. The separation for the PCBs was chosen to reduce the footprint of the module, which makes it more easily movable across the testing space. The microcontroller board contains the microcontroller and the gate drivers.

5.6.1 Pulse loop

For the pulse loop, only the capacitor and the switch have to be chosen, as the inductor is designed and produced by the Stimulation subgroup. In the design analysis, a comparison between IGBTs and thyristors was made, and from that comparison, it has been concluded that IGBTs are the preferred option for this specific application. The most important properties and characteristics of the components for the pulse loop have been described in the following list:

- Capacitor
  - High DC voltage rating, >300 V
  - High peak current rating, >1000 A
  - Low equivalent series resistance (ESR), <30 mΩ
  - Low equivalent series inductance (ESL), <30 nH
- IGBT
  - High DC voltage rating, >300 V
  - High pulse current rating, >1000 A for 1 ms
  - Low resistance, <30 mΩ
  - Low self-inductance, <30 nH
  - Low rise and fall time, <500 ns

The optimisation of these parameters has been done with the sole purpose of maximising the dI/dt.

	Capacitor	IGBT
Voltage	500 V	650 V
Peak current	3150 A	-
Pulse current (1 ms)	-	1200A
Resistance	1.6 mΩ	17 mΩ
Self-inductance	19 nH	-
Rise time	N.A.	93 ns
Fall time	N.A.	40 ns

Table 5.4: Component values of the pulse capacitor and pulse IGBT

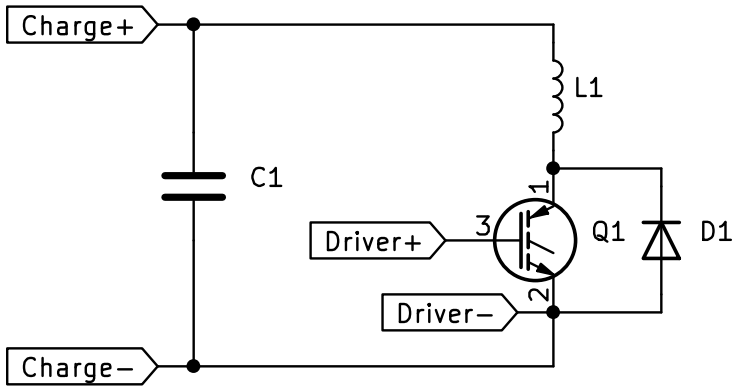

Figure 5.8: Schematic of the pulse loop

Table 5.4 shows the relevant parameters, and Figure 5.8 shows the topology of the pulse loop. In the process of selecting the capacitor, the highest priority was given to selecting one with a

high peak current. This brings the difficulty of capacitors with higher current ratings becoming quite bulky, as they should be able to dissipate the additional energy. There is a preference, however, for lower capacitances, as this will increase the dI/dt by decreasing the pulse period. Just a few options remained with this list of preferences, and a final value of 210 µF was chosen in combination with a supply voltage of approximately 300 V. This combination should result in the capacitor storing a maximum of just under 10 J. Care should still be taken as the capacitor has a tolerance of 10%, which means that at its maximum value the maximum voltage is 294 V instead. Fortunately, the ESR and ESL of the capacitor were really low compared to other capacitors with similar voltage and current ratings. The IGBT was selected by finding ones with the highest pulse current ratings. Most IGBTs in this rating range had sufficiently low rise and fall times, and resistances. The inductance for this specific IGBT is not mentioned in the datasheet, but most IGBTs of the same form factor typically have a self-inductance of about 5 nH up to 20 nH. Since the majority of the parasitic self-inductance comes from the leads of the IGBTs, it is assumed that it is reasonable to estimate the self-inductance at approximately 20 nH. In the final implementation, the length of the leads will be minimised to further optimise the dI/dt. Finally, an anti-parallel diode has been added to the IGBT to protect it from reverse conduction, as IGBTs do not have defined behaviour in reverse conduction. Using these components in combination with the placeholder stimulation inductor, which is a wire loop with a self-inductance of 15 nH and a resistance of 4 mΩ, the following characteristics can be simulated:

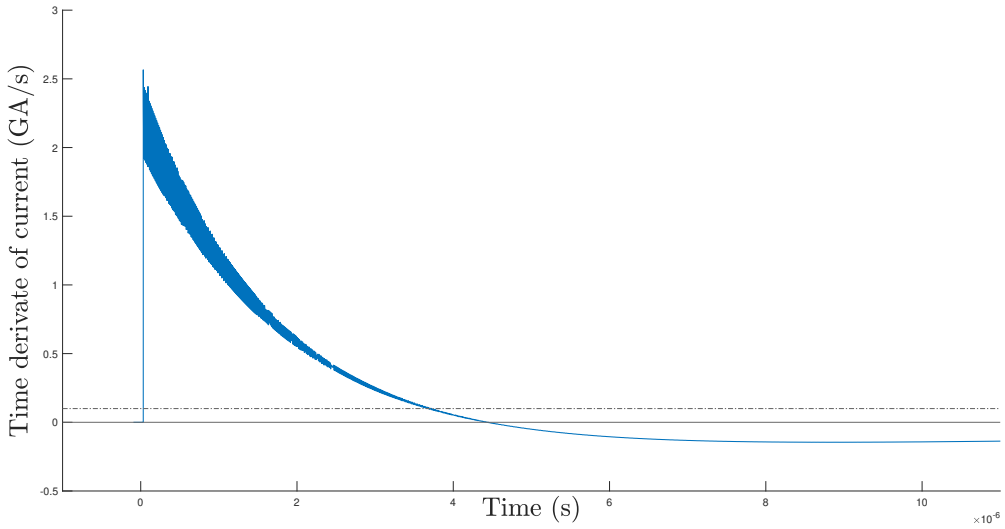

Figure 5.9: dI/dt of the pulse loop that was shown in Figure 5.8. The following RLC series values were used: $V_0 = 300\,\text{V}$, $R = 78.6\,\text{m}\Omega$, $C = 210\,\mu\text{F}$, $L = 134\,\text{nH}$ ($\xi = 1.56$). Parasitic properties of the capacitor, the IGBT and the wire have been included in these values, as well as an approximated resistance of soldering connections, but the parasitic capacitances of the inductor, wire and IGBT have been ignored. The data shows that the threshold of 100 MA/s, which has been indicated with a dotted line, is amply achieved. The waveform oscillates a lot due to the parasitic inductance of the capacitor.

This combination of parameters has the added benefit of being able to create a monophasic pulse, which is beneficial for attempting to stimulate the neurons in a worm.

5.6.2 Charge and discharge loops

Since the capacitor has already been chosen for the pulse loop, only the resistors have to be carefully considered. As was discussed in the design analysis, the addition of an extra switch that controls the discharge loop brings little to no benefit at all when the added complexity is taken into account. The charge switch does not have to be an IGBT per se, but since the pulse switch is an IGBT is it desirable to use an IGBT for the charge switching as well, since this is beneficial for the consistency and simplicity of the implementation. There is no need for the charging process to occur in a time-frame of tens or hundreds of microseconds, so the peak current requirements are not nearly as strict. The specific choice of switch does not have a significant effect on the charging behaviour, apart from its switching time, but since IGBTs typically have a rise and fall time in the order of magnitude of tens or hundreds of nanoseconds, the effect on the accuracy of the voltage setting is practically negligible. For the exact same reason of protecting the IGBT against reverse conduction, an anti-parallel diode is added, just like in the case of the pulse IGBT. These components should have a voltage rating of at least 300 V.

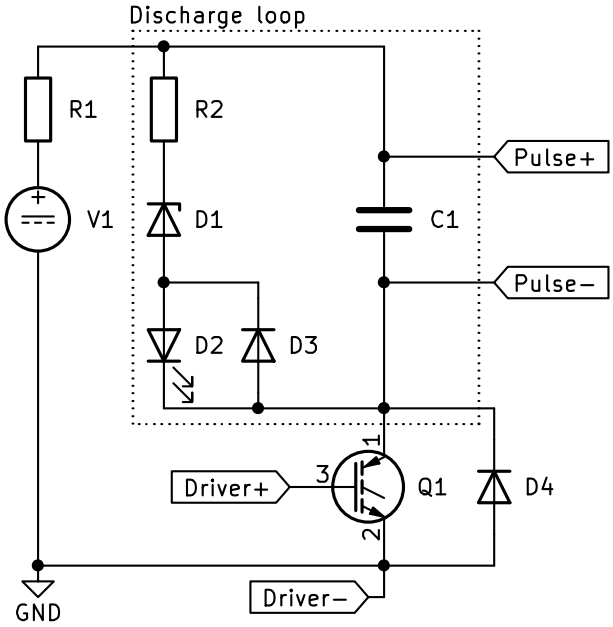

Figure 5.10: Schematic of the charge and discharge loops

Component	Parameter	Value	Unit
V_1	Voltage	300	V
V_1	Current limit	100	mA
R_1	Resistance	50	Ω
R_2	Resistance	3000	Ω
C_1	Capacitance	210	µF
D_1	Zener voltage	10	V
D_2	Current limit	100	mA
D_3	Current limit	100	mA

Table 5.5: Component values of charge and discharge loops

Figure 5.10 shows the topology of the proposed charge and discharge loops. The discharge loop contains some additional components aside from the dump load, namely a reverse conducting Zener diode and an LED with an anti-parallel diode, that protects the LED from reverse

breakdown. The LED is used to indicate that the capacitor is charged, and by adding a reverse conducting Zener with a Zener voltage under the practical safe voltage limit of 60 V, the LED will also indicate when it is safe to touch or move the capacitor again by not emitting any light when the capacitor has dropped below the Zener voltage. The breakdown current of the LED, which will in most cases be the limiting factor for the discharge loop, should be chosen as high as possible, which will typically be around 100 mA. This value can then be used to find the minimum value of the dump load, which, for a voltage of 300 V should be at least 3 kΩ. Looking at the charging loop, which really only consists of components V_1, R_1, R_2 and C_1, it can be observed that in the absence of a switch in series with the dump load a voltage division is created with a ratio that is dependent on the values of the two resistors. Henceforth, these resistors, R_1 and R_2, will be respectively addressed as the charging resistor and the dump load. Since there is a voltage division, and the resistance of the dump load has already been chosen, it is preferable to minimise the value of the charge resistor, as this will lower the charging time, and maximise the maximum voltage of the capacitor in its fully charged state. Using a 50 Ω charge resistor yields a maximum capacitor voltage of 295 V with a voltage source at 300 V. Evaluating Equation 5.18 with these values results in five time constants being equal to 52 µs, which results in a voltage of 293.1 V. This does assume that the voltage source is not current limited. Ideally, a voltage source without current limit is used to promote fast charging speeds, but for the sake of safety a current limited voltage source has been selected for this project, with the limit being 100 mA. For current limited RC networks, the voltage and current characteristics become piecewise functions. Substituting the voltage source for a current source, removing the charge resistor and substituting the dump load and the current source for a Norton equivalent voltage source allows for the first part of the piecewise function to be found. The second part is simply Equation 5.20, but this part can practically be ignored since it starts beyond the five time constants voltage at 295 V, which is where the current of the unlimited case would reach 100 mA. The first part of the piecewise function is as follows:

$$V_C = \frac{I_{\text{lim}}}{R_2}\left(1 - e^{-\frac{t}{R_2 C}}\right) \tag{5.28}$$

By evaluating Equation 5.28 at 150 V, it can be found that a charging time of 437 ms is required, which appears to be true according to Figure 5.11, which shows the simulated characteristics.

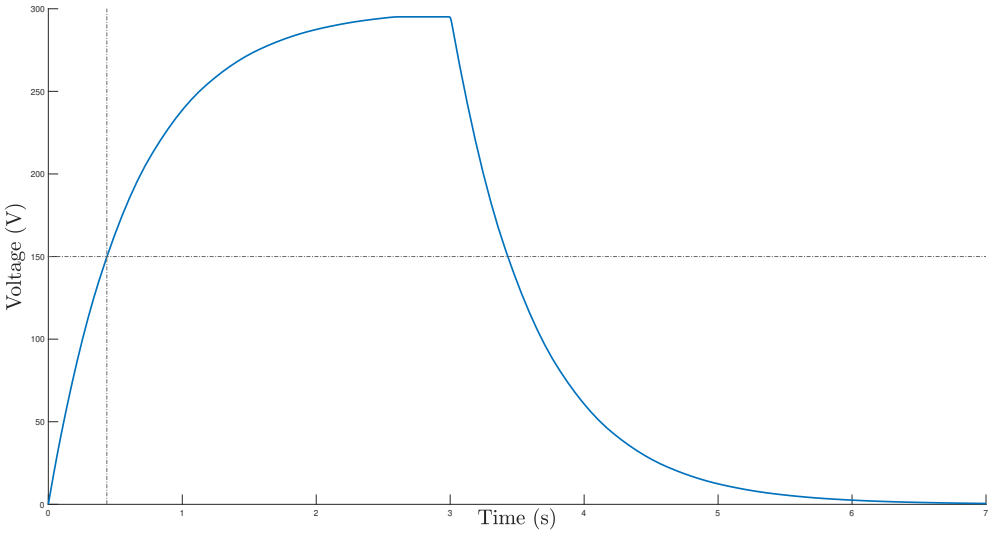

Figure 5.11: Voltage of the pulse capacitor plotted against time. Using the circuit topology of Figure 5.10 with a 50 Ω charge resistor, a 3 kΩ dump load, a 300 V voltage source limited at 100 mA and a 210 µF pulse capacitor, it is expected that after 437 ms the voltage should be 150 V, which can be confirmed to be true, as is shown by the dotted lines. Additionally, it was expected that the maximum voltage should be 295 V, the charge time should be 2.58 s and the discharge time should be 3.15 s. This can be roughly verified visually.

Figure 5.11 also confirms that the maximum voltage of the capacitor lies around 295 V and that the discharge time for five time constants is approximately 3.15 s, which matches with the evaluation of Equation 5.17 with the relevant component values.

Regarding the accuracy of charging the capacitor to a specific voltage, using Equation 5.23, it can be found that the maximum error amounts to 0.12% of the maximum voltage when the maximum timing error is 12 µs. The tolerances of the resistors and capacitor should be measured and their values should be adapted accordingly in the equations to prevent any additional inaccuracies.

5.6.3 PCB

Since multiple stimulation modules must be used in accordance with requirement C-MR1, and the control over these modules must be maximised, it would be desirable to have the modules behave with as little variability as possible. Therefore, it was chosen to design a PCB to host the circuitry. The following requirements were put forward:

- The PCB must be modular, with each module containing one stimulation inductor, so that these can be moved freely during testing. (Requirement G-TR2)
- The PCB must be as small as possible. (Requirement G-TR2)
- The traces of the PCB must be able to handle the high power demands of the circuit. (Requirements C-MR8, C-MR9)
- The stimulation inductor should be easily installed on the edge of the PCB.
- The PCB must allow for multiple inductors to be tested.

Firstly, the layout was chosen for the PCB. The pulse capacitor, IGBT and the slots for the inductor were composed as closely as possible, but with the condition of keeping all components to one side. For the inductor slot, a mask was made at the end of the traces so that multiple inductors could easily be soldered directly onto the traces. The traces end on the side of the PCB to easy positioning during stimulation. Additionally, two test point were added over the capacitor. After connecting the components via the shortest path possible, the total length of the wire ended up at approximately 8 cm.

Previously, in the design analysis, it was shown that a minimal total mass of 1.04 g was necessary to prevent the conducting paths from heating up beyond a temperature of 318K. As a practical compromise, the traces were designed to be 70 µm thick, which equates to two ounces of copper, and 9 mm wide. This yields a total copper mass of just under half the proposed minimal total mass, but this does not take into account the conductive mass of other large circuit components such as the switch and the capacitor. It is expected that the RLC loop in its entirety should have enough conductive mass to not heat up beyond the temperature limit.

These values were further investigated with Saturn PCB Design. With the expected maximal frequency component of 100 kHz, the wire diameter lies between a single skin depth and 10 skin depths, which means that excessive resistance increase due to surface roughness is avoided and all copper experiences at least a single percent of the total current density. With a wire length of 8 cm the DC resistance is found to be around 2.8 mΩ.

Ideally, the traces should be optimised for the maximum practical copper weight, as this reduces both the resistance and the self-inductance, which is beneficial for maximising the dI/dt. Additionally, optimising the conductive path to be as short as possible minimises the self-inductance of the paths, which is also beneficial for increasing the dI/dt.

Afterwards, the charging and control circuits were added. The first tests will be performed with slow charging time, and with a monophasic pulse, but when changing these parameters in such a way that the pulse becomes biphasic, the switches will require RC snubbers to protect the switches from sudden voltage spikes in the event of closing the switch after a full period when there is still a significant dI/dt. Space has been reserved on the PCB for the snubbers, but no components have been selected for the scope of this project.

The schematic and the PCB layout can be found in Figures 5.12 and 5.13.

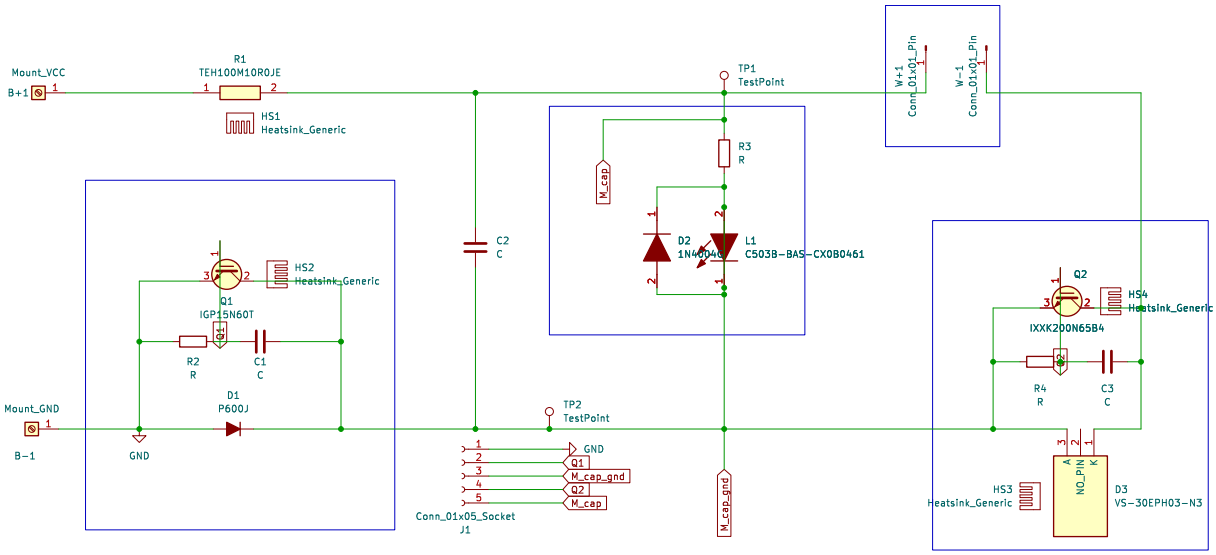

Figure 5.12: Complete control PCB schematic. Including charging, discharging, pulse, and control electronics. All sections have been elaborated upon further in Section 5.6.

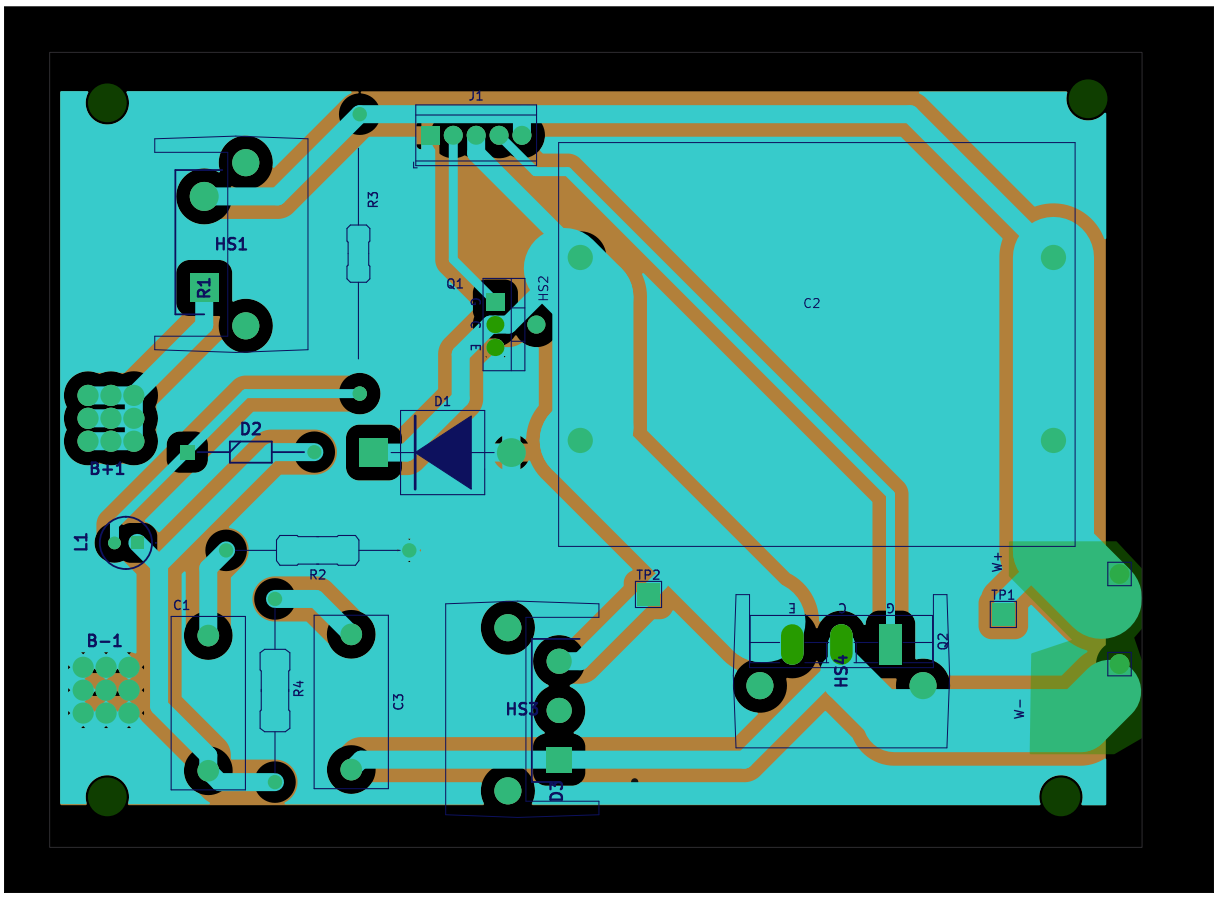

Figure 5.13: Control module PCB layout

Finally, the realisation of the control circuit on a PCB as form factor allows the entire setup to be moved

5.6.4 Microcontroller

For the microcontroller the ESP32 will be used. Two main library's have been developed for the controller, one for Arduino IDE and one for programming in C. The latter has been chosen as it provides more control, and is better documented. The library functions as an API to the freeRTOS kernel, so a lot of the limitations and configurations are based on the workings of freeRTOS. The microcontroller in question has a 160MHz clock frequency and about 520kB of RAM.

The program that runs after the ESP receives power is visualised in Figure 5.14, and works as follows: After the board receives power, OS will boot and main app will start. Here, the WIFI module will be enabled in softAP mode, and all HTTP handlers will be registered. Further setup consists of the GPIO and ADC, only ADC1 will be used in attenuation mode 12, as ADC2 is used for WIFI. After that, the program will wait for a request from the user. The user logs onto the WIFI network hosted on the ESP32 and can operate the ESP32 from a browser or a python script. The script also allows the user to view the data instantaneously after the ESP responds with the measured data.

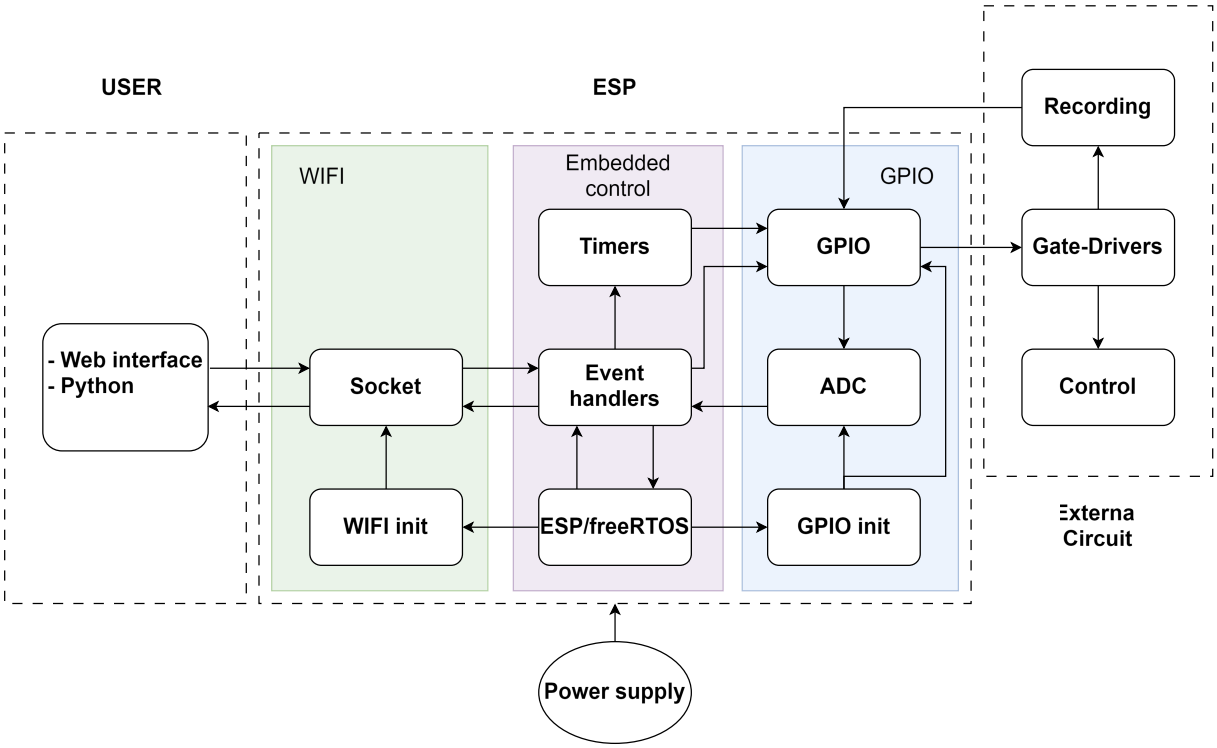

Figure 5.14: Schematic for the ESP32

The server has a set of registered GET requests that can be called by the user: Setting the parameters, triggering the stimulation, and requesting the data. In the provided python script there has also been given the option to run all of these with a single request: *program_1* and *read_data*. The latter allows the user to make a long reading. The data will be recorded and sent out in separate HTTP chunks. The python script glues these chunks together to form the complete data string. This function can be used for testing the setup.

Program_1 will be used for stimulation using two inductors and consists of multiple sections. First, the timers will be created, and depending on the input parameters from the user. The values that can be changed in this program are: Voltages of two separate inductors, and the interpulse duration of the firing of the two pulses. Before the first pulse is generated, a measure-

ment of 16ms is made to comparison after the pulse. The pulse switch close in the same callback as the charging gate opens, since the charge gate has a faster switching time. This callback is called for the separate charging times of the pulse capacitors (Section 5.4.3). After the second pulse fires, the blanking switch will close after 100us, to reduce interference. 3 blocks of 16ms of data will be measured and will be send via HTTP chunks to the user. The timeline can be found in Figure 5.15

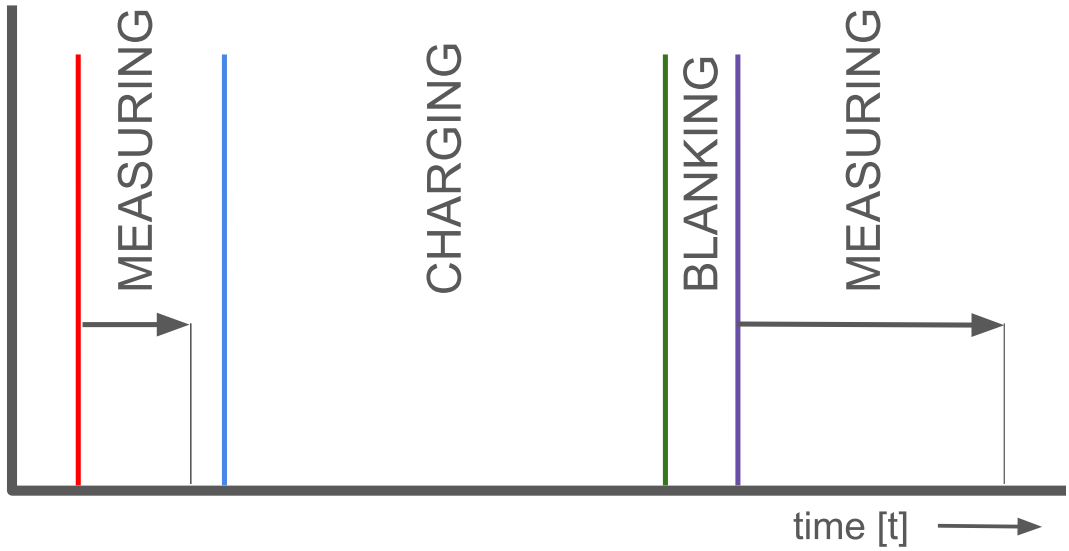

Figure 5.15: Timeline of program one for single inductor. (red) The timers are created and a measurement is made. (blue) The charge gate closes and the capacitor is charged. (green) Pulse gate closes. (purple) After blanking period the a longer measurement is made.

Detailed instructions on how to use the system, and make changes, can be found in Appendix B.

5.6.5 Gate Driver

To be able to control the IGBT switches using the ESP voltage output, a system of gate drivers needed to be designed. To allow the pulse IGBT its maximum current, the gate-emitter voltage needs to be at least 16V (Section **??**). The original design to accommodate this voltage was with the use of a high switching MOSFET, as the switch should not restrict the switching times of the IGBTs. When implementing the initial design in Figure **??**, it was found that the ESP should not be powered using the same source that provides the pulse power (300V source). This would cause the reference voltage of the ESP - and the gate voltage of the IGBT- always to be equal to the emitter voltage, so the switch could never open. Initially it was planned to solve this by powering the microcontroller with a battery, and the problem with the implementation was only found when incorporating the design with the recording subgroup.

When the ESP is also used to record the data, and the blanking pulse is also sent from the ESP to the recording circuit, they should have a shared ground to operate properly. When the recording group uses power supplies connected to the net, it would again link the reference voltage of the ESP to the gate to the emitter of the IGBT, thus making it so it will never turn on. To resolve this, the grounds needed to be separated. The easiest way to resolve this is

by using 2 separate DC ground plane sources, galvanically isolated by the implementation of a transformer. The second option is to use insulators within the design.

The option of using isolation within the circuit was used, as this would also remove a risk that arises with the first implementation: Due to the placement of the pulse IGBT, the ground of the ESP32 is lifted to 300V, which forms a hazard for the user and for the ESP. a new driver circuit was designed that would give separate the ESP output voltage from the gate of the driving MOSFET. Optocouplers were used for this purpose, as they can achieve high switching times, and need little current to turn on. Rise and fall time are important is this is the thirds switch added to the loop for enabling the IGBT. A simple pull-up network was designed for the 6N136 optocoupler. R_1 and R_2 make a voltage divider that will drive the FET, 5V is enough here. R_5 limits the current of the ESP32, but should not be too large, as this affects the operation of the interal LED. R_3 contributes to longer fall time of the FET, and should therefor be kept low, but not too low that the current becomes too large. With a value of 50, the current of 400 mA is not small, so the resistor must withstand some power. The chosen values are listed in Table 5.6.

Component:	Value:
R1	880 Ω
R2	220 Ω
R3	50 Ω
R4	20 kΩ
R5	100 Ω
OC1	6N136
Q1	IXXK200N65B4
Q2	SI2312DBS

Table 5.6: Gate driver circuit with optocoupler component values.

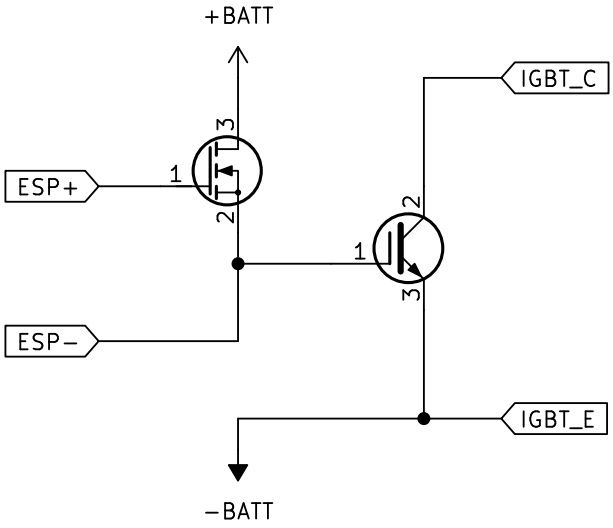

Figure 5.16: Gate driver circuit without the inclusion of an optocoupler for insulation. When non-insulated sources are used to power the recording circuitry and the pulse capacitor, the ground of the ESP becomes connected to the emitter of the IGBT. The switch would therefor never turn on. This setup also raises the ESP ground to 300V after the capacitor is discharged.

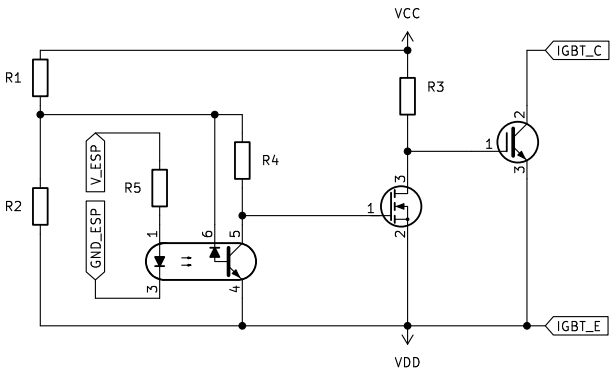

Figure 5.17: Gate driver circuit with the inclusion of an optocoupler for insulation.

When connecting this circuit to the one in Figure 5.10, the following dI/dt results from LTSpice.

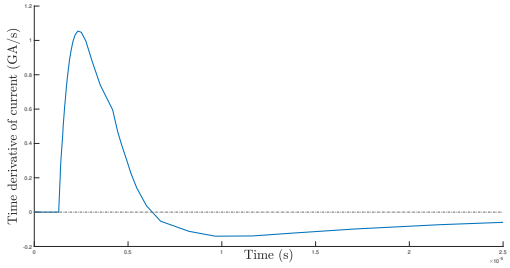

Figure 5.18: Gate driver circuit with the inclusion of a optocoupler for insulation.

5.6.6 Enclosure

The control PCB and its accessory peripherals can be put into a transparent flat plastic box with a lid. Holes with a diameter no larger than 10 mm can be cut into the sides of the box, which will allow cables to enter the box without enabling fingers to reach far enough inside to touch active circuitry. As the power supply itself is also IP2X rated, this setup should be in compliance with both enclosure and insulation requirements.

5.6.7 Minimum Viable Product

During implementation, due to time constraints, it was decided to reduce the product to the minimum functioning design, so that the product of this subgroup could still be used with the products of the other subgroups for the complete design implementation and tests. It was thereby decided that the charge IGBT would be shorted. This enables the pulse IGBT to control the entire circuit, reducing the complexity of the design. Requirements C-MR6 should still be achievable by setting the DC voltage of the source, at the cost that multiple coils can not be driven by different voltages. This change also implies that there will be a constant DC current trough the inductor when the switch is not open. This current will be limited by the charge resistor and the DC source. This DC current is negligible compared to the current pulse of the discharging capacitor.

5.6.8 Cost

For the final implementation, just over €613, − was spent on two control circuits, spare parts for a single PCB and the ESP32. This means that the cost of a single of a single control PCB

with its accessory peripherals amounts to approximately €212, −. The total amount that was spent, is less than the subgroup budget of €750, −.

5.7 Results

Due to time constraints, no physical testing was done with the designed PCB. All the conclusions about the efficacy of the system will be based on the simulation results, and can be found in Section 5.6.

5.8 Discussion

While most of the requirements are theoretically feasible with the designs that we have made for this project, a definitive answer about the real world functioning has to be omitted due to the lack of real life testing results. Due to time constraints, it was decided to focus on completing the report, and draw conclusions from the simulations.

The developed RLC circuit shows promising results, and marginally surpass the requirements about minimum dI/dt, safety and charging speed. The ESP microcontroller, even though it does adhere to the requirements, and shows enough quality to justify being used for this project, is not precise enough to be used for an actual product, and will need to be replaced with a more precise microcontroller in the future. This is primarily relevant for the interpulse duration.

With added time, the minimum viable product would be assembled and tested, after which the charge IGBT would be added back into the schematic for control over the different capacitor voltages. The gate drivers would be made using the 6N136 optocouplers to improve the switching time.

5.9 Conclusion

To come back to the primary objective, which was to design, build and test a control circuit that could be used to power a stimulation inductor. A Programme of Requirements was put together around this main objective that consisted mainly of requirements pertaining to the user safety and providing the proper current characteristics. Using the simulation results from the proposed implementation, the following can be stated about the system's compliance with the Programme of Requirements:

Requirement:	Achieved:	Value:
GC-MR1	–	–
C-MR1	Yes	N.A.
C-MR2	Yes	N.A.
C-MR3	Yes	N.A.
C-MR4	–	–
C-MR5	–	–
C-MR6	Yes	0.12%
C-MR7	Yes	2.6 s
C-MR8	Yes	3.15 s
C-MR9	Yes	2.5 GA/s
C-MR10	–	–
C-MR11	Yes	613, –
TR1	Yes	N.A.

Table 5.7: Achieved requirements for control circuit, based on simulation results.

General requirement G-MR1 cannot be confirmed to have been achieved, but it can be expected to have been achieved, as the dI/dt threshold has been amply achieved. Requirements C-MR4 and C-MR5 cannot be verified through simulations, since they pertain to the physical setup itself. Requirement C-MR10 can also not be verified to have been achieved, technically the copper weight of the conducting paths is less than what is requirement to safely dissipate the energy stored in the capacitor. It is expected, however, that the heat should also be able to dissipate through the IGBT and capacitor, which are rather large components, but this cannot be verified through simulations.

Regarding the conclusions that can be made from the physical tests, the following can be stated to have been achieved:

Requirement:	Achieved:	Value:
GC-MR1	–	–
C-MR1	–	–
C-MR2	–	–
C-MR3	–	–
C-MR4	–	–
C-MR5	–	–
C-MR6	Yes	0.12%
C-MR7	–	–
C-MR8	–	–
C-MR9	–	–
C-MR10	–	–
C-MR11	Yes	613, –
TR1	Yes	N.A.

Table 5.8: Achieved requirements for control circuit, based on physical tests.

Few tests were done, which is why only a few conclusions can be made.

Chapter 6

Recording

6.1 Introduction

To determine the success of the worm stimulation, it is essential to record and analyse neural activity in the worm. This analysis enables conclusions to be drawn about the worm's response to stimulation through signal visualisation. Similar methods of recording and visualising these low-voltage signals have been documented in literature with single-point electric stimulation [28][29].

However, this experiment introduces new challenges. The magnetic fields generated by the coil could potentially induce currents in the recording setup, compromising the accuracy of the recordings. While shielding electronics from an electric field is relatively straightforward, magnetic shielding is considerably more complex. Magnetic field lines can penetrate most materials, complicating the design process.

This chapter addresses the question: **How can a recording setup be designed to accurately measure neural activity in a worm?**

6.2 Programme of Requirements

Recording low-voltage signals involves numerous aspects that must be examined before the design process can commence. To delineate the design objectives, a set of requirements was established and compiled into a Programme of Requirements. The mandatory requirements in this Programme of Requirements are based on Requirements G-MR10, G-MR11, G-MR12, G-MR13 and G-MR14 of the general requirements. The trade-off requirements are both based on Requirement G-TR3 as well as the mandatory requirements set for this subgroup. This section outlines these requirements and their rationale.

Mandatory Requirements

R-MR1 | The bandwidth of the output signal is 20 Hz to 3000 Hz.

R-MR2 | The SNR at the output of the final stage is no less than 20 dB.

R-MR3 | The signal is digitally sampled at 6 kHz or more.

R-MR4 | The latency from finishing the recording to displaying the data should be less than 100 ms.

R-MR5 | External interference is removed before it reaches the sampler input.

R-MR6 | The total cost of the design must be less than €200,-.

Trade-off Requirements

TR1 | Steepen the cutoff slope for more effective filtering.

TR2 | Integrate the amplification circuit in the enclosure of the pulse generation circuit.

TR3 | The system supports a dual input for multichannel measurements.

Requirement R-MR1 pertains to bandwidth. As mentioned in Requirement G-MR10, the response of neurons must be monitored. The expected signal from the neuron is a pulse, but since the exact shape of this pulse is unknown, it was modelled as an ideal square pulse of 2ms with an amplitude of 50 µV, as seen in literature [28, 29]. Consequently, a 3000 Hz anti-aliasing filter was chosen, which is also often seen in literature [29]. A high-pass filter is implemented to reduce the amount of 1/f noise, which can distort the signal significantly [30]. Removing this greatly improves the output signal, but from around a 50 Hz high-pass filter this filtering starts to affect the recording of the neuron activation, significantly affecting the length of the peak [31]. This is undesirable, so a cutoff of 20 Hz was determined to be sufficient.

Requirement R-MR2 concerns the Signal-to-Noise Ratio (SNR). To fulfil Requirement G-MR10 accurately, so there is distinction between the response and noise, a certain SNR must be reached. With a voltage signal measurement, an SNR of 20 dB allows for noise constituting up to 10% of the signal amplitude. This ensures that noise peaks will not be mistaken for signal pulses. Considering the low amplitude of the signal, this requirement necessitates careful consideration in designing the circuit.

In literature it was found that neural signals of mammals are both noise and signal at the same time [32]. However, since a worm only has three big axons, as can be found in Appendix A, it is assumed that there is no noise generated by the other neurons. This means that this will not be of significance for this project. However, internal noise in the system will significantly impact the quality of our measurements. Also, it is crucial to minimise external noise, such as the induced current from the coils, to ensure the accuracy and reliability of our measurements.

Requirement R-MR3 addresses the sampling rate. The pulse length is approximately 2 ms, as mentioned in the explanation of Requirement R-MR1, implying a minimum sampling rate of 1000 Hz is necessary to ensure the peak is detected. However, given the requirement to use a 3000 Hz anti-aliasing filter, a higher sampling rate is required to meet the Nyquist criterion, which is twice the analog filtering rate. Therefore, a sampling rate exceeding 6000 Hz is necessary.

Requirement R-MR4 affects the latency of displaying the data. This requirement is established to realise Requirement G-MR12, because it is desirable to receive feedback on the stimulation as promptly as possible, ideally instantaneously. Given the challenges in achieving this, the requirement is somewhat lenient, allowing for the system's feedback to be pseudo-instantaneous, since this will not affect the usability of the product. Also the time of recording and stimulation needs to be taken into account, indicating 100ms gives room to achieve this and still meet Requirement G-MR12

Requirement R-MR5 is directly linked to Requirement G-MR11. The objective of this requirement is to eliminate external interference generated during stimulation to prevent the system from overloading. Given the high gain that must be implemented in the system, this requirement is essential to avoid amplifying noise and thus also links back to Requirement R-MR2.

Requirement R-MR6 was established to allocate a portion of the budget in Requirement G-MR14 to the other subsystems. Given that the control subgroup requires substantial funding, it

was determined that setting the budget at €200 would provide them with the necessary financial flexibility.

Requirement TR1 is linked to Requirement R-MR2. Since noise is present across the entire frequency spectrum, increasing the cutoff slope of the filters improves the signal-to-noise ratio (SNR). However, as there is already a requirement specifying the desired SNR, this is not a mandatory requirement.

Requirement TR2 is connected to Requirement G-TR4. Including PCBs of different designs in a single enclosure enhances the system's mobility but does not affect its core functionality, making this requirement non-binding.

Requirement TR3 relates to Requirement G-TR3. This requirement has already been discussed in Chapter 2, and the same rationale applies here.

6.3 Design Overview

To determine the setup that is going to be used, there are comparisons to be made. The setup should be able to record, digitise and visualise the activation of the neuron. For this purpose the design is divided into blocks, that are shown in Figure 6.1, which all have their own design considerations. The blocks Power Source and Display are not designed by this subgroup but significantly influence the design and will therefore be discussed.

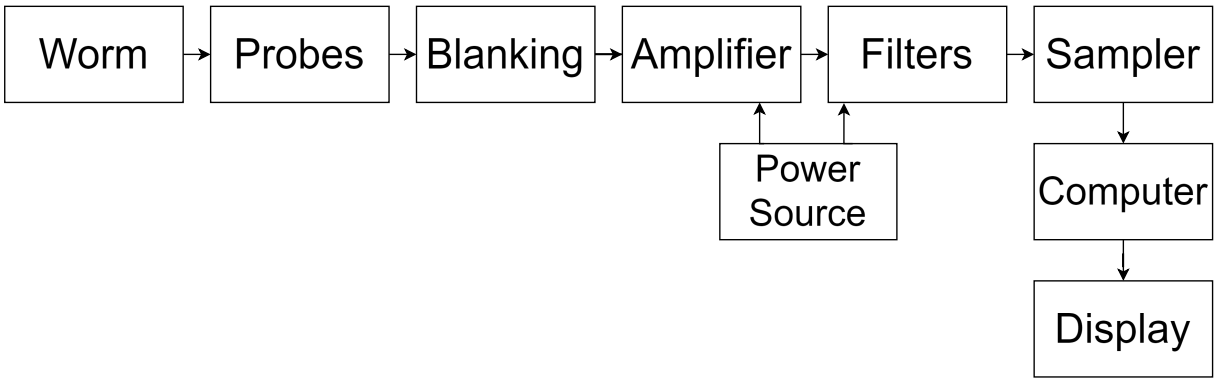

Figure 6.1: Block diagram for recording.

6.4 Possible Solutions for Design

For each requirement, considerations needed to be made that link to one of the blocks in the diagram. In this section, all the requirements are listed and connected to a block, after which the possible solutions that came up during the design process are listed.

6.4.1 SNR

The SNR links back to the block diagram's amplifier, filters and sampler. Since the components in these blocks all generate noise, different options for these need to be assessed. There are three main sources of noise in this system: $\sqrt{\text{Hz}}$ noise, Johnson noise and quantisation noise.

1. $\sqrt{\text{Hz}}$ noise is frequency-dependent and can be minimised by filtering. Given that the neural pulse length is approximately 2 ms, there is a limit to how much filtering can be applied, as specified in Requirement R-MR1.

2. Johnson noise, also known as thermal noise, arises from the resistors and capacitors in the system. It is inherent to all electronic components and can be calculated based on the system's temperature, resistance and capacitance [33].
3. Quantisation noise results from the sampler due to its internal step size. Increasing the gain of the amplifier can reduce the impact of quantisation noise because it amplifies the signal relative to the noise.

To quantify the noise, the following formula is used:

$$P_{\text{noise}} = P_{\text{Noise, ADC}} + P_{\text{Noise, Filter}} + \mathrm{G} \cdot P_{\text{Noise, Amp}}$$

$$P_{\text{Noise, ADC, max}} = \frac{V_{\text{output,max}}}{2^{R+1}}$$

$$P_{\text{Noise, Filter}} = \sqrt{\frac{kT}{C}}$$

$$P_{\text{Noise, Amp}} = \sqrt{\mathrm{B}} \cdot N$$

To calculate the SNR, the following formula is used:

$$\mathrm{SNR}_{\mathrm{dB}} = 10 \log_{10} \left(\frac{P_{\text{signal}}}{P_{\text{noise}}} \right) = 20 \log_{10} \left(\frac{A_{\text{signal,rms}}}{A_{\text{noise,rms}}} \right)$$

Where:

- G is the gain of the system.
- R is the total number of bits used by the sampler.
- N is the noise power per $\sqrt{\text{Hz}}$.
- k is the Boltzmann constant.
- T is the absolute temperature.
- C is the capacitance of the filters.
- B is the bandwidth of the signal.
- A is the amplitude of the signal

From these formulas, it can be derived that to minimise noise, the voltage at the sampler input should be as close to the maximum input voltage as possible. This implies that to meet the set requirements, the gain should be maximised. Also, it becomes clear that the SNR can be derived from the RMS voltage of the noise and the RMS value of the signal.

For this project, an SR560 amplifier [34], known for its low input noise profile of $4\text{nV}/\sqrt{\text{Hz}}$ and adjustable gain ranging from 0 to 50,000, was provided by the supervisor. This option is compared to designing a PCB that integrates a combination of active and passive components to perform the amplifying task. By evaluating both approaches, it can be determined whether using a pre-built solution or designing a custom PCB offers the best balance between cost, performance, and functionality.

6.4.2 Bandwidth

The bandwidth of the system is determined by the cutoff frequency of the filters. This means that the only block that influences this requirement is the filtering block. To reach the required bandwidth, choices have to be made. The first possibility that needs to be assessed is analog filtering. There are two options that are considered with analog filtering: single pole or double pole filters. A double pole filter has a steeper cutoff slope than a single pole filter, which could be beneficial in removing $\sqrt{Hz}$ noise. However, a double pole filter also has an added resistor, increasing the amount of Johnson noise generated.

Also, the signal can be filtered digitally. For the digital filtering, the choice needs to be made which type of filtering is applied. Since there are many options that can be chosen from, the comparison is done between an elliptical and a Butterworth filter, since these are two filter types with different characteristics which can be compared.

6.4.3 Sample Rate

This requirement is solely influenced by the sampler block in the block diagram. To meet this requirement, it is necessary to have a sampler capable of sampling at least 6 kHz. Two options are available: using a dedicated analog-to-digital converter (ADC) or employing a microcontroller to sample the analog signal. A microcontroller is already implemented in another subsystem, deeming it a viable option in meeting Requirement TR2.

There is also a choice of which microcontroller to use. Given that most microcontrollers are quite similar in price and functionality, a comparison needs to be made based on the set requirements. From this comparison, an informed choice can be made.

6.4.4 Latency

The latency from obtaining the recording and projecting it on a screen is generated in the block diagram's computer block. To minimise the latency, the functionality of the system must be optimised. The digital part of the system contributes significantly more in creating latency, due to analog-to-digital conversion processes [35]. The two options that are considered for displaying the data are an oscilloscope and a digital device of choice, that can process the data that is sampled by our sampler. An oscilloscope has the added benefit of performing sampling and instantly displaying the data. However, it severely reduces the mobility of our device and is less functional, as not everyone has access to an oscilloscope. Both options will be implemented and analysed to determine if a more portable solution can provide comparable performance to the oscilloscope output version. Therefore, it is crucial to optimise the code for converting and plotting the signal to ensure latency remains below the specified 100 ms.

In the case that a microcontroller will be used and assuming there is a lot of interference due to the magnetic field of the stimulation coil, an option that will be compared is using wireless data transfer from the sampler to the computer instead of serial communication. This catches much less interference from the magnetic field and have less latency compared to serial data communication, which is known not to be the fastest way of transporting data.

6.4.5 Interference

To fulfil Requirement R-MR5, a decision must be made regarding how and where to address interference within the system. This requirement affects the blanking block of the block diagram, since this is where the interference is removed. First it needs to be analysed whether removing interference actually is possible. If this is deemed to be possible, the two options that

are considered are removing the interference at the output or at the input of the system.

Removing interference at the output is not feasible due to the nature of the system. Amplification within the system can cause all the amplifiers to clip, negatively affecting performance and possibly destroying components. Therefore, the focus is on options for removing interference at the input. These options include removing the gain, cutting off the power, or grounding the input during stimulation.

6.4.6 Price

This requirement affects every block in the design, as each component's price contributes to the total cost. The decision-making process involves comparing the cost and performance of all potential components to ensure an optimal balance between affordability and functionality.

6.5 Design Analysis

In this section, we present the simulations conducted to evaluate whether the set requirements are met with the options considered. These simulations provide insight into the viability and effectiveness of the proposed design. Additionally, this section outlines the tests that were designed to further validate the performance and functionality of the system.

6.5.1 Bandwidth

The frequency analysis of the system is shown in Figure 6.2. The x-axis indicates the frequency range, from 10 Hz to 1 kHz, and the y-axis indicates the power of the signal in dB. The red line is the attenuation at different frequencies, the dotted red line is the phase shift at different frequencies. Since the simulations are conducted in LTSpice, the phase response automatically is plotted, though this is not necessary for this analysis. Figure 6.2 shows the frequency response of the two options.

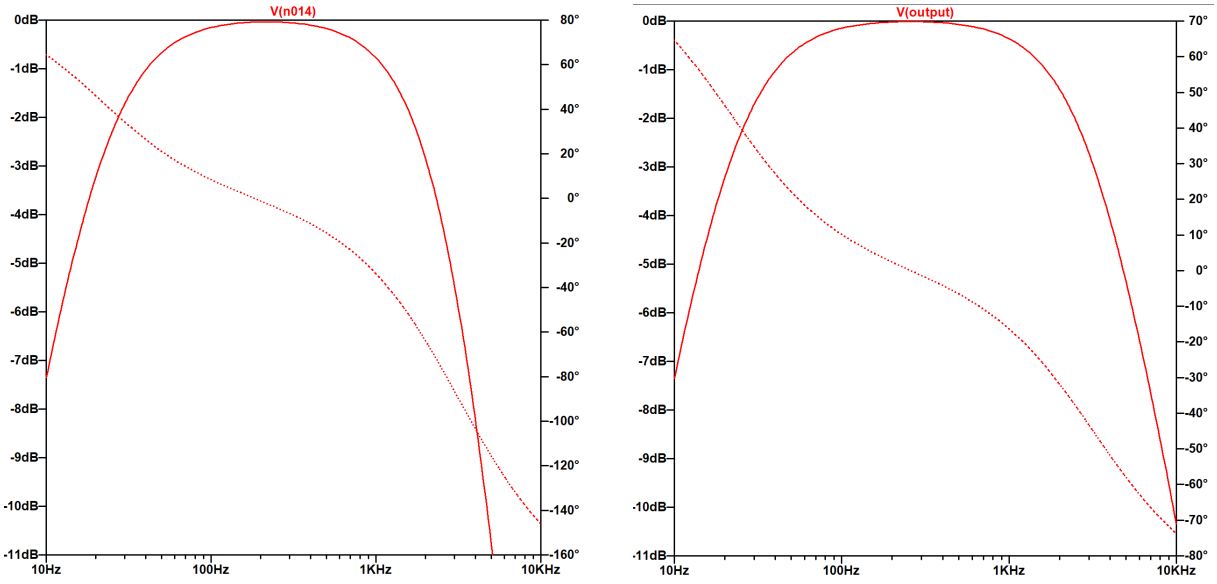

Figure 6.2: Frequency-amplitude diagram of the system with a double pole anti-aliasing filter on the left, single pole anti-aliasing filter on the right. Both of these filters meet the bandwidth requirement of 20 to 3000 Hz.

From the figure it can be concluded that both options meet the bandwidth requirement, with

the cutoff frequency being at 20.9 Hz for the high-pass filter and at 3180 Hz for the anti-aliasing filter.
For digital filtering, a Butterworth filter and an elliptic filter are simulated. The Butterworth filter is evaluated at a pass-band frequency of 500 Hz and a stop-band frequency of 1500 Hz, with an order of five. The elliptic filter is evaluated at a pass-band frequency of 1400 Hz and a stop-band frequency of 1500 Hz, with an order of seven. The 1500 Hz was determined as a placeholder value, as it is half of the analog low-pass filter. This way it was possible to evaluate the steepness of the cutoff slope and the length of the passband.
The frequency responses of these signals can be found in Figure 6.3 and Figure 6.4. On the x-axis of the figures, the frequency can be seen in Hz. On the y-axis of the figures, the power is shown in dB. As can be seen in these figures, the elliptic filter has a steeper cutoff slope than the Butterworth filter.

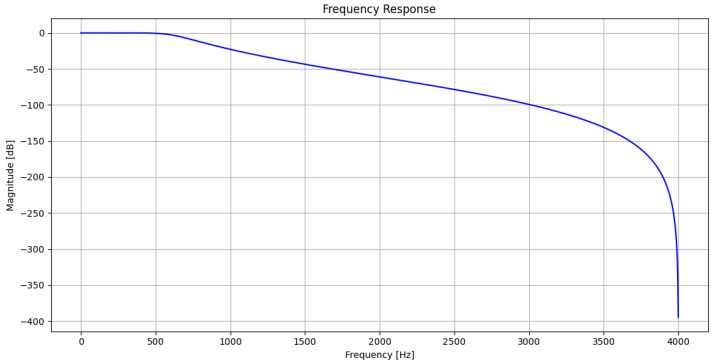

Figure 6.3: Frequency response of the Butterworth filter with a passband of 500 Hz to 1500 Hz

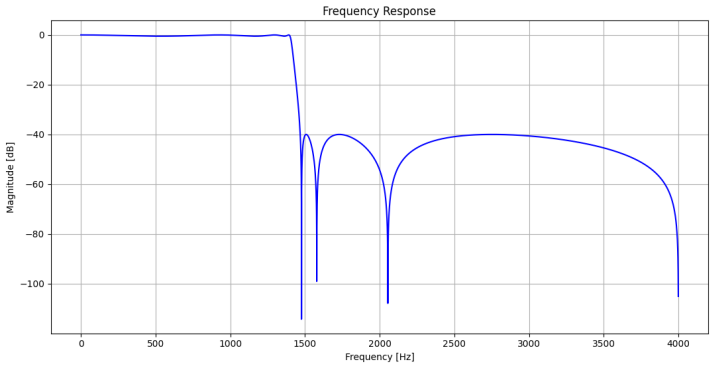

Figure 6.4: Frequency response of the elliptic filter with a passband of 1400 Hz to 1500 Hz

6.5.2 SNR

Requirement R-MR2 is to achieve an SNR of 20 dB. Internal noise is generated in the measuring device due to noise-generating components. The SNR and the noise voltage that is reached with each option is displayed in Table 6.1. From this table can be concluded that all three options meet the noise requirement.

The RMS Noise Voltage of the SR560 is significantly higher than the pole filters, independent of the amount of poles that are set. From the table can be derived that the steeper cutoff slope outweighs the added resistor noise in the double pole anti-aliasing filter.

Filter type	RMS Noise Voltage [V]	SNR [dB]
Single pole anti-aliasing	$1.91 \cdot 10^{-3}$	57.9
Double pole anti-aliasing	$1.50 \cdot 10^{-3}$	60
SR560	$6.6 \cdot 10^{-3}$	47.2

Table 6.1: Noise figures of different filters. All these filters meet the SNR requirement.

6.5.3 Sample Rate

To analyse the sampling rate, the sampling rate of the ESP that was already in possession is compared to that of a standard audio converter, which is the cheapest and most conventional option available. The results of this comparison are shown in Table 6.2.

	Microcontroller	Analog-Digital converter
Price (€)	11,99	40,95
Sampling frequencies:	$1 - 2 \cdot 10^6$ Hz	32, 44.1 kHz, 48 kHz, 96 kHz

Table 6.2: Noise figures of different filters. It can be seen that both samplers meet the sampling frequency requirements.

From the table, it can be concluded that both samplers meet the set requirement. However, the audio amplifier is less modular than the microcontroller, making it a less favorable option.

6.5.4 Latency

Analysing the latency is a difficult task, since it is yet unknown what the code will look like and how much latency a specific digital device will have. For the latency analysis it was chosen to look at the difference of speed in communication between serial and wireless communication, which is also a possible design choice that needs to be made. In Table 6.3 the comparison in theoretical communication speed is shown. In practice, the communication speed is way lower. The serial communication speed is dependent on the hardware and software limitations. The wireless communication speed is affected by more overheads, such as network congestion and signal strength.

	Serial communication	Wireless communication
Maximum communication speed (Msps)	5	1

Table 6.3: The theoretical communication speed of two connection types. Though both are fast in theory, due to overheads the actual speed is lower.

6.5.5 Interference

During simulation, it was found that blanking the power input of the instrumentation amplifier can cause stability issues when the input voltage is too high, rendering this option not viable. Blanking the input is found to be efficient since no stability issues occur through this and the output receives no signal from interference. To validate the efficacy of the approach, the propagation time of the neuron signal through the worm was calculated, which is in the order of 5 ms, given that the length between the coil and the probes is 10 cm and the propagation speed is around 20 m/s. Given that the duration of the magnetic pulse and its decay occurs within the microsecond range, it is feasible to blank out a time frame of a millisecond to effectively eliminate magnetic interference. A derivation of the maximum blanking time is seen in Table 6.4.

	Time	
Propagation time	5 ms	+
Pulse time	$1 - 10$ µs	-
Decay time	$50 - 100$ µs	-
Total maximum	4.890 ms	

Table 6.4: Derivation of maximum blanking time, showing blanking the external interference is possible.

Due to uncertainty of the coil that will be designed and it's characteristics, it was assumed that the magnetic field at 50 cm distance does not influence any of the electronics after the blanking stage.

6.6 Design Choice

During the design process, it was essential to compare the potential solutions and decide which option to implement. For each block, possible options were considered and eventually a choice is made which option to use. This section provides an explanation of the choices that were needed to be made for each block and the reasoning behind those choices.

6.6.1 Probes

To obtain the signal from the worm, probes are necessary to transmit the electric signal directly to a reading device. Initially, surface probes were considered, but due to the worm's anatomy, non-invasive methods were deemed ineffective since they would decrease the SNR. Given the objective of measuring the neural signal as directly as possible, needles were identified as the optimal solution. The first consideration was to use EMG needles [36], which are specifically designed to measure neural stimulation by obtaining information from motor cells. However, this approach was unsuitable for the project's needs, as the responsiveness of the muscle cells might decline when sedated [37]. This way the SNR rises, which is needed to be kept at a low point in accordance with Requirement R-MR2. Also, the EMG needles are expensive, which interferes with Requirement R-MR6. For this project, bug pins are expected to provide adequate results. Additionally, these pins can also serve to immobilise the worm, thus fulfilling a dual function.

In Table 6.5 the comparison of the prices of EMG needles to that of bug pins can be found. The prices of EMG needles were derived from literature[36].

	EMG needles	Bug pins
Price (€)	7,-	4,50/100 Pc

Table 6.5: Prices of different needles. EMG needles are significantly more expensive than bug pins.

6.6.2 Sampling

It is important to establish a method for transmitting and visualising the data. For visualisation purposes, the signal needs to be digitised. It was decided to implement the microcontroller as a sampler. This approach also minimises the number of components, since multiple functionalities can be combined. A comparison of options for this implementation is presented in Table 6.6.

Variable:	ESP32	Arduino Uno R3	STM32	Weight
Price (€)	11,99	24,-	23,64	2
Resolution (bits)	12	10	12	3
Implementation language	C	APL (C/C++)	C	1
Maximum Sampling Rate (kHz)	2000	10	5000	3
Maximum Voltage Input (V)	3.3	3.3	4	1
Wireless Capabilities	+	-	+	2

Table 6.6: Comparison of different sampler design choices, showing the ESP is the preferred option.

From this table, it was concluded that using an ESP [26] to convert the analog signal to a digital signal and also transport it is the best option. The primary advantage of utilising an ESP is its capability for wireless data transfer, which reduces the need for cables. This greatly enhances the system's mobility and ease of troubleshooting, and it also eliminates the possibility of interference after sampling since there are no wire loops in which current can be generated. The STM has multiple advantages, but as the ESP is already in our possession and it meets all of the requirements, that one is preferred.

To achieve high resolution, an 8 kHz digital sampling frequency was chosen. This frequency enhances the quality of the plots while maintaining a manageable amount of data for storage and transmission. Since it was established that an ESP will be used to convert the signal from analog to digital, the sampling rate of this device has to be checked to see whether it meets the requirements. According to the datasheet, the maximum sample rate of the ESP is significantly higher than 8 kHz, ensuring that the requirements for this part of the system are met.

6.6.3 Amplifier

To ensure effective signal amplification, it is crucial to study various aspects of amplification. The primary goal of the system is to suppress noise as much as possible, following Requirement R-MR2. Various amplification methods were explored, the most applicable being designing a printed circuit board (PCB) to house a collection of integrated circuits or utilising the provided SR560 amplifier. Table 6.7 compares the two most feasible options, highlighting their respective advantages and limitations.

Variable:	SR560	A.M.P. Amplifier	Weight
Price (€)	8000,-	130,-	2
Maximum voltage output (Vpp)	10	12	1
Noise figure (nV/$\sqrt{Hz}$)	$120 \cdot 10^3$	$27.5 \cdot 10^3$	2
Common Mode Rejection Ratio (dB)	90	120	1
Maximum gain	50000	15000	1
Multichannel	-	+	2

Table 6.7: Comparison of different amplifier design choices, showing the SR560 is dominant in most categories.

The table indicates that the A.M.P. amplifier appears to be the superior option for this project. However, since multichannel is a trade-off requirement and both options are viable, both will be utilised and compared subsequently to determine the optimal choice for this application.

After determining that the ESP would serve as the ADC for this project, the requirements for the amplifier became clearer. The ESP can measure voltages between 0 and 3.3 V, neces-

sitating that the amplifier outputs a signal within this range. Given that the expected signal is bipolar, an offset of 1.65 V is required. The conversion does have margins for which voltages and frequencies the ADC is usable. Even though a 0 to 3.3 V range was used to consider the ESP, by changing the attenuation settings, different voltage margins exist. In Table 6.8 these margins can be seen.

Attenuation	Low margin	High margin
0 dB	70 mV	1.05 V
2.5 dB	70 mV	1.40 V
6 dB	70 mV	1.90 V
12 dB	70 mV	3.15 V

Table 6.8: Margins of voltages for different attenuation settings. From this can be concluded that the 12 dB setting is the best option.

The smallest distance to a margin from the 1.65 V needs to be taken as an upper limit for the signal since the signal is bipolar and has the same amplitude in both directions. It was decided that the attenuation of 12dB was to be used as the larger gap between its lower boundary and upper boundary results in a higher resolution. The signal peaks range from $-50\,\mu V$ to $50\,\mu V$, so to avoid clipping and stay within the margins of 0.15 V to 3.15 V, an amplification factor of 30,000 is necessary. As the SR560 amplifier features a differential input with a common-mode rejection ratio exceeding 90 dB for signals under 1 kHz, an instrumentation amplifier is incorporated at the input stage of the A.M.P. amplifier. This configuration ensures that the signal is measured differentially, aligning with the standard practice in literature on recording neural signals with electrical stimulation [28, 29].

The ESP can handle voltages between 0V and 3.3 V, so it needs to be ensured that this threshold is not passed. To do this, two diodes will be put parallel to the input of the ESP to a 0 and a 3.3 V rail. This will ensure the ESP is not destroyed when the amplifier clips. Given the significant role of noise in these measurements, selecting amplifiers with low noise profiles is crucial. For the choice of the integrated circuits the Texas Instruments website was filtered on the requirements that were set. The instrumentation amplifier that was chosen for the input is the INA849, since this amplifier has an extremely low noise profile. For the filtering stage the OPA1612 is chosen, since this amplifier has two amplifiers integrated and also has a noise profile of $1 nV/\sqrt{Hz}$. Since the INA849 cannot achieve a gain of 30,000, a gain of 3000 is implemented in the instrumentation amplifier stage and a gain of 5 is implemented with the operational amplifier in the anti-aliasing filter stage.

6.6.4 Filtering

Filtering is done by implementing an RC circuit that cuts off the frequencies below or above a certain frequency. By changing the position of these components it can become either a high-pass or a low-pass filter. For the analog filtering two possible options were considered, namely active filtering and passive filtering. However, since passive filtering is less efficient at low frequencies, it was chosen to use active filters for the design. As per Requirement TR1, steepening the cutoff is desired. Considering single and double-pole filters, a single-pole high-pass filter and a double-pole anti-aliasing filter were selected for implementation. The decision to avoid a second-order high-pass filter stems from stability concerns and the lack of necessity for aggressive filtering below 20 Hz. The double-pole anti-aliasing filter was included to ensure adequate noise removal for the system's BNC output, intended for oscilloscope use, without relying on digital filtering.

Since noise is dependent on bandwidth, it is crucial to minimise the bandwidth to ensure an

optimal signal-to-noise ratio. Therefore, digital filtering will be applied after sampling. This approach preserves most of the relevant information while significantly reducing the total noise figure. During digital filtering, a bandwidth of 20 Hz to 1500 Hz is analysed to determine if it is sufficient for recording neural signals. This bandwidth is compared to the 3000 Hz bandwidth of the analog filter. The analysis will indicate whether the commonly set bandwidth of 20 Hz to 3000 Hz is necessary or if the signal can be accurately represented within the smaller bandwidth. To fulfil Requirement TR1 it was decided to use the elliptic filter for digital filtering, since this has a much steeper cutoff and can be implemented with a much smaller passband. This significantly enhances the resolution of the output signal, resulting in more readable plots and a higher SNR. A filtered DC signal compared to the original signal can be seen in Figure 6.5. On the x-axis the time is shown in milliseconds, on the y-axis the output value of the ESP is shown. The input signal of the ESP is 700 mV, indicating a small offset can be noticed.

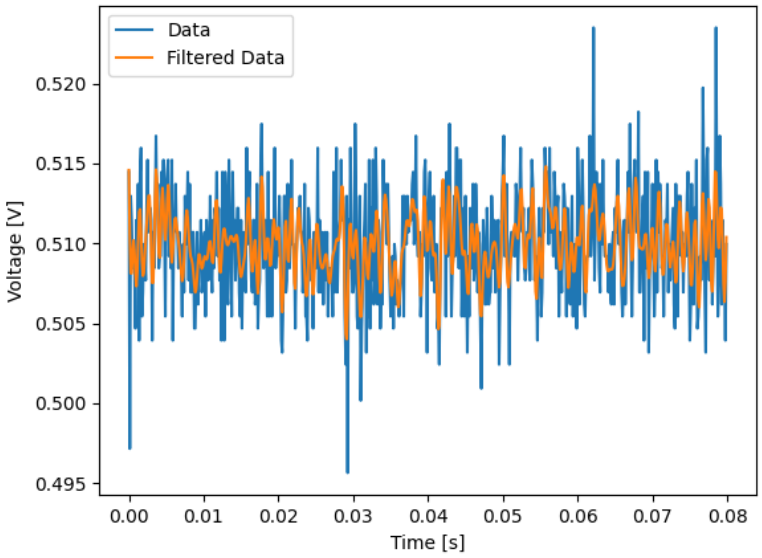

Figure 6.5: A DC signal and a filtered signal. This shows the digital filtering has the desired effect on the noise, e.g. suppressing it.

6.6.5 Blanking

To mitigate the risk of amplifier overload and over-voltage at the ESP input caused by induced currents and voltages in the cable loops between the needles and the amplifier, precautions are necessary due to the magnetic field generated by the coils. As per Requirement R-MR5, it is necessary to ensure external interference is removed before it reaches the sampler input. To address this, a blanking circuit is implemented, incorporating a multiplexer that opens the circuit upon receiving a high voltage at the gate. This high signal, managed by a microcontroller, activates when the inductors are turned on. This mechanism prevents overloading and ensures that the voltage peak induced in the worm is properly transmitted to the amplifier. A schematic overview of this process is seen below in Figure 6.6.

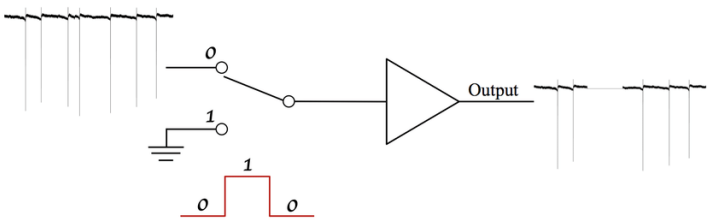

Figure 6.6: The workings of a blanking circuit[38].

During the design stage, three options for blanking were considered: blanking the gain resistor, blanking the power supply and blanking the signal. Simulations revealed that grounding the signal during blanking yielded superior results. This approach ensures that no unwanted signal reaches the amplifier, thereby maintaining the integrity of the measurements. Conversely, blanking the power supply or the gain resistor could introduce stability issues when the input voltage exceeds a certain threshold, potentially compromising the system's performance. Thus, grounding the signal was determined to be the more effective method for blanking in this application. In order to ensure that the loop created to ground is small enough that there will be no current induced, the ground is inserted onto the PCB as a plane. Also, the PCB is placed at an angle, setting the magnetic field lines parallel to the traces. The multiplexer that was chosen to switch the input from signal to ground is the CD4053B, since this multiplexer has two 2:1 multiplexers inside a single enclosure, which means there is only one integrated circuit needed for this implementation. This choice was based on filtering the Texas Instruments website on the requirements for this specific component and choosing the one that matches all.

6.6.6 Computer

For displaying the data, a link is established between the ESP and the device on which the data will be displayed. To ensure real-time visualisation and to accommodate the ESP's limited data storage, data cannot be sent only after the entire measurement is completed; instead, a constant connection must be maintained.

Serial communication was considered for this connection, but it has several drawbacks. Serial communication is prone to transmission errors, different operating systems require different programming to read the serial data, and using the communication cable for data transmission precludes its use for other purposes, such as debugging. Therefore, communication between the ESP and the visualisation software is established via an internet connection. Maintaining a constant data stream through the internet and plotting it as the information arrives is impractical. Consequently, an alternative approach was chosen: data is transmitted in chunks. If the chunks are too large, the transmission will slow down. Thus, it was decided to transmit chunks of 128 samples. With an 8 kHz sampling rate, this results in a new chunk being transmitted every 16 ms.

To visualise the measurements, the signal is input on two pins of the ESP. Next the average of these two inputs is taken to offset transmission errors. Due to the Direct Memory Access (DMA) of the ESP, the analog to digital conversions can still take place while the data is transmitted and a flag is raised when the amount of data is above a certain threshold. After the data is sent, the total measurement is plotted. This way a pseudo-real-time visualisation is achieved. The code used to obtain and process the data from the ESP can be viewed in Appendix B.

6.6.7 Power Supply

The power supply required for this design must provide three ports: +12 V, GND, and -12 V. This configuration is necessary because the input voltage of the instrumentation amplifier can be both negative and positive. Consequently, a negative supply voltage is required to accommodate the input and output swing of the amplifier. The choice of 12 V was made as it is a standard value for power supplies, which makes it easy to implement. Internally, the 12 V supply is also used to set a biasing voltage of 1.65 V.

The 1.65 V bias is implemented at the output of the instrumentation amplifier since this has a reference input. An alternative approach was to bias the instrumentation amplifier at the probes, which would eliminate the need for a -12 V rail. However, to avoid causing unnecessary harm to the living organism being measured, this approach was not adopted. Also, a voltage divider with a buffer amplifier was chosen to create the 1.65 V bias. This method minimises the current through the resistors and ensures that the output voltage remains constant. Although using a dedicated 1.65 V power rail was another option, this was deemed excessive since this voltage is only needed on this PCB.

6.6.8 Display

It was established earlier that the ESP will function as a web host, allowing digital devices to connect via Wi-Fi. This capability means the device can be used with a laptop, mobile phone, or tablet, significantly enhancing its mobility and usability. Additionally, the device can be connected to an oscilloscope after the amplification stage with a BNC connector to increase functionality and simplify testing.

6.7 Implementation

In this section the realisation of our design is outlined together with the tests that will be performed on this design. The results of these tests will be shown in the section Results and Discussion.

6.7.1 Schematic

In Figures 6.7 and 6.8 the schematic and the configured PCB of the complete design are shown. The stages blanking, amplification and filtering can be seen from left to right. The capacitors on the bottom of the screen are implemented close to the integrated circuits, to ensure their supply power stays constant. The values for the components at each node are shown in Table 6.9.

Component:	Value:
R1	2 Ω
R2	1 MΩ
R3	3.2 kΩ
R4	15 kΩ
R5	9 kΩ
R6, R7, R8	1 kΩ
R10	20 kΩ
C1	500 nF
C2,C3	50 nF
C4,C5,C6,C7,C8,C9,C10	100 nF

Table 6.9: Component values

The values R4, R7, R8, C1, C2, and C3 were specifically chosen to determine the cutoff frequencies of the filters. Capacitors C4 through C10 were selected to mitigate voltage ripple at the power supplies of the integrated circuits. The resistors R3 and R10 were chosen to divide the voltage, thereby biasing the circuit to 1.65 V. R1 was selected to set the gain of the instrumentation amplifier, while R5 and R6 were chosen to set the gain of the first operational amplifier. The purpose of R2 is to ensure that the leakage current of the instrumentation amplifier does not load the worm. Two of the PCB's will be used to monitor two different signals received from the worm. These signals will be sent to the ESP, where they will be sampled. At the input of the buffer amplifier an NMOS is implemented to be able to reset the system when overloading occurs, since this is also implemented on the SR560. To protect the input of the ESP from voltage exceeding the specified range, two Schottky diodes will be implemented. However, these diodes will be placed on the breadboard of the ESP, as the PCB does not include a 3.3 V power rail.

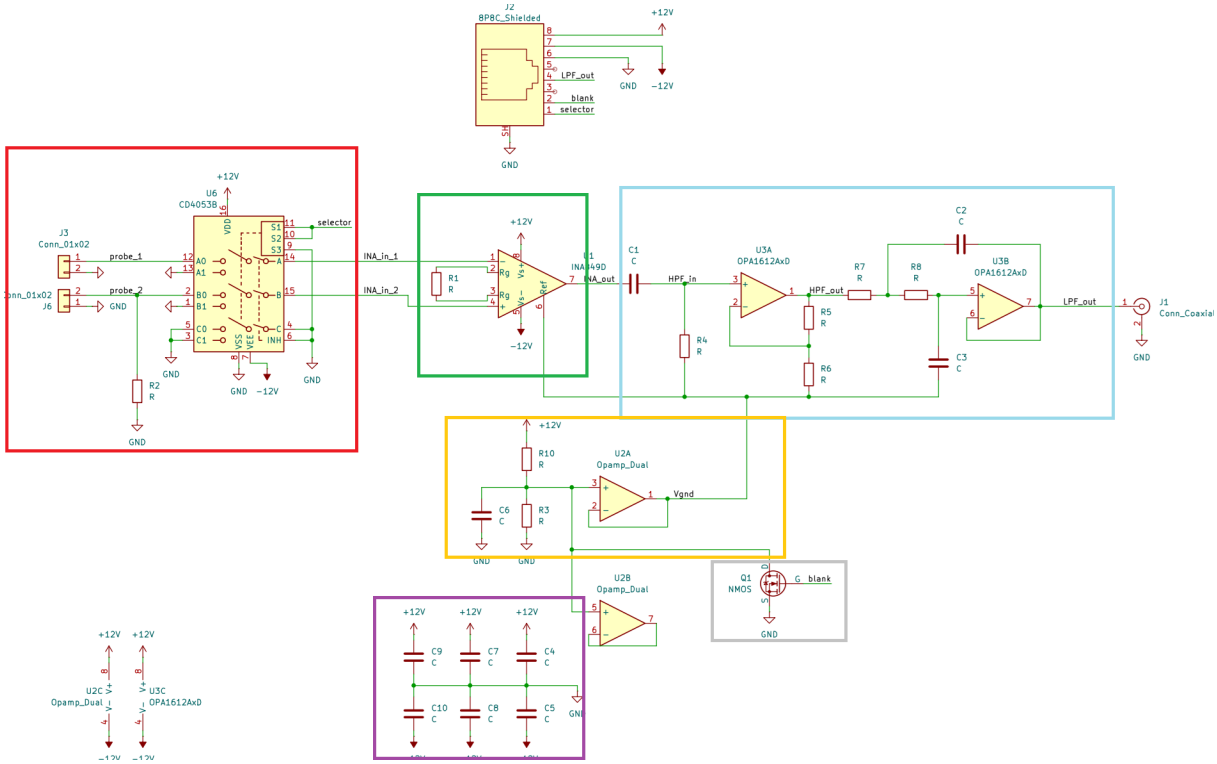

Figure 6.7: Overview of the entire schematic. The red box is the blanking stage with the input pins and a deloading resistor, the green box is the instrumentation amplifier with the gain resistor, the light blue box is the high-pass filter and the anti-aliasing filter, the orange box is the buffer amplifier with the voltage divider and a decoupling capacitor, the purple box are the decoupling capacitors for the INA849 and the OPA1612 and the grey box is the reset NMOS. The Ethernet connector has connections for all the output and input signals.

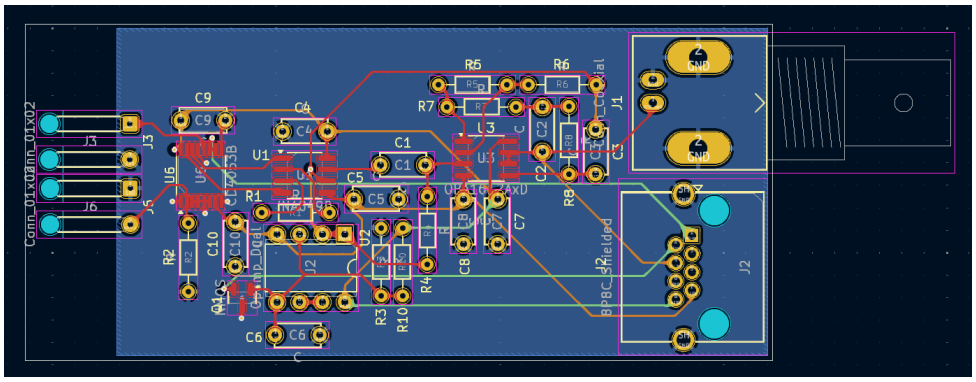

Figure 6.8: An overview of the PCB.

6.7.2 System Testing

To ensure that the system functions as intended, several tests have been designed. These tests are outlined in Figure 6.9 within the red boxes. Each test is performed to verify that the set requirements are met.

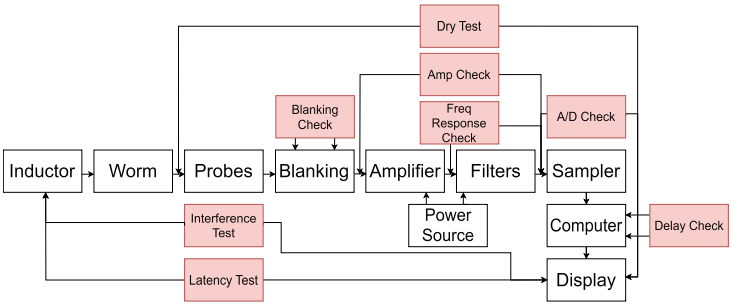

Figure 6.9: Block diagram of the recording system.

The first test conducted is the interference test. This involves activating the coils and measuring the output to assess the total interference. The interference should be minimal since the input of the instrumentation amplifier is blanked.

The second test is the dry test, performed on the entire system using a dummy subject, such as a function generator or a wet sponge. This test provides insight into the signal transmission through the system, which is crucial for determining the system's readiness for testing on live worms. It is important to conduct this preliminary testing to avoid causing unnecessary harm to the worms. From this test the SNR can also be derived, since each component is cascaded and the total output noise can be measured.

The third test is the latency test, which measures the time delay between the end of recording a signal and the display of the data. This is accomplished by closely monitoring the timestamps recorded by the ESP and the duration taken to execute the code.

The last tests are the amp check, the frequency response check, the blanking check, the sampler check and the delay check. These are tests conducted on each specific block to see whether the required functionality is available. This can be done by sending signals from a function generator into each block and reading the output with an oscilloscope.

6.7.3 Realisation

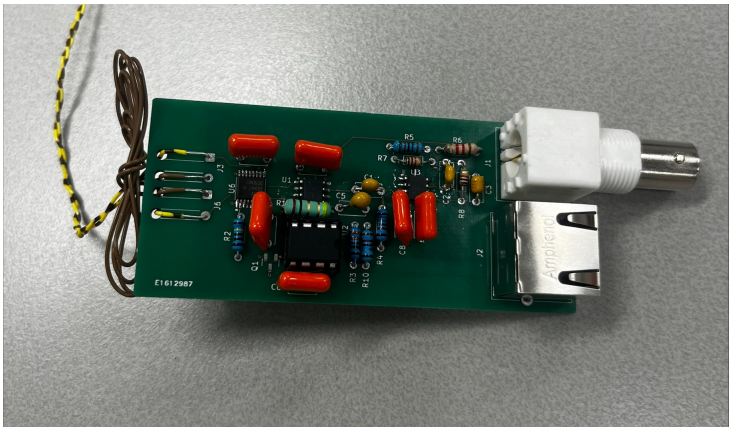

Figure 6.10: Physical realisation of the design.

In Figure 6.10 the realised design can be seen with all the components. The total price of the design is €130,-, which is the combined price of the PCB's and the components. The components were ordered from Mouser and the PCB's from Eurocircuits.

6.8 Results

In this sections the results from the tests on the physical realisation of the design are presented. These results are discussed and compared to the requirements from which is concluded whether they match the theory of the analysis. The testing is split up in two categories: Digital Testing and Analog Testing. Digital Testing consists of the A/D Check and the Latency Test, Analog Testing consists of the Freq Response Ceck, the Amp Check and the Dry test. The Interference Test can only be completed when connecting the subsystems and will thus not be discussed in this section.

6.8.1 Digital Testing

To investigate whether the sampling and conversion is done in a correct manner, the ESP with ADC can be connected to a function generator. As the figure of the function generator is known, it can be compared to the sampled and converted signal. In Figure 6.11 the comparison between the original and the sampled signal can be seen.

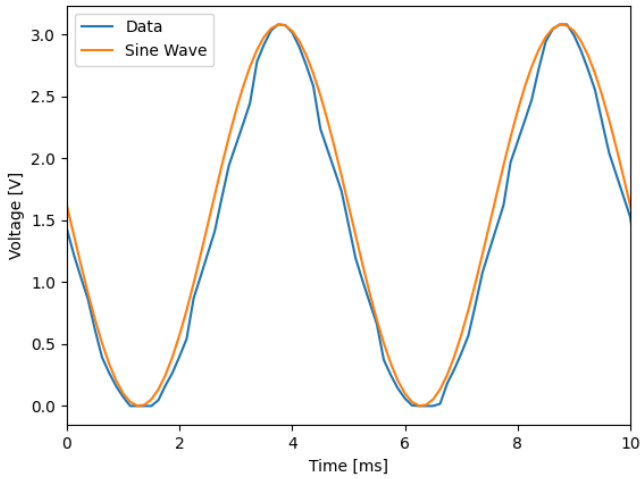

Figure 6.11: Original signal and signal after sampling by the ESP. The sampling rate of the ESP meets the requirement of 8 kHz. The sine achieves two full periods in 10 ms, confirming the 200 Hz frequency of the signal.

The x-axis indicates the time in milliseconds, and the y-axis indicates the amplitude of the signal in volt. The blue line displays the sampled signal retrieved from the output of the ESP, the orange line is a sine wave of 200 Hz with 8000 samples per second, as outputted by the function generator. For each signal a total of 80 samples are plotted. As can be seen, the converted signal closely represents the original signal, indicating the conversion works as intended. Also, from the figure can be derived that the sampling rate of 8 kHz is reached, since the figure fits 80 samples in 10 ms.

To measure the latency, a Python code is run on a test dataset to see whether it meets the latency requirement. A timer is implemented that shows the duration of running the code, when it obtains data. This code was run on a HP Probook 440 laptop, since a laptop is the device that is most commonly used. From this timer it was derived that the latency between obtaining the data, filtering and then plotting the data, is 21.12 ms. In Table 6.10 the results for both tests are shown.

Test:	Result:
Sampling Rate	8000 Hz
Latency	21.12 ms

Table 6.10: Results of the tests performed on the digital part of the measuring device.

6.8.2 Analog Testing

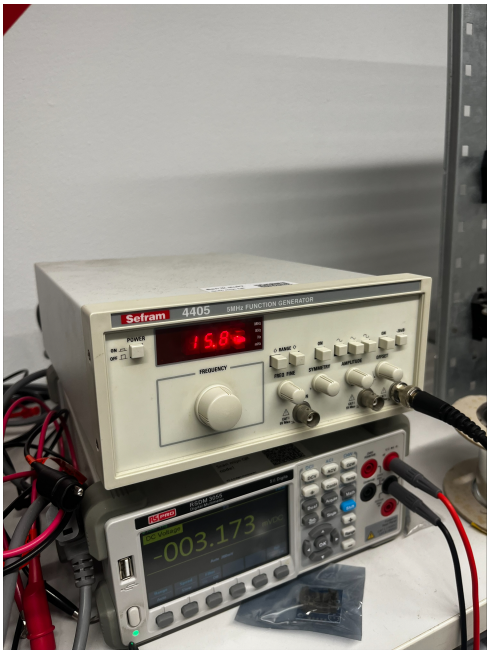

Figure 6.12: Picture of the function generator setup which generates a sine at a frequency of 15.8 Hz.

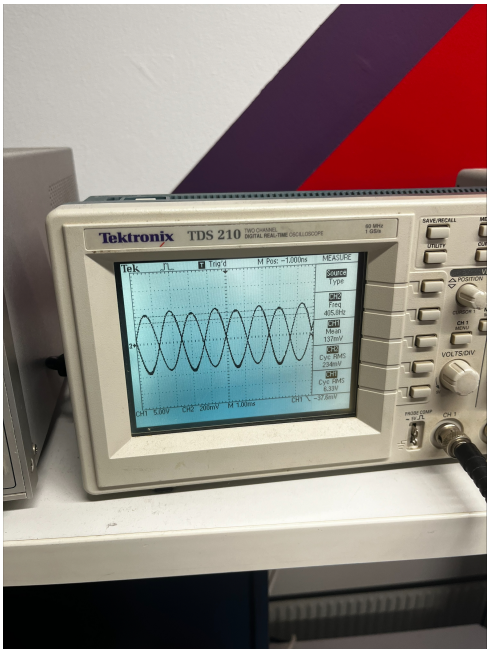

Figure 6.13: Output signal of the measuring device and the output signal of the function generator with a frequency of 400 Hz plotted on an oscilloscope. It can be seen that the amplitude of both signal is matched, enabling cutoff frequency detection by adjusting the frequency knob of the function generator.

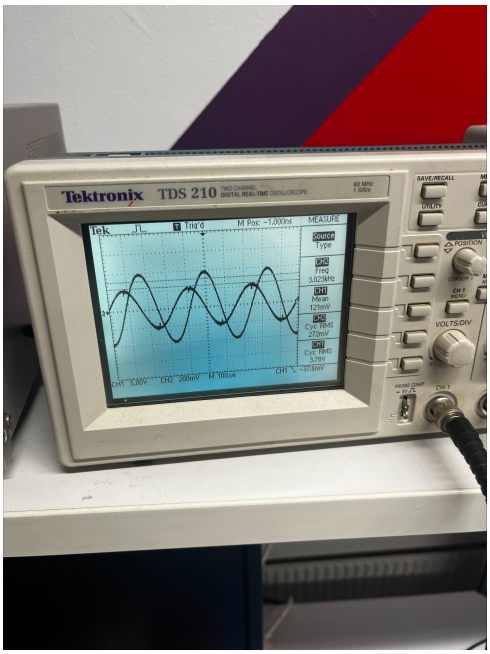

Figure 6.14: Output signal of the measuring device and the output signal of the function generator with a frequency of 3 kHz plotted on an oscilloscope. It can be seen that the amplitude of the signal is halved, indicating the cutoff frequency of the anti-aliasing filter is correct.

The device cutoff and the device gain was tested by feeding a sine into the measuring device, as can be seen in Figures 6.12 and 6.14. This gives insight in whether the requirements that were set are met. The gain of the system could be derived by comparing the output of the measuring device to the output of the function generator. From the signal RMS value the cutoff frequency could be derived, since the signal should be attenuated with a factor $\sqrt{2}$ for the high-pass filter and a factor 2 for the anti-aliasing filter. The blanking check was performed by putting a +12 V signal on the multiplexer selector and checking whether any signal went through. In Table 6.11 the results for all tests are displayed.

Test:	Result:
Bandwidth	15.8-3000 Hz
Gain	$2,7 \cdot 10^4$
Blanking	-20 dB
SNR	???

Table 6.11: Results of the analog tests performed on the A.M.P. amplifier. It can be seen that three of four requirements are met, failing the dry run test.

From the noise test it was concluded that the noise power is a lot higher than anticipated. This is because there is an oscillation of 1.6 V RMS at 23 MHz that is generated in the anti-aliasing filter, which was not resolved by removing the capacitor of the double-pole filter. Since this oscillation cannot be described as noise, the SNR could not be defined. Because of this phenomenon the dry test could not be performed and the SNR could not be derived.

6.9 Discussion

Due to errors in the physical realisation of our design, an oscillation of 23 MHz occurred at the output of the A.M.P. amplifier. This issue likely originates from the operational amplifier or the capacitor in the second stage of the anti-aliasing filter. However, removing this capacitor did not resolve the problem. For future research, it would be beneficial to analyse the source of this oscillation, as it significantly interferes with the device's measurements.

6.10 Conclusion

This chapter addresses the question: **How can a recording setup be designed to accurately measure neural activity in a worm?** This is achieved by designing an amplification, filtering, and sampling setup capable of transferring the recorded data to a digital device for display. Six primary requirements must be met: bandwidth, SNR, sampling rate, measurement delay, interference and price. These are linked to Requirements G-MR10 to G-MR14. Six out of six of these requirements are satisfied due to the choices in the design of the filters, both analog and digital, the amplifier and the sampler. However, in the realisation of the A.M.P. amplifier only four out of six of the mandatory requirements are met. Additionally, there are three trade-off requirements, of which one is met: cutoff slope steepening. Consequently, our design not only meets but also surpasses the established standards. In Table 6.12 the final values of our design requirements can be seen and it can be seen which trade-off requirements were met.

Requirement:	Achieved:	Value:
R-MR1	Yes	20-3000 Hz
R-MR2	Yes	60 dB
R-MR3	Yes	8 kHz
R-MR4	Yes	21 ms
R-MR5	Yes	-20 dB
R-MR6	Yes	€130,-
TR1	Yes	–
TR2	No	–
TR3	Yes	–

Table 6.12: Evaluating the requirements. It can be seen that all of the mandatory requirements are met and two of the trade-off requirements are met.

6.11 Recommendation and Future Work

During the design process, many decisions were influenced by the goal of building an amplifier that closely matches and exceeds the specifications of the SR560, as this was the device used by our supervisor and his team for recording neural activity. However, the SR560 is not optimised for neural recordings of worms, presenting an opportunity for improvement. Literature reveals that recording worm neural signals is not yet optimised, as most research in this area is conducted by medical researchers rather than electronics researchers. This indicates that it is still recommendable to conduct research on this topic. For future research, it is recommended to make the design more modular, allowing for adjustable gain and bandwidth. This modularity was not implemented in the current design.

Chapter 7

Implementation

In this chapter the implementation of the complete design is shown, with all the subsystems connected. Also, all the tests that were designed to test the interconnected functionality of the device are presented and explained.

7.1 System testing

In Figure 3.2 all the tests conducted on the system are shown. However, most of the tests were conducted on subgroup level and are not applicable in this section. In figure 7.1 all the tests that are discussed in this section are shown.

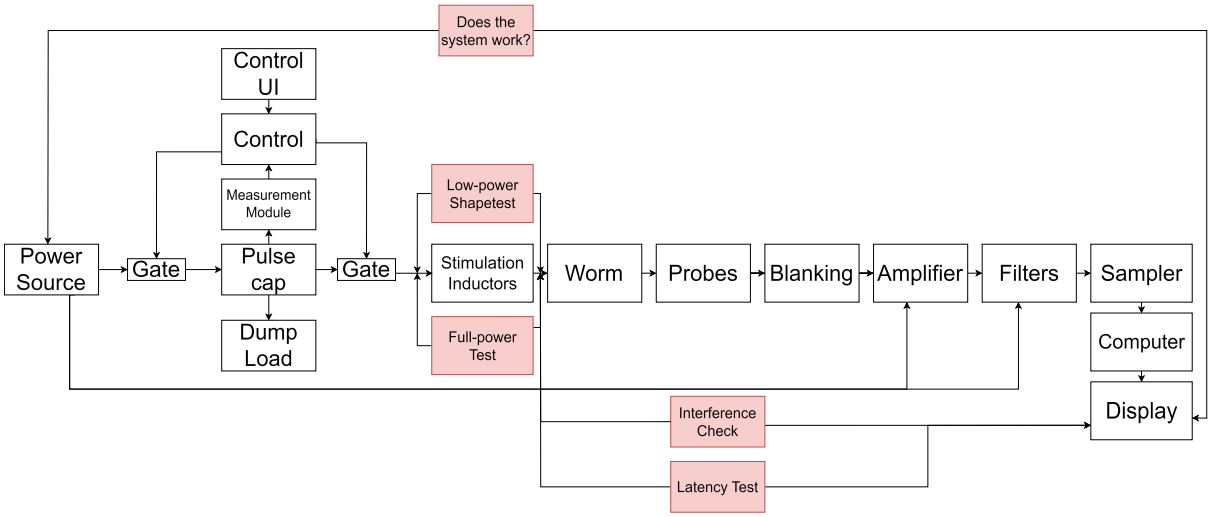

Figure 7.1: The full design block diagram with tests.

The first test that is conducted is the Interference Check. This will indicate whether the induced EMF in the recording system is seen at the output of the system, which is not desired as per requirement G-MR11.

The second and third test are the Low-power Shapetest and the Full-power Test. these tests will indicate whether the RLC circuit functions correctly. The shapetest will be performed on a low capacitor voltage and shows if the assumed impedances are in the correct range. The voltage is then tuned up to test if the circuit components can handle higher voltages, and whether the coil does not heat up too much.

The fourth test is the Latency Test. With this test the total latency of the system is measured, indicating whether Requirement G-MR12 is met.

The final test that is performed is the Does the system work? This is the test that will be performed on a worm that indicates if trade-off requirement G-TR1 is met.

7.2 Realisation

In figure 7.2 the realisation of the complete design can be seen. All the the subgroup designs are realised, completing the device. From the figure can be derived that requirement G-TR4 is met, since it is possible to move this device as a single person.

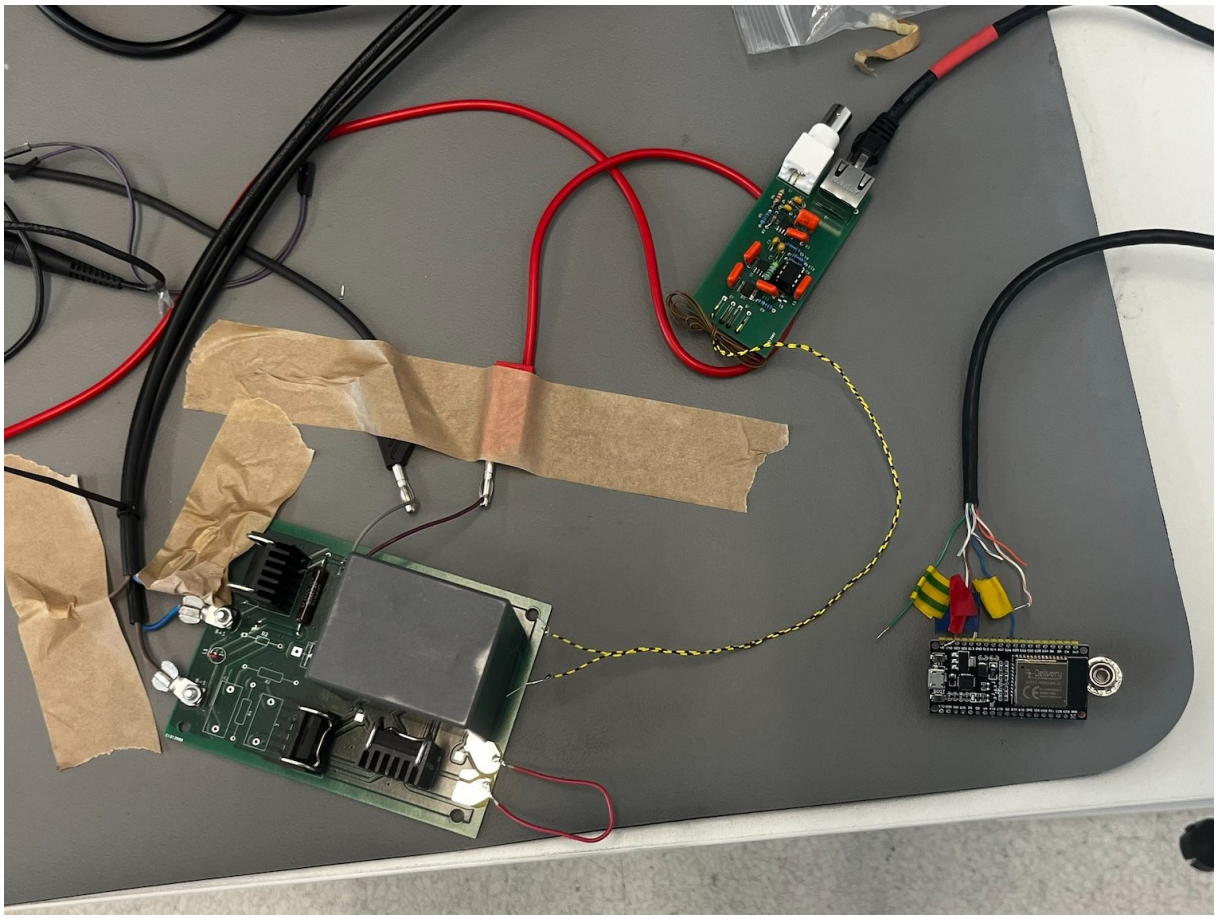

Figure 7.2: The realised design. All the subsections are present: Stimulation, Control and Recording.

Chapter 8

Results and Discussion

In this sections the results from the tests on the physical realisation of the design are presented. These results are discussed and compared to the requirements from which is concluded whether they match the theory of the analysis. Also a brief explanation of the result of each test is given.

8.1 Test Results

Due to assembling problems that arose it was not possible to perform the Interference Check, the Latency Test, the Low-power Shapetest and the Full-power test. This means that Requirement G-MR4, G-MR11, and G-MR12 could not be confirmed.

Due to the system not being tested as extensively as intended, and considering it is unprofessional and unethical to test a non-functional device on a living animal, the decision was made not to perform this test. Consequently, requirement G-TR1 is not met.

8.2 Discussion

When it was time to test the complete design, it quickly became apparent that this would not be possible due to time constraints. However, since the device has been simulated and all the necessary software and hardware are already in place, assembling and confirming the design should be relatively straightforward. This task can be undertaken in future research. Simulations confirmed that all the general requirements are theoretically met, validating that the design process was conducted in a professional and coherent manner.

Chapter 9

Conclusion

This thesis addresses the question: **"How should a product be designed to effectively and safely utilise inductors for noninvasive neuronal stimulation at various sites on an earthworm, while ensuring accurate monitoring of the response of the neuron?"** The design approach is based on meeting specific requirements, which led to dividing the device into three subsystems: Stimulation, Control, and Recording. Each subsystem has its own set of requirements, with results and conclusions detailed in their respective chapters.

In these subsystems, most of the requirements outlined in the Programme of Requirements appear to be met. However, since not all requirements have been tested and confirmed, it cannot be definitively stated that all requirements are satisfied. Table 9.1 displays the mandatory requirements and their status in the physical realisation.

Requirement:	Achieved:	Value:
G-MR1	No	
G-MR2	No	
G-MR3	Yes	
G-MR4	No	
G-MR5	No	
G-MR6	No	
G-MR7	Yes	
G-MR8	No	
G-MR9	Yes	
G-MR10	Yes	
G-MR11	No	
G-MR12	No	
G-MR13	No	
G-MR14	Yes	€530,-

Table 9.1: Mandatory Requirements with indication which requirements are met in the physical realisation. It can be seen that most of the requirements are not met due to lack of testing.

References

[1] A. T. Barker, "An Introduction to the Basic Principles of Magnetic Nerve Stimulation," *Journal of Clinical Neurophysiology*, vol. 8, no. 1, pp. 26–37, 1 1991.

[2] M. Hallett, "Transcranial Magnetic Stimulation: A Primer," *Neuron*, vol. 55, no. 2, pp. 187–199, 7 2007.

[3] A. Barker, R. Jalinous, and I. Freeston, "NON-INVASIVE MAGNETIC STIMULATION OF HUMAN MOTOR CORTEX," *The Lancet*, vol. 325, no. 8437, pp. 1106–1107, 5 1985.

[4] H. R. Siebner, K. Funke, A. S. Aberra, A. Antal, S. Bestmann, R. Chen, J. Classen, M. Davare, V. Di Lazzaro, P. T. Fox, M. Hallett, A. N. Karabanov, J. Kesselheim, M. M. Beck, G. Koch, D. Liebetanz, S. Meunier, C. Miniussi, W. Paulus, A. V. Peterchev, T. Popa, M. C. Ridding, A. Thielscher, U. Ziemann, J. C. Rothwell, and Y. Ugawa, "Transcranial magnetic stimulation of the brain: What is stimulated? – A consensus and critical position paper," *Clinical Neurophysiology*, vol. 140, pp. 59–97, 8 2022.

[5] W. Jiang, R. Isenhart, C. Y. Liu, and D. Song, "A C-shaped miniaturized coil for transcranial magnetic stimulation in rodents," *Journal of Neural Engineering*, vol. 20, no. 2, p. 026022, 4 2023.

[6] J. Ruohonen, P. Ravazzani, F. Grandori, and R. J. Ilmoniemi, "Theory of Multichannel Magnetic Stimulation: Toward Functional Neuromuscular Rehabilitation," Tech. Rep. 6, 1999.

[7] X. Wang, Y. Chen, M. Guo, and M. Wang, "Design of multi-channel brain magnetic stimulator and ansys simulation," *IJBEM*, vol. 7, no. 1, pp. 259–262, 2005.

[8] S. Yang, G. Xu, L. Wang, Y. Geng, H. Yu, and Q. Yang, "Circular coil array model for transcranial magnetic stimulation," in *IEEE Transactions on Applied Superconductivity*, vol. 20, no. 3, 6 2010, pp. 829–833.

[9] Z.-D. Deng, S. H. Lisanby, and A. V. Peterchev, "Electric field depth–focality tradeoff in transcranial magnetic stimulation: Simulation comparison of 50 coil designs," *Brain Stimulation*, vol. 6, no. 1, pp. 1–13, 1 2013.

[10] J. Rodger, C. Mo, T. Wilks, S. A. Dunlop, and R. M. Sherrard, "Transcranial pulsed magnetic field stimulation facilitates reorganization of abnormal neural circuits and corrects behavioral deficits without disrupting normal connectivity," *The FASEB Journal*, vol. 26, no. 4, pp. 1593–1606, 4 2012.

[11] K. Makowiecki, A. R. Harvey, R. M. Sherrard, and J. Rodger, "Low-Intensity Repetitive Transcranial Magnetic Stimulation Improves Abnormal Visual Cortical Circuit Topography and Upregulates BDNF in Mice," *Journal of Neuroscience*, vol. 34, no. 32, pp. 10 780–10 792, 8 2014.

[12] A. D. Tang, A. S. Lowe, A. R. Garrett, R. Woodward, W. Bennett, A. J. Canty, M. I. Garry, M. R. Hinder, J. J. Summers, R. Gersner, A. Rotenberg, G. Thickbroom, J. Walton, and J. Rodger, "Construction and Evaluation of Rodent-Specific rTMS Coils," *Frontiers in Neural Circuits*, vol. 10, 6 2016.

[13] M. T. Wilson, A. D. Tang, K. Iyer, H. McKee, J. Waas, and J. Rodger, "The challenges of producing effective small coils for transcranial magnetic stimulation of mice," *Biomedical Physics & Engineering Express*, vol. 4, no. 3, p. 037002, 4 2018.

[14] F. A. Khokhar, L. J. Voss, D. A. Steyn-Ross, and M. T. Wilson, "Design and Demonstration ¡i¿In Vitro¡/i¿ of a Mouse-Specific Transcranial Magnetic Stimulation Coil," *IEEE Transactions on Magnetics*, vol. 57, no. 7, pp. 1–11, 7 2021.

[15] J. Parthoens, J. Verhaeghe, T. Wyckhuys, S. Stroobants, and S. Staelens, "Small-animal repetitive transcranial magnetic stimulation combined with [18F]-FDG microPET to quantify the neuromodulation effect in the rat brain," *Neuroscience*, vol. 275, pp. 436–443, 9 2014.

[16] J. Boonzaier, P. I. Petrov, W. M. Otte, N. Smirnov, S. F. Neggers, and R. M. Dijkhuizen, "Design and Evaluation of a Rodent-Specific Transcranial Magnetic Stimulation Coil: An In Silico and In Vivo Validation Study," *Neuromodulation: Technology at the Neural Interface*, vol. 23, no. 3, pp. 324–334, 4 2020.

[17] J. O. Nieminen, A. S. Pospelov, L. M. Koponen, P. Yrjölä, A. Shulga, S. Khirug, and C. Rivera, "Transcranial magnetic stimulation set-up for small animals," *Frontiers in Neuroscience*, vol. 16, 11 2022.

[18] D. Cohen and B. N. Cuffin, "Developing a More Focal Magnetic Stimulator. Part I," *Journal of Clinical Neurophysiology*, vol. 8, no. 1, pp. 102–111, 1 1991.

[19] X. Liu, A. J. Whalen, S. B. Ryu, S. W. Lee, S. I. Fried, K. Kim, C. Cai, M. Lauritzen, N. Bertram, B. Chang, T. Yu, and A. Han, "MEMS micro-coils for magnetic neurostimulation," *Biosensors and Bioelectronics*, vol. 227, p. 115143, 5 2023.

[20] M. Talebinejad, S. Musallam, and A. E. Marble, "A transcranial magnetic stimulation coil using rectangular braided Litz wire," in *2011 IEEE International Symposium on Medical Measurements and Applications*. IEEE, 5 2011, pp. 280–283.

[21] F. W. Grover, "Tables for the calculation of the inductance of circular coils of rectangular cross-section," *Journal of the Franklin Institute*, vol. 195, no. 2, pp. 246–248, 2 1923.

[22] C. Sonntag, E. Lomonova, and J. Duarte, *2008 International Conference on Electrical Machines : ICEM '08.* IEEE, 2008.

[23] B. He, *Neural Engineering*, B. He, Ed. Cham: Springer International Publishing, 1 2020. [Online]. Available: http://link.springer.com/10.1007/978-3-030-43395-6

[24] N. Arai, S. Okabe, T. Furubayashi, Y. Terao, K. Yuasa, and Y. Ugawa, "Comparison between short train, monophasic and biphasic repetitive transcranial magnetic stimulation (rTMS) of the human motor cortex," *Clinical Neurophysiology*, vol. 116, no. 3, pp. 605–613, 3 2005.

[25] A. V. Peterchev, R. Jalinous, and S. H. Lisanby, "A Transcranial Magnetic Stimulator Inducing Near-Rectangular Pulses With Controllable Pulse Width (cTMS)," *IEEE Transactions on Biomedical Engineering*, vol. 55, no. 1, pp. 257–266, 1 2008.

[26] "ESP32 Series Datasheet 2.4 GHz Wi-Fi + Bluetooth ® + Bluetooth LE SoC Including," Tech. Rep., 2024. [Online]. Available: www.espressif.com

[27] E. B. Rosa and L. Cohen, "Formulae and tables for the calculation of mutual and self-inductance," *Bulletin of the Bureau of Standards*, vol. 5, no. 1, p. 1, 8 1908.

[28] K. M. Shannon, G. J. Gage, A. Jankovic, W. J. Wilson, and T. C. Marzullo, "Portable conduction velocity experiments using earthworms for the college and high school neuroscience teaching laboratory," *Advances in Physiology Education*, vol. 38, no. 1, pp. 62–70, 3 2014. [Online]. Available: https://www.physiology.org/doi/10.1152/advan.00088.2013

[29] N. Kladt, U. Hanslik, and H.-G. Heinzel, "ARTICLE Teaching Basic Neurophysiology Using Intact Earthworms," Tech. Rep. [Online]. Available: www.funjournal.org

[30] M. S. Keshner, "1 / f Noise," Tech. Rep. 3, 1982.

[31] J. Wang, L. Tang, and J. E. Bronlund, "Surface EMG Signal Amplification and Filtering," Tech. Rep., 2013.

[32] G. Czanner, S. V. Sarma, D. Ba, U. T. Eden, W. Wu, E. Eskandar, H. H. Lim, S. Temereanca, W. A. Suzuki, and E. N. Brown, "Measuring the signal-to-noise ratio of a neuron," *Proceedings of the National Academy of Sciences of the United States of America*, vol. 112, no. 23, pp. 7141–7146, 6 2015.

[33] J. B. Johnson, "Thermal agitation of electricity in conductors," Tech. Rep., 1928.

[34] "MODEL SR560 LOW-NOISE PREAMPLIFIER," Tech. Rep., 1989.

[35] J. G. Proakis and D. G. Manolakis, *Digital signal processing.*

[36] D. I. Rubin, "Needle electromyography: Basic concepts," in *Handbook of Clinical Neurology.* Elsevier B.V., 1 2019, vol. 160, pp. 243–256.

[37] S. Gruss, M. Schmid, S. Walter, B. Schick, L. Holler, and E. Barth, "The impact of analgesic on EMG and other biosignals in a postoperative setting," *Frontiers in Medicine*, vol. 10, 3 2023.

[38] "https://www.researchgate.net/figure/Schematic-of-blanking-circuit-to-prevent-the-amplifier-from-saturation-in-the-presence-of_fig1_345724943."

[39] W. N. Hess, "Nervous system of the earthworm, lumbricus terrestris L." *Journal of Morphology*, vol. 40, no. 2, pp. 235–259, 6 1925.

[40] R. E. Coggeshall, "A fine structural analysis of the ventral nerve cord and associated sheath of ¡i¿Lumbricus terrestris¡/i¿ L." *Journal of Comparative Neurology*, vol. 125, no. 3, pp. 393–437, 12 1965.

[41] T. H. Bullock, "FUNCTIONAL ORGANIZATION OF THE GIANT FIBER SYSTEM OF ¡i¿LUMBRICUS¡/i¿," *Journal of Neurophysiology*, vol. 8, no. 1, pp. 55–71, 1 1945.

[42] C. A. Edwards and N. Q. Arancon, "Earthworm Morphology," in *Biology and Ecology of Earthworms.* New York, NY: Springer US, 2022, pp. 1–31.

[43] P. Basser, R. Wijesinghe, and B. Roth, "The activating function for magnetic stimulation derived from a three-dimensional volume conductor model," *IEEE Transactions on Biomedical Engineering*, vol. 39, no. 11, pp. 1207–1210, 1992.

[44] D. Tranchina and C. Nicholson, "A model for the polarization of neurons by extrinsically applied electric fields," *Biophysical Journal*, vol. 50, no. 6, pp. 1139–1156, 12 1986.

[45] T. Pashut, S. Wolfus, A. Friedman, M. Lavidor, I. Bar-Gad, Y. Yeshurun, and A. Korngreen, "Mechanisms of Magnetic Stimulation of Central Nervous System Neurons," *PLoS Computational Biology*, vol. 7, no. 3, p. e1002022, 3 2011.

[46] H. Seo, N. Schaworonkow, S. C. Jun, and J. Triesch, "A multi-scale computational model of the effects of TMS on motor cortex," *F1000Research*, vol. 5, p. 1945, 8 2016.

[47] T. Wu, J. Fan, K. S. Lee, and X. Li, "Cortical neuron activation induced by electromagnetic stimulation: a quantitative analysis via modelling and simulation," *Journal of Computational Neuroscience*, vol. 40, no. 1, pp. 51–64, 2 2016.

[48] A. S. Aberra, A. V. Peterchev, and W. M. Grill, "Biophysically realistic neuron models for simulation of cortical stimulation," *Journal of Neural Engineering*, vol. 15, no. 6, p. 066023, 12 2018.

Appendix A

Neurobiology

A.1 Nervous System of the Earthworm

The Lumbricus Terrestris (earthworm) consists of a large amount of segments. The nervous system is consistent in the middle segments and differs only in the anterior (front) and posterior (back) of the worm. As can be seen in Figure A.1, the worm has a central nerve cord that exists throughout the whole body length, with small branches in each segment [39]. In Figure A.2, a cross-section of the central nerve cord is given, which has a relatively uniform diameter [40]. It consists of three giant axons, one Medium Giant Fiber (MGF) (diameter $0.07mm$) and two smaller Lateral Giant Fibers (LGF) (diameter $0.05mm$).
In every segment several cell bodies send axons into the neurocords and the neurocords or their cell bodies send small processes into the neuropile, presumably to make connection with sensory or motor neurons. The fibers are interrupted in every segment by oblique septa. These divide the neurocord into segmental units and provide a broad area of contact between adjacent units, representing essentially synapses of unusual proportions. The giant fibers are thus chains of short compound axons. The two lateral fibers are connected by frequent anastomoses [41].
Sensory stimuli in one segment may invoke a motor response, either via fibers in the nerve of the same side of the same segment, the contra-lateral nerve of that segment, the nerve before or after that stimulated in the same segment, or even the segment in front or behind. Nerve connections extend for as many as three segments backward or forward along the body via association neurons. Stimuli from one segment can also reach other segments indirectly, because the sensory fields of the nerves supplying the body wall cover more than one segment.
Strong stimuli can bypass the association neurons and be transmitted up and down the giant fibers. The arrangement of giant fibers is important in allowing the transmission of motor impulses along the nerve cord at high speed (600 meters per second) and a very rapid reaction of the animal to adverse stimuli. There is some evidence that the MGF transmits stimuli only from the front to the back of the earthworm and not vice versa. It is believed that the LGF's transmit stimuli in the opposite direction. The most probable explanation is that the sensory input from the front of the animal passes into the median giant fiber and in the rear of the animal into the lateral fibers. Most of the available evidence indicates that the main chemical transmitter substances in the central nervous system are acetylcholine, probably adrenalin, noradrenalin, and possibly 5-hydroxytryptamine (5HT).
The main function of the enlarged cerebral ganglia in the front of the body seems to be mostly inhibitory, because if they are excised, the earthworm moves continuously. They seem to play little part in initiating movement [42]. Other research suggests that the MGF has a lower treshold than the LGF due to its larger diameter [29]. Measured conduction velocities differ in different articles. In anaesthetised worms, MGF speed was measured at 32.2 m/s and LGF speed at 12.6 m/s using tactile stimulation. In anaesthetised worms, the average speed of the LGF was 7.6 ± 1.2 m/s (mean $\pm$ SD) and the MGF was 22.8 ± 4.5 m/s (mean $\pm$ SD) [28].

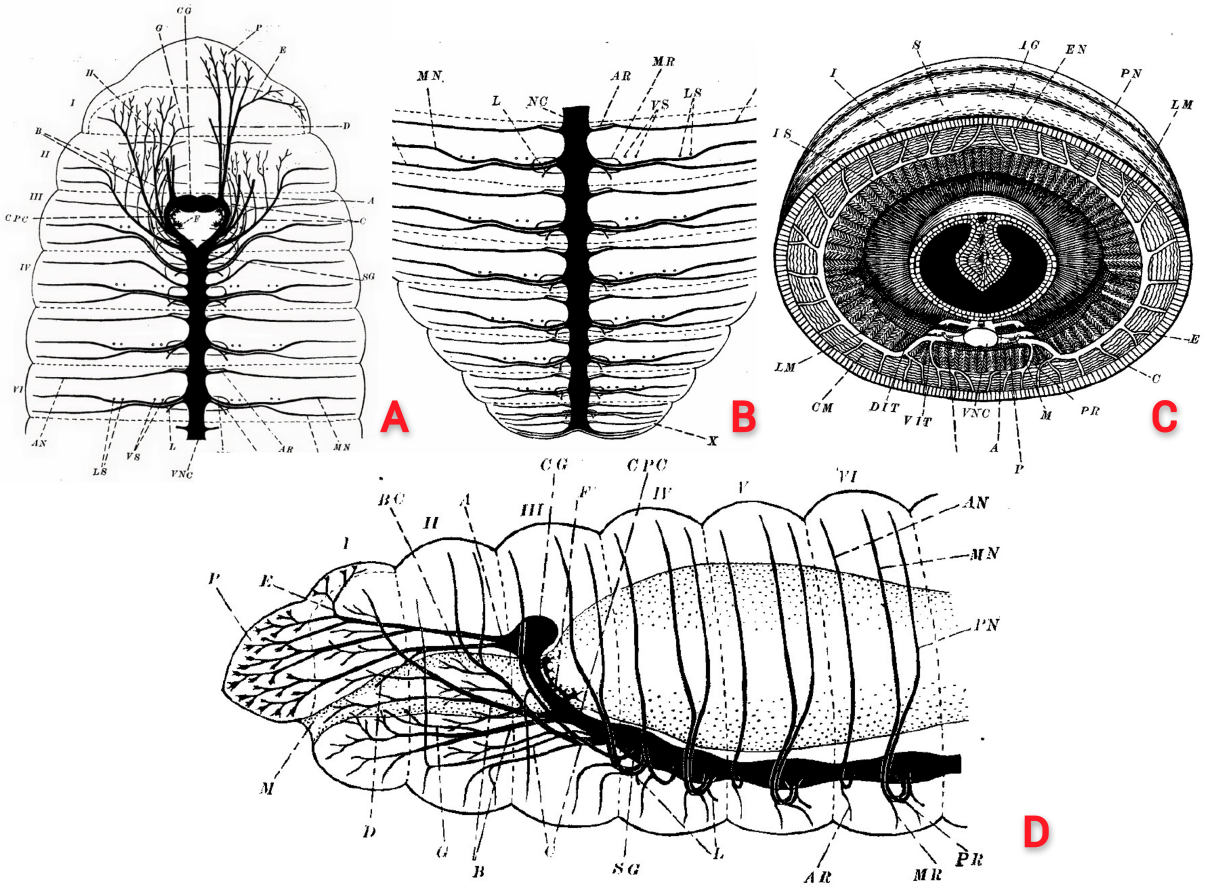

Figure A.1: Anatomy of the nervous system of L. Terrestris (earthworm). Drawing showing the arrangement of the larger nerves in the anterior (A) and posterior (B) segments, as viewed in a dissection from the dorsal side. (C) Drawing of cross-section, dorsoposterior view, showing the arrangement of the nerves in a single segment. (D) Drawing showing a lateral view of the arrangement of the larger nerve trunks in the left half of the anterior segments [39].

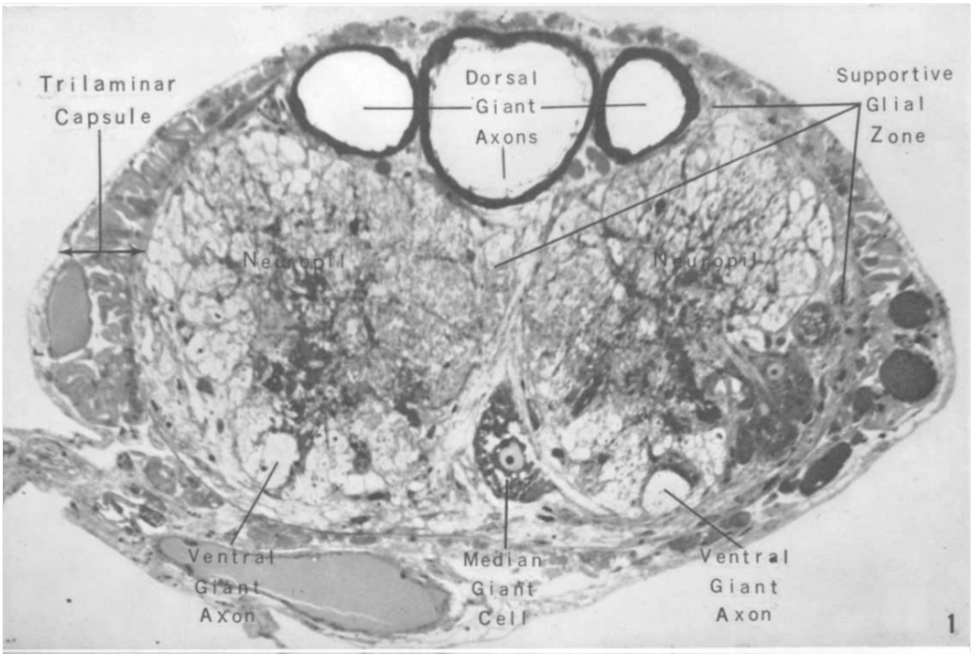

Figure A.2: A light micrograph of a cross section through the posterior part of the ventral nerve cord of the earthworm [40].

A.2 Action Potential Induced by E-field

Strength-Duration Curve

Neurons have a threshold function for evoking a by an E-field induced action potential that is called the Strength-Duration (S-D) curve [4]. It is closely related to neurophysiological concepts of chronaxie and rheobase. Rheobase describes the minimum current amplitude (of infinite duration) that leads to threshold depolarisation, whereas chronaxie is the minimum time required for a current at double the strength of the rheobase to initiate an action potential [4]. The shape of this curve is shown in Figure A.3. The time constants for peripheral nerves and motor cortex pulse are similar and are around 150 µs to 300 µs. Most TMS devices use therefore a pulse duration of around 30 µs to 150 µs, with an E-field strength of around 30 V/m to 100 V/m.

Stimulation site

Tranchina and Nicholson (1986) used analytical analysis of basic cable theory and concluded that Axons can be stimulated by electric field gradients along their length. These gradients can occur due to spatial changes in the induced electric field or due to changes in the axon geometry. The spatial changes in the field is often referred to as the activator function which includes $-\frac{\delta E_x}{\delta x}$ [43]. Tranchina and Nicholson predicted peak polarisation at the soma by uniform E-field due to impedance mismatch between the axon and dendrite [44]. In agreement with this, some modelling work using compartmental neuron models also found that the soma is being depolarised enough to trigger an action potential at the axon's initial segment at threshold intensities [45][46]. However, these studies used simplified model neurons with a single, straight main axon without including axonal arborization or axon terminals. [4]. At variance with the notion of soma sensitivity, biophysical models that included realistic axon morphologies [47][48], found that axon discontinuities have substantially lower thresholds for activation by TMS [4]. These results seem more plausible since Tranchina and Nicholson also came to the conclusion that in a bent axon, polarization focuses at the bend, potentially reaching the action potential threshold there first instead of at the soma [44].

In summary, it is highly unlikely that TMS selectively excites exclusively a specific neuronal microstructure. However the prevailing view is that TMS activates primarily myelinated axons at their bends, bifurcations or terminations [4]. In addition to this uncertainty, the sedation of the worm might also influence its neuronal mechanisms. Depending on the kind of substance used, anesthesia may dampen neuronal excitability in general or affect primarily excitatory or inhibitory synaptic transmission, thereby possibly interfering with the TMS effects [4].

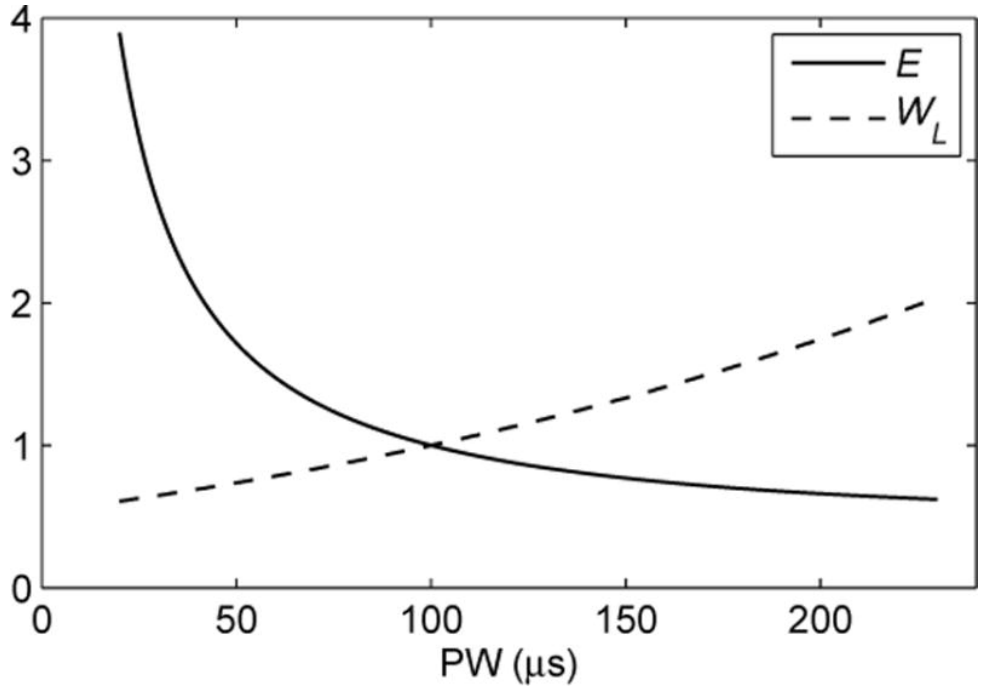

Figure A.3: Strength-duration curves linking rectangular pulse width (PW) to electric field strength E and coil energy WL for threshold stimulation of neuron with membrane time constant of $\tau_m = 150\,\mu s$. Curves are normalized to one at PW $= 100\,\mu s$ [25].

Appendix B

Code

All the code that is used can be found on the GitHub link below:
`https://github.com/DoornSKA/BEP_code`